DOTTORATO DI RICERCA IN
PHYSICS AND NANO SCIENCES

XXVI CICLO

Sede Amministrativa

Università degli Studi di MODENA e REGGIO EMILIA

TESI PER IL CONSEGUIMENTO DEL TITOLO DI
DOTTORE DI RICERCA

Electronic properties of dye/ZnO interfaces for photovoltaic applications

Candidato: Gaëlle Françoise Arnaud

Relatore: Valentina de Renzi

---

3 Febbraio 2014

Contents

1 Introduction **1**

1.1 Background 1

1.2 Aims of the project 2

2 Dye Sensitized Solar Cells **7**

2.1 Operation principle of a DSSC 10

2.2 Energetics 14

2.2.1 Tuning of the energy level alignment 19

2.3 Materials 20

2.3.1 Photosensitizing Dye 20

2.3.1.1 Anchoring Group 23

2.3.2 Semiconducting Oxide 25

3 Dye/metal-oxide model systems **33**

3.1 TiO_2 structural and electronic properties 33

3.2 Zinc Oxide structural and electronic properties 35

3.3 Catechol/metal-oxide interfaces 37

3.3.1 An introduction to catechol 37

3.3.2 How catechol adsorbs on TiO_2 39

3.3.3 Electronic properties of catechol/TiO_2 interfaces 42

3.3.4 How catechol adsorbs on ZnO surfaces 43

3.3.5 Electronic properties of catechol/ZnO interfaces 44

3.4 Phthalocyanine/metal-oxide interfaces 47
3.4.1 Metal-Phthalocyanines on TiO_2 surfaces 47
3.4.2 Metal-Phthalocyanines on ZnO surfaces 49
3.4.2.1 Electronic properties: work function change and molecular level alignment 51

4 Experimental techniques 57

4.1 Photoelectron spectroscopy (PES) 57
4.1.1 X-ray Photoelectron spectroscopy (XPS) 59
4.1.1.1 Quantitative analysis for XPS 61
4.1.2 UV photoelectron spectroscopy (UPS) 65
4.1.2.1 Determination of work function 66
4.2 Low-energy electron diffraction (LEED) 67
4.3 High resolution electron energy loss spectroscopy (HREELS) 69
4.4 Experimental procedures 71
4.4.1 Dye deposition 72

5 Results and discussion 77

5.1 Characterization of the ZnO($10\bar{1}0$) surface 78
5.2 The catechol/ZnO interface 81
5.2.1 Catechol adsorption 81
5.2.2 Electronic properties 82
5.3 The 4-Nitrocatechol/ZnO interface 85
5.3.1 4-Nitrocatechol adsorption 86
5.3.2 UPS and HREELS - Electronic properties 88
5.3.2.1 Band bending 92
5.3.2.2 Work function and ionization potential 93
5.4 Co-evaporation of 4-nitrocatechol and ethanol 97
5.4.1 Ethanol/ZnO interface characterization 97
5.4.2 Ethanol/4-nitrocatechol/ZnO interface characterization 99

5.5 From 4-nitrocatechol to aminocatechol 103

5.5.1 Ionization energy variation 105

5.6 Cu-Phthalocyanine on ZnO($10\bar{1}0$) 107

5.6.1 Cu-Phthalocyanine adsorption 107

5.6.2 CuPc/ZnO interface - electronic properties 109

6 Conclusions **115**

List of Figures

2.0.1 Schematic illustration of a typical dye sensitized solar cell (DSSC) 7

2.0.2 I-V curve of a solar cell in dark and under illumination. 9

2.1.1 Energy level and device operation of DSCs 10

2.2.1 Energy diagram of a semiconductor 17

2.3.1 Ruthenium N-719 dye. 21

2.3.2 Zn-TP-$(COOH)_2$ and TT1 structures 22

2.3.3 Binding modes for carboxylate unit on TiO_2 surface. 24

2.3.4 A top-view SEM image of rutile - TiO_2 electrodes. 25

3.1.1 Structure of rutile (110) and anatase (101) 34

3.2.1 ZnO structure 36

3.2.2 Structure of a bulk-truncated mixed-surface ZnO$(10\bar{1}0)$ 36

3.3.1 Types - II of electron injection pathways from an desorbed dye to TiO_2 in DSSC 37

3.3.2 Structure of the catechol molecule 37

3.3.3 Spectra of free and bound catechol 38

3.3.4 Calculated rotational pathway of a catechol on $TiO_2(110)$ with the lowest E_{act} 40

3.3.5 Full monolayer of catechol on anatase $TiO_2(101)$ 41

3.3.6 Adsorption configurations of isolated catechol molecules on anatase $TiO_2(101)$ 42

3.3.7 UPS spectra of clean and functionalized anatase $TiO_2(101)$ 43

3.3.8 Total DOS and projected contributions on ZnO substrate and catechol for the molecule/surface interface 44
3.3.9 HOMO and LUMO energy alignment for different molecules with respect to the vacuum level in the gas phase 46
3.4.1 Structure of Cu-phthalocyanine molecule 48
3.4.2 XPS Core level spectra of C1s and N1s of ZnPc on TiO_2 48
3.4.3 VB spectra: HOMO region at different coverages of ZnPc on TiO_2[15]. . . . 49
3.4.4 VB spectra of FePc/TiO_2 50
3.4.5 Valance band region of UPS spectra for CuPc deposited on ZnO film[19]. . 51
3.4.6 Map of He I UPS spectral intensities for VL and HOMO band regions of the CuPc-HOPG and OTiPc/HOPG systems as a function of deposition amount 53

4.1.1 Photoelectron spectroscopy scheme 57
4.1.2 Representation of an XPS apparatus 59
4.1.3 Drawing of background subtraction 62
4.1.4 Main steps for a quantitative analysis of an XPS core level peak 64
4.1.5 Schematic energy diagram of a n-type semiconductor. 67
4.2.1 Scheme of a LEED apparatus and a typical diffraction pattern 68
4.3.1 Schematic drawing of an HREELS experiment 69
4.3.2 Photograph of a modern ultrahigh-resolution EEL spectrometer. 70

5.1.1 LEED pattern and STM image of ZnO($10\bar{1}0$) clean surface 78
5.1.2 XPS core levels of the ZnO($10\bar{1}0$) clean surface 79
5.1.3 The vibrational region of the HREELS spectrum for the ZnO clean surface 80
5.2.1 O1s and C1s core level peaks for the catechol/ZnO system for the saturation coverage 82
5.2.2 UP spectra of clean ZnO($10\bar{1}0$) surface and the saturation coverage. 84
5.3.1 Theoretical adsorption model of 4-nitorcatechol on ZnO($10\bar{1}0$) surface . . . 86

5.3.2 O 1s, N 1s and C 1s XPS core level peak for clean and functionalized ZnO surface 86

5.3.3 C1s core level peak of saturation coverage 4-nitrocatechol/ZnO($10\bar{1}0$) surface 87

5.3.4 UPS valence band spectra of the clean ZnO($10\bar{1}0$) surface and 4-nitrocatechol/ZnO system. 89

5.3.5 Total density of states and its projected contribution on 4-nitrocatechol for the molecule/ZnO interface system. 90

5.3.6 UPS VB spectrum and HREELS spectrum of the clean and 4-nitrocatechol/ZnO($10\bar{1}0$) surface 91

5.3.7 VB spectra and band bending variation of the clean surface and 4-nitrocatechol/ZnO system 92

5.3.8 XPS spectra in the secondary electron cutoff region as a function of 4-nitrocatechol coverage. 94

5.3.9 Variation of work function, band bending and ionization potential energy as a function of 4-nitrocatechol coverage. 95

5.3.10 Macroscopic average of the electrostatic potential for the clean surface and 4-nitrocatechol/ZnO surface 96

5.4.1 O1s and C 1s XPS core level spectra of EtOH/ZnO 98

5.4.2 UPS VB spectra of the clean ZnO surface and the functionalized surface. . 100

5.4.3 Left panel: O1s core level of the clean surface and the EtOH/4-nitrocatechol/ZnO system. Right panel: C1s core level spectra of the EtOH/ZnO and EtOH/4-nitrocatechol/ZnO 101

5.4.4 UPS VB spectra of clean ZnO, EtOH/ZnO, 4-nitrocatechol/ZnO and EtOH/4-nitrocatechol/ZnO 102

5.5.1 XPS N1s core levels spectra as function of irradiation time. 104

5.5.2 C1s and O1s XPS core levels spectra of 4-nitrocatechol/ZnO before and after two hour of irradiation 105

5.5.3 Variation of the WF measured as a function of time irradiation 106

5.6.1 Intensity ratio between the N1s and Zn2p core level peak intensity as a function of evaporation time. 107
5.6.2 C1s and N1s XPS core level peaks of Cu/ZnO system 109
5.6.3 N1s, C1s and $Cu2p_{2/3}$XPS core level peaks of CuPc/ZnO system 109
5.6.4 N1s, C1s and $Cu2p_{2/3}$core-level energies as function of coverage 110
5.6.5 HREEL spectra: electron transition region for different coverage. 111
5.6.6 UPS VB spectra of clean surface and different CuPc/ZnO coverage 112

Nomenclature

ΔI	Ionization Eenrgy
η	solar-to-electric power conversion efficiency
AES	Auger Electron Spectroscopy
AM1.5	1.5 atmosphere thickness (i.e. solar zenith angle of z=48.2°)
aminocatechol	4-amino-1,2-benzendiol
ASF	Atomic Sensitivity Factor
CB	Conduction band
CuPc	Cu-phthalocyanine
DOS	Density Of States
DSSC	dye sensitized solar cell
EF	Fermi Energy
EtOH	Ethanol
HOMO	Highest occupied molecular orbital
HREELS	High Resolution Electron Energy Loss
LEED	Low Energy Electron Diffraction
LUMO	lowest unoccupied molecular orbital

NIR	Near-infrared
UPS	UV Photoelectron Spectroscopy
VB	Valence Band
Vbb	Band Bending
VL	Vacuum Level
Voc	open-circuit voltage
WF	Work function
XPS	X-Ray Photoelectron Spectroscopy

Chapter 1

Introduction

1.1 Background

The interfaces between organic molecules and inorganic substrates are extremely relevant in both scientific and technological fields as they play a key role in the development of electronic devices based on organic materials: organic light emitting diodes, transistors, sensors, and dye sensitized solar cells.

Nowadays, one of the most relevant topics of this field regards the development of novel organic solar cells, such as dye-sensitized solar cells (DSSCs), organic photovoltaic, multi-junction photovoltaic cells (tandem cells) and quantum dot sensitized solar cells. The major advantage offered by organic materials, as dyes, is their inherently low production costs. Furthermore, dyes can exhibit very high absorption coefficients, allowing efficient harvesting of sunlight from very thin films. Moreover, their properties, such as optical band-gap, molecular orbital energy levels and the nature of any functional group present, can be quite easily chemically tailored in order to meet the requirements needed to optimize device performances.

Accordingly, the research is currently interested in identifying and optimizing the properties of novel materials to be use in photovoltaic cells. Since Graetzel and co-workers first announced 7.1-7.8 % efficiency for dye sensitized solar cells (DSSCs) obtained using dye

sensitized colloidal titanium oxide (TiO_2) films in 1991[1], DSSCs has received continuous and intense attention. Part of the research effort is focused in the development and understanding of the principles which govern the operation of this type of organic photovoltaic cells. The major advantage offered by organic materials, as dyes, is their inherently low production costs. Furthermore, dyes can exhibit very high absorption coefficients, allowing efficient harvesting of sunlight from very thin films. Moreover, their properties, such as optical band-gap, molecular orbital energy levels and the nature of any functional group present, can be quite easily chemically tailored in order to meet the requirements needed to optimize device performances.

A key to design high performance optical and electronic organic devices is the understanding of the electronic properties of the molecule/inorganic heterojunction[4, 5]. Indeed, in the case of DSSC, the knowledge of the electronic properties of the interfaces between the electrodes and the active organic layers is of enormous importance for the device efficiency. In fact, the mechanisms of electron transfer between the molecular adsorbate and the semiconductor materials has been subject of intense research in recent years[2, 3]. On the other hand, the microscopic mechanisms determining the energy alignment at the interface has been less investigated. Indeed, while this issue has been extensively studied in the case of organic/metal and organic/semiconductor (mainly silicon and III-V compounds) interfaces[5, 7, 4], the case of wide-gap metal oxide surfaces is quite unexplored.

1.2 Aims of the project

The main part of this work deals with the experimental study, by means of several complementary electron spectroscopies, of the interfacial electronic properties of two dyes, catechol and 4-nitrocatechol, on ZnO($10\bar{1}0$) single crystal surface as model systems. ZnO is a wide-gap semiconductor characterized by high electron mobility and ease of growth in different nanostructures. For this reason, it is one of the most promising alternative to TiO_2 in the DSSC field. Catechol is used in DSSC system as a linker which may bond

more complex dyes to the metal-oxide surface. It also behaves as the simplest sensitizer, as its adsorption induces a red-shift in the absorption spectrum of metal-oxide nanoparticles. Moreover, 4-nitrocatechol posses a significant permanent dipole moment and has been therefore chosen to investigate the role of molecular dipole moment on energy level alignment at the interface.

Indeed, we found that 4-nitrocatechol adsorption modifies the interface ionization potential by more than one eV, allowing us to analyze in details how this variation influences the electronic properties at the interface.

The differences between dye/semiconductor model systems and real DSSC interfaces are quite significant, and are mainly due to the latter complexity. A real DSSC interface is indeed an extended interface, formed by a number of different mutually interacting components. Despite the simplicity of model systems, the understanding of the relevant mechanisms governing DSSC performances which can be derived by UHV-based spectroscopic investigations is undoubted. Bridging the gap between model and real systems is therefore an extremely important and challenging issue. In a tentative to make a step in this direction, we investigated the co-evaporation of 4-nitrocatechol and ethanol, one of the typical solvents used in the production of DSSC pastes. This mixed system represents also a model for investigating the co-adsorption of molecules with opposite dipole moments.

In the last part of this work we addressed the study of Cu-phthalocyanine adsorption on ZnO($10\bar{1}0$) surface. Since phthalocyanines, together with porphyrins are characterized by variability of their molecular structures, optical spectra, electrical properties, and supramolecular organization[6], they play a central role in organic solar cells study. We investigated the adsorption and the electronic properties at the interface between the phthalocyanine dye and the ZnO surface as a function of the ad layer thickness, aiming at a better understanding of the interactions between the molecular dye and the surface, and focusing on the ways adsorption influences the interface electronic properties.

Bibliography

[1] B. O'Regan, M. Gratzel, Nature 1991, 353, 737.

[2] A. H. M. Gratzel, Chem. Rev. 1995, 95, 49.

[3] C. Bauer, G. Boschloo, E. Mukhtar, A. Hagfeldt, J. Phys. Chem. B 2002, 106, 12693.

[4] H. Ishii, K. Sugiyama, E. Ito, K. Seki, Adv. Mater. 1999, 11, 8.

[5] D. Cahen, A. Kahn, E. Umbach, Mater. Today 2005, 32.

[6] N. Papageorgiou, E. Salomon, T. Angot, J-M Layet, L. Giovanelli, G. Le Lay Prog. Surf. Sci. 2004, 77, 139.

[7] Z. Zhang, J. T. Yates, Chem. Rev. 2012, 112, 5520.

Chapter 2

Dye Sensitized Solar Cells

A dye sensitized solar cell (DSSC) is a photoelectrochemical cell in which light is absorbed by a molecular-sensitized photoanode, and electron-hole charge separation occurs at the interface between the photoanode itself and the electrolyte[1]. In this way, in DSSC the function of light absorption and that of charge carrier transport are separated in different materials. The main parts of a dye sensitized solar cell are illustrated schematically in Figure 2.0.1.

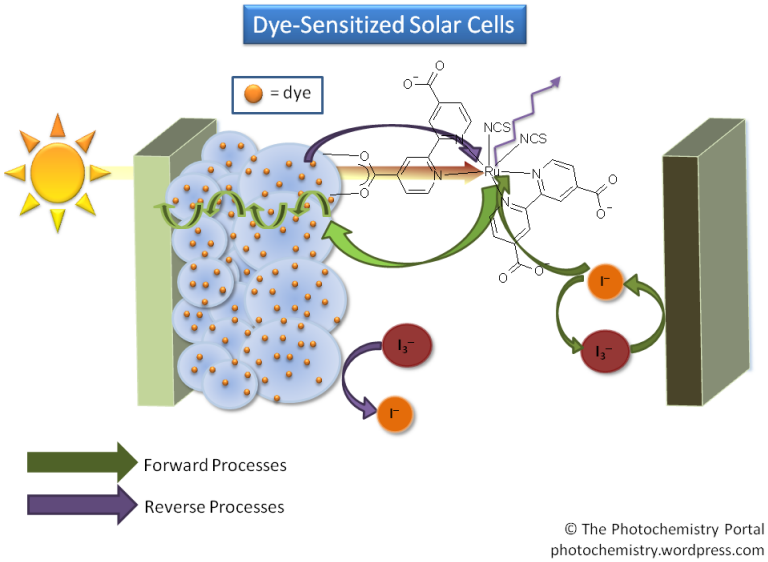

Figure 2.0.1: Schematic illustration of a typical dye sensitized solar cell (DSSC)

A typical DSSC consists of a nanostructured wide band-gap semiconducting layer deposited on a transparent conductive oxide (TCO, usually an ITO-covered glass) substrate, a dye molecule (sensitizer), an electrolyte, and a counterelectrode. The nanocrystalline semiconductor - like, for example, TiO_2, ZnO, SnO_2 and Nb_2O_5, is functionalized with the photosensitized dye. The dye, typically a metallorganic Ru- complex, is chemically anchored to the semiconductor, thus forming a monolayer thick film. The network of TiO_2 nanoparticles that composes the oxide layer is sintered together to establish electrical conduction. Its structure is mesoporous in order to produce a high surface area for dye coverage, therefore increasing the cell absorption efficiency. Indeed, the dimension of nanoparticles (20-30 nm) determines an increase in their effective surface area by a factor of more than a thousand relative to the projected area. This porous photoanode is immersed in an electrolyte which contains a redox mediator, typically the redox couple I^-/I_3^-. When solar light is absorbed by the molecular dye, it excites an electron from the dye HOMO (highest occupied molecular orbital) to the LUMO (lowest unoccupied molecular orbital). Charge separation is achieved through electron injection from the excited state of the dye into the conduction band (CB) of the metal oxide. From there electrons diffuse through the mesoporous photoanode, reaching the electrode. This process results in the formation of dye cations, which are subsequently reduced by the redox mediator. The oxidized ionic species diffuse through the electrolyte to the platinum-coated cathode, thus maintain electrical neutrality. Overall, electric power is therefore generated without permanent chemical transformation.

The solar-to-electric power conversion efficiency of DSSCs, η, depends on a delicate balance between the kinetics of injection, dye regeneration properties and recombination reactions. η is defined as the ratio between the maximum power obtainable by the device and the power flux of the incident light I_0. It is usually expressed as:

$$\eta = \frac{J_{sc} V_{oc} FF}{I_0} \tag{2.0.1}$$

where the short-circuit current (J_{sc}) and the open circuit voltage (V_{oc}) are the maximum current and voltage obtainable from the solar cell, respectively. The fill factor FF is

defined as the ratio between the maximum power obtained by the solar cell and the product of V_{oc} and J_{sc}. In Figure 2.0.2, the I-V curve of a typical DSS cell is reported. The open-circuit potential is defined by the point of the graph where the flux of recombining charges is equal to that of charge generation, i.e. where the total current is zero. On the other hand, the short circuit current density, J_{sc}, corresponds to the maximum value of the current, achieved at zero potential. Graphically, FF is a measure of the "squareness" of the IV curve and corresponds to the area of the largest rectangle which could fit in it. The product of the short circuit density (J_{sc}) and the open circuit photovoltage (V_{oc}) represents therefore the maximum power which would be achieved by the DSSC in the case of an ideal square-like behavior of the I-V curve. The real maximum power is instead obtainable at the operating point MPP (maximum power point) of the cell, as indicated in Figure 2.0.2.

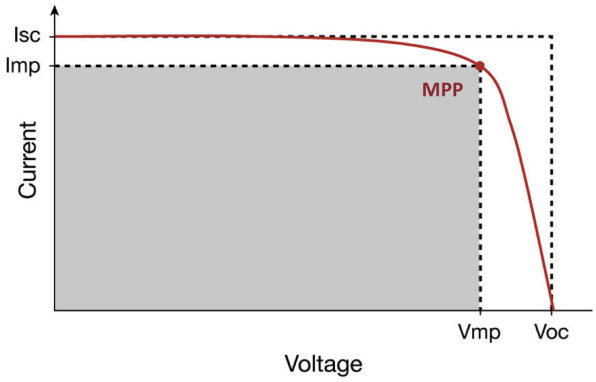

Figure 2.0.2: I-V curve of a solar cell in dark and under illumination.

At present, the best Ru-complex based devices exhibit a power conversion efficiencies approaching 11.8% under standard AM1.5 illumination conditions[2], while very recently a new record efficiency was established (13%), exploiting a novel porphyrine-based moiety as dye and the Co^{2+}/Co^{3+} as redox mediator[3].

2.1 Operation principle of a DSSC

Although DSSCs appear extremely simple in concept, their efficiency is determined by the complex interplay between several different processes and between different material components, whose global optimization is therefore an extremely challenging task.

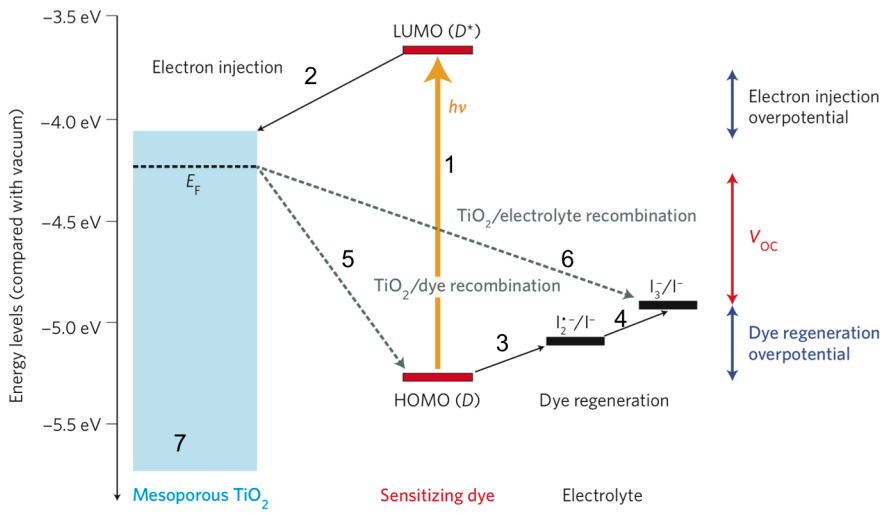

Figure 2.1.1: Energy level and device operation of DSCs; the sensitizing dye absorbs a photon (energy $h\nu$), the electron is injected into the CB of the metal oxide (TiO_2) and travels to the front electrode (not shown). The oxidized dye is reduced by the electrolyte, which is regenerated at the counter-electrode (not shown) to complete the circuit. V_{OC} is determined by the difference between the quasi-Fermi level (E_F) of TiO_2 and the redox potential (I_3^-/I^-) of the electrolyte.

In the following, we briefly describe the fundamental processes occurring during DSC functioning, mainly focusing on their kinetics. The energetics of the processes, which also play a fundamental role, will be discussed in more details in Section 2.2. The values of the relevant parameters here reported refers to a typical DSSC, i.e. one made by a nanostructured TiO_2 semiconductor functionalized by a Ru-complex dye, which exploits a iodide/triiodide redox couple as mediator.

- Light absorption from the photosensitizer (1) :

Upon photon absorption, the HOMO electron of the dye is promoted in an excited state.

The power efficiency of this step depends both on the matching between the solar emission spectrum and the absorption spectrum of the dye, and on the molar extinction coefficient of the dye in that wavelength range. The absorption spectrum of a typical Ru-based dye is reported in Figure 2.3.1: it is characterized by a fairly broad absorption range ($\Delta\lambda = 350$ nm), with an onset at around 720 nm, which corresponds to a photon energy of 1.72 eV. Typical values of the molar extinction coefficient in this wavelength range are 10000-20000 $M^{-1}cm^{-1}$.

- Electron injection from the dye to the metal-oxide (2) and back reactions (5)

The excited electron is injected from the dye into the conduction band of TiO_2. Although the detailed mechanism of the injection process is still under debate, it is generally accepted that a fast femtosecond component is observed when the sensitizer is directly attached to the oxide surface. This timescale should be compared with those of the decay of the dye excited state to the ground state (reaction 1) and of the back reactions, i.e. electron transfer back to the sensitizer molecules (reaction 5) or to the electrolyte acceptor (reaction 6). Generally, the injection process is much faster than the excited state decay, thus contributing to efficient charge separation in the device. Indeed, in the case of the long-lived triplet state of Ru-complexes, the lifetime of the excited state is in the tens of nanosecond range[4]. It is nevertheless interesting to note that electron injection in a complete DSC device has been found to occur with halftimes of around 150 ps, i.e. slow enough for kinetic competition between the injection and decay processes, with potential implications for the overall DSC performances[5].

As far as electron back-transfer from the semiconductor to the dye is concerned, it has been found to follow a multi-exponential time law, occurring in the μs - ms range. These timescales depend on the density of injected electrons in the semiconductor and thus in turn on light intensity. This process is therefore several orders of magnitude slower than electron injection. In the case of the I^-/I_2 redox couple, recombination of electrons with the electrolyte acceptors also happened on timescales in the ms range. These values are much longer than those of other redox systems, thus being therefore one of the main

reasons for the I^-/I_3^- success.

- Charge transport through the semiconductor film (7):

The nanoporous TiO_2 layer, which is typically 10 µm thick, contains spherical anatase particles with a diameter between 20 - 30 nm, sintered together by the annealing process. Its porosity is 50-60%. The oxide particles and the electrolyte-containing pores form an interpenetrating network, through which electrons can percolate by hopping from one crystallite to the next.

Since the TiO_2-particles are too small for a macroscopic electric field to build up, diffusion is the main transport mechanism for electrons in the TiO_2 layer. The driving force for charge transport across the oxide layer is therefore provided by the electron density gradient across the layer, which strongly depends on light intensity. In the simplest model, the governing equation used to describe electron transfer in semiconductor films can be expressed as:

$$D_{eff} = \frac{\partial^2 n(x)}{\partial x^2} - \frac{n(x) - n_0}{\tau} + \alpha I_0 e^{-\alpha x} \tag{2.1.1}$$

where D_{eff} is the diffusion constant of electrons in the film, $n(x)$ is the excess electron density, n_0 is the electron density in the dark, I_0 represents the incident light intensity, and α is the reciprocal absorption length. Once injected into the metal-oxide, electrons could be expected to move through the network of interconnected nanoparticles via conduction band states, although there could be barriers between individual grains. In fact, a density of trap states that increases exponentially towards the conduction band edge is found in the energy gap of these nanoporous electrodes[6] and the transport can be best described with a trapping/detrapping model[7]. Depending on the depth of the trap state the electron remains in a characteristic waiting time τ in the trap before it is thermally activated to the TiO_2 conduction band and hops to a neighboring trap site. A detailed description of diffusion across the oxide layer is an extremely complex issue which is matter of present investigations. We here just note that electron transport within the oxide layer is not only

an intrinsic property of the oxide itself. For instance, it has been argued that the density and energetic distribution of electron traps could depend also on the interaction between conduction electrons and electrolyte ions[8].

- Regeneration of the oxidized dyes (3)

After photoinduced electron injection, the dye is in its oxidized state and must therefore be regenerated, i.e. reduced by an electron donor in the electrolyte. In the case of the iodine/iodide redox couple, the diiodide radical ($I_2^{\cdot -}$) is formed upon reduction of the oxidized dye, which is subsequently converted into triiodide . Regeneration is in competition with reduction of the oxidized dye by an electron from TiO_2 (reaction 5). The regeneration efficiency is defined as the probability that an oxidized dye is regenerated by the electrolyte donor rather than by recombination with an electron from TiO_2. For the iodine redox couple, typical half times for regeneration are in the range of 100 ns to 10 µs, and strongly depends on the precise composition and concentration of the electrolyte. These lifetimes can usually ensure regeneration efficiencies close to one. Nevertheless, reaction 5 depends strongly on the concentration of electrons in the TiO_2. At high light intensities, back electron transfer to the dye may limit cell performance as in this case regeneration of the dye fails to compete effectively with it[9]. Recently, modification of the Co^{2+}/Co^{3+} redox system with ligands presenting bulky groups which function as insulating spacers, have been demonstrated to slow down the recombination process between the electrolyte and the titania, thus making this system competitive with the iodine-based one.

- Transport of the redox mediator and reduction of electron acceptors in the electrolyte at the counter electrode (4):

After oxidation, the I_3^- ions diffuse a short distance (<50 µm) through the electrolyte to the cathode. At the cathode, triiodide is reduce to iodide:

$$I_3^- + 2e^- \rightarrow 3I^-$$

The counter electrode must be catalytically active to ensure rapid reaction. The efficiency of a DSSC depends on different rate constants for iodine reduction at the front-and-counter electrode. The counter electrode is therefore usually covered by a thin layer of platinum, which acts as a catalyzer of iodine reduction: triiodide dissociated to iodine atoms upon adsorption, enabling a rapid one-electron reduction.

2.2 Energetics

The alignment of the energy levels at the oxide/dye/electrolyte interface is fundamental for the DSSC functioning. On one hand, it directly affects the V_{OC} and J values, on the other it also influences the kinetic balance between the concurrent processes discussed in paragraph 1.1.

As shown in Figure 2.1.1, the relevant energy levels are the semiconductor band edges and Fermi level, the HOMO and LUMO levels of the dye and the electrolyte redox potential. The dye HOMO-LUMO separation is obviously a fundamental parameter to be considered, as it determines the onset of light absorption. Moreover, for a DSSC device to work, the LUMO of the dye has to lie higher in energy than the CB edge of the oxide, while the HOMO must lie lower than the redox potential. It is important here to recognize that while semiconductor energies are measured in the "solid state physics" energy scale (i.e. referred to the vacuum level), the electrolyte and dye redox potentials are usually measured in the 'electrochemistry' scale (i.e. referred to the standard normal hydrogen electrode (NHE) potential). The difference between the potential of the NHE versus an electron in vacuum cannot be measured with thermodynamic rigor, but can be estimated as[10]:

$$E_{F,redox}[eV] = -(4.6 \pm 0.1) - eU_{redox}[V] \tag{2.2.1}$$

With this estimate, the standard potential of other redox couples can be expressed on the absolute (i.e., referred to vacuum) scale where both energy scales are reported.

In non-degenerate semiconductors, the equilibrium Fermi level is given by

$$E_F = E_C + k_B T ln \frac{n_c}{N_C} \tag{2.2.2}$$

where E_C is the energy at the conduction band edge, $k_B T$ is the thermal energy, n_c is the density of conduction band electrons, and N_C is the effective density of conduction band states. With respect to vacuum, E_C is given by the electron affinity E_A.

At equilibrium, the electrochemical potential of electrons across the interface must be constant. The electrochemical potential of the electrolyte is well-buffered by the high concentration of oxidized and reduced forms and does not change significantly under operation. The redox potential of the electrolyte forms therefore the zero of any measure of potential in the cell.

This means that when the semiconductor/electrolyte interface is formed, the Fermi level of the semiconductor becomes equal to the redox potential U_{redox} of the electrolyte.

Let us consider in detail what happens when an isolated nanocrystalline particle of TiO_2 is brought into contact with the redox electrolyte. For typical values of nanoparticle diameter (20 nm) and intrinsic n-type doping (n = 10^{18} cm^{-3} , due to oxygen vacancies) the Fermi level in the particle before immersion is close to the conduction band. The electron affinity of TiO_2 is typically 4.1 eV, so that I^-/I_3^- redox potential (in NHE) is located around 1 eV below the conduction band of the TiO_2. Consequently, electrons will be extracted from the n-doped particle until the electrochemical potentials (i.e. the Fermi levels) are equilibrated. This will leave the particle with a net positive charge associated with the ionized donors in the lattice. If the particle is small, the density of ionized donor states will now exceed that of the electrons by many orders of magnitude, and the particle will be fully depleted.

The alignment between the redox potential and the Fermi level implies a shift of the valence and conduction bands, i.e. a change in the semiconductor electron affinity and ionization potential energy, which should be taken into account when considering alignment with the other relevant energies.

When the cell is illuminated, a potential difference is created between the two electrodes and a photostationary state is produces. In this case, electrons and holes are in thermal equilibrium with the lattice but not with each other. It is therefore useful to introduce the concept of quasi Fermi level nE_F. The quasi Fermi level of electrons in the conduction band is related to their density n_c through the Fermi-Dirac function:

$$f_{FD} = \frac{1}{1 + e^{(E_c - nE_F)/K_B T}} \tag{2.2.3}$$

If (E_c-nE_F) is much greater than K_BT, the Fermi-Dirac distribution can be approximated by the Boltzmann distribution and the density of electrons in the conduction band is given by:

$$n_c = N_C e^{\frac{-(E_c - nE_F)}{K_B T}} \tag{2.2.4}$$

In the dark, the Fermi level in the TiO_2 is equal to the redox Fermi level, $E_{F,redox}$ and the (very low) electron density is

$$n_{c_0} = N_C e^{(\frac{-(E_c - E_{F,redox})}{K_B T})} \tag{2.2.5}$$

As illustrated in Figure 2.2.1 on page 17, the photovoltage is then given by the energy difference between the electrolyte redox potential and the quasi-Fermi level of the semiconductor:

$$qU_{photo} = (nE_F - E_{F;redox}) = K_B T \ln \frac{n_c}{n_{c_0}} \tag{2.2.6}$$

Due to the presence of trapping states below the conduction band edge, the position of the quasi Fermi level is typically near E_C.

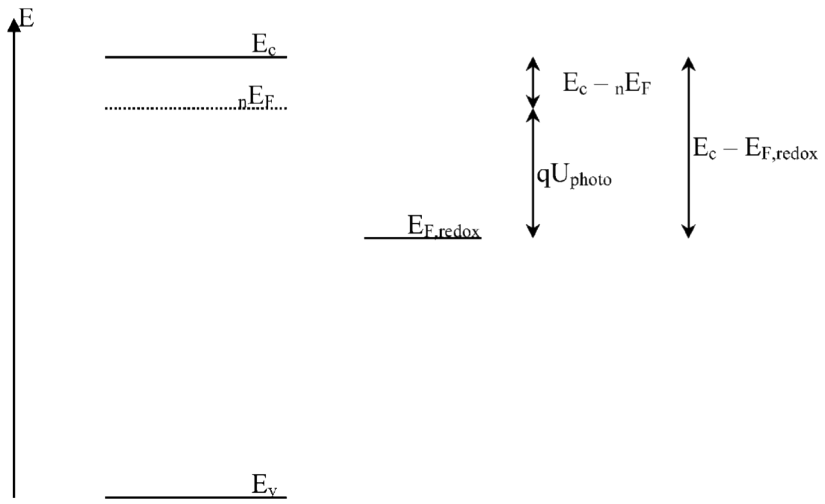

Figure 2.2.1: Energy diagram illustrating relationship between the electrolyte redox potential and the quasi-Fermi level of the semiconductor.

Equation 2.2.6 clearly shows that to increase the photovoltage we need to increase the electron density under illumination n_c. This increase can be achieved by increasing the electron lifetime τ_n and/or the distance between E_c and $E_{F,redox}$.

As explained previously, the maximum attainable photovoltage V_{OC} is obtained when the total current is zero, i.e. when the electron current injected from the dye equals the electron transfer in the opposite direction. Three routes can be identified for back transfer: (i) transfer of electrons from the mesoporous TiO_2 layer to ions in the electrolyte; (ii) transfer of electrons from the mesoporous oxide to oxidized dye molecules attached to the surface, and (iii) transfer to I_3 ions via the substrate. Usually, both routes (ii) and (iii) can be neglected, while the rate of electron transfer to I_3 ions is the dominant quantity that determines the open circuit voltage at high light intensities. In this approximation, the open circuit condition can be defined in terms of the electron injection rate v_{inj} and the recombination rates of route (i) $v_{I_3^-}$, as: $v_{inj} = v_{I_3^-}$. The rate of electron injection is determined by the light intensity and the surface coverage of adsorbed dye and can be expressed as

$$v_{inj} = \eta_{inj} \alpha I_0 e^{-\alpha x} \tag{2.2.7}$$

where η_{inj} is the efficiency of electron injection from the dye excited state, and α is the absorption coefficient, related to the effective molar concentration c and molar absorption coefficient ε(l) of the dye. The recombination rate is given by:

$$v_{I_3^-} = k_{I_3^-} n_c [I_3^-] \tag{2.2.8}$$

where $k_{I_3^-}$ is the constant and $[I_3^-]$ is the ion concentration in the electrolyte. The open circuit condition therefore sets the value for n_c as

$$n_c = \frac{v_{inj}}{k_{I_3^-}[I_3^-]} = v_{inj}\tau_n \tag{2.2.9}$$

It can be seen that this simple approach predicts that the steady state electron density is linearly proportional to the illumination intensity and to the electron lifetime, which in turn depends on the efficiency of the back transfer reactions. It is therefore clear from this discussion that one way to increase the open circuit voltage is to decrease the concentration of I_3^-. However, this will impose restrictions on the maximum (diffusion limited) current that the cell can deliver. An alternative is to reduce the rate constant for electron transfer by modification of the surface of the TiO_2 particles with blocking layers.

The energy position of the LUMO relative to the CB and of the HOMO relative to the redox potential has also to be optimized, as they influence the kinetics of the injection and reduction processes. For optimum performances, a certain excess energy δE_{inj}(i.e. energy difference between these levels) is required. This indeed provides the driving force for electron injection. The magnitude of the required offset has not been precisely determined but is likely to be around 100 - 150 mV. This offset can be tailored by changing the position of E_c relative to the excited state. On the other hand an exceedingly high value of δE_{inj}, obtained by lowering E_c, may not be beneficial for the performance of the DSC device, because it will in turn correspond to a net decrease of $E_c - E_{F,redox}$, i.e. of V_{OC}.

Similarly the relative energy position of the HOMO level relative to the redox potential has to be fine-tuned to optimize efficiency.

2.2.1 Tuning of the energy level alignment

We have shown in the previous paragraph how improved energy alignment of the LUMO with the oxide CB, and of the HOMO with the redox potential of the electrolyte, could improve efficiency and provide new options in the design of photovoltaic cells. The ability to finely tune the energy level alignment is therefore extremely important to optimize device performances. Actually, the main practical route to tune energy level alignment across the extended interface is usually to add to the electrolyte bath a range of different moieties. These additives have the capability to shift the semiconductor conduction band, thus altering the driving force between the dye LUMO and E_c.

In fact, it is important to recognize that other factors, such as intermolecular interactions and molecular orientation, can significantly alter the alignment. Particularly relevant are the shift of the semiconductor bands relative to the vacuum level, which can be induced by the formation of a dipole layer at the dye/oxide interface. It is indeed well known that molecular adsorption can induce significant changes in ionization potential and work function (W_F) both in the case of semiconductor[11] and metal surfaces[12, 13, 14, 15], especially when molecules with significant permanent dipole moments are considered. This effect has been indeed investigated in particular in the case of solid state heterojunction solar cells[16, 17, 18, 19]. In the specific case of DSSCs, few reports have shown a modification of V_{OC}, attributed to the intrinsic dipole moment of the molecular sensitizer[20] or of co-adsorbed small molecules[21]. In particular De Angelis et al.[20] investigated the DSSC performances for several types of Ru-complex dyes, (derived from N3 or N719) differing only by their side functional chains. They observed small V_{OC} variations, which were attributed, on the basis of theoretical calculations, to the different values and orientation of the dipole moment of each molecular dye.

2.3 Materials

2.3.1 Photosensitizing Dye

Dyes employed in highly efficient DSSC should fulfill some essential characteristics:

(1) The absorption spectrum of the photosensitizer should cover the whole visible region and part of the near-infrared (NIR).

(2) The photosensitizer should have anchoring groups to assure strong binding to the semiconductor surface.

(3) the HOMO and LUMO energies should be properly located relative to the redox potential and to the oxide conduction band.

(4) Unfavorable dye aggregation on the semiconductor surface should be avoided through optimization of the molecular structure of the dye or by addition of ligands or co-adsorbers that prevent aggregation.

(5) For long-term performances, the photosensitizer should be photostable, and electrochemical and thermal stability are also required.

The best dyes contain both electron-rich (donor) and electron-poor (acceptor) sections connected through a conjugated (π) bridge. The electron-poor section is typically functionalized with an acidic binding group that couples the molecule to the oxide surface. Photoexcitation causes a net electron transfer from the donor to acceptor sections such that the electron wavefunction couples to the titania conduction band states, while the hole wavefunction resides mostly away from the oxide surface, where it is well-positioned to interact with the redox couple. In other terms, this structure ensures that electron density in the excited state is concentrated in the vicinity of TiO_2, promoting injection and localizing the resultant positive charge away from the interface. Alkyl chains are also often attached to the side of the dye to create a barrier between holes in the redox couple and electrons in the titania, thereby inhibiting recombination.

There have been several thousand different sensitizing dyes trialled in DSSCs, making a complete assessment of sensitizers difficult to provide. In the following we will therefore briefly review the characteristics of the most extensively studied dye, i.e. Ruthenium

organometallic complexes and of the interesting class of phthalocyanine and porphyrin-based sensitizers.

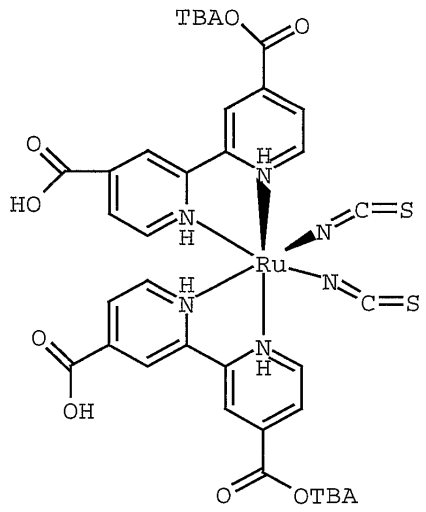

Figure 2.3.1: Ruthenium N-719 dye.

Ruthenium organometallic complexes are certainly the most extensively investigated dyes, due to the high power conversion efficiency. The N719 dye (see Figure 2.3.1) is the most used Ruthenium complex and shows highly efficient electron injection, due to a long lived triplet excited state, absorption of light over a broad wavelength range ($\Delta\lambda = 350$ nm) and extremely slow recombination[22, 23]. On the other hand, it is characterized by low molar extinction coefficients (10,000 - 20,000 M^{-1} cm^{-1}). and extremely weak absorption at the band-edge (around 780 nm), which restricts NIR light harvesting.

Organic dyes generally have substantially higher molar extinction coefficients (50,000 -200,000 M^{-1} cm^{-1}) than ruthenium- based complexes, but typically have narrower spectral bandwidths ($\Delta\lambda = 100 - 250$ nm).

Porphyrins and phthalocyanines are also interesting candidates as sensitizers for DSSCs. They represent an intermediate case between metal transition complexes and purely organic dyes. Their advantages mainly reside in their thermal photo- and electro-chemical stability and to their excellent light-harvesting properties, due to high extinction coefficient. Moreover, porphyrin and phthalocyanine systems exhibit intense spectral response bands in the near-IR region: they are indeed characterized by a Q-band absorption in the

700 nm region, which makes them good candidates as panchromatic photosensitizers for DSSCs.

On the other hand, due to their large π-conjugated structure, these sensitizers have a marked tendency towards aggregation in solution and on the surface of TiO_2: this is one of the reasons why they have generally shown low efficiency in DSSCs.

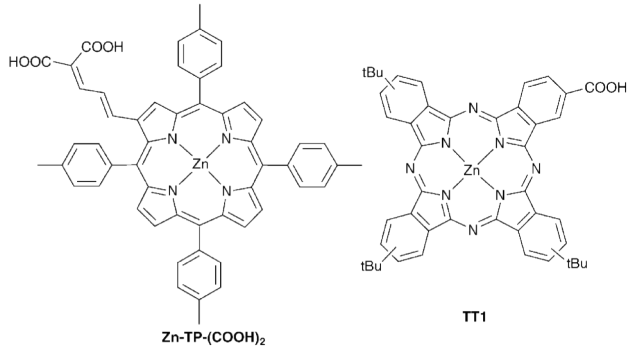

Figure 2.3.2: Zn-TP-$(COOH)_2$ and TT1 structures

Moreover, due to their symmetrical structures, porphyrins and phthalocyanines display an inherent lack of directionality in the excited state. Better excited state directionality can be achieved by breaking the symmetry of these large planar systems and designing unsymmetrical complexes such as Zn-TP-(COOH) and TT1 (Figure 2.3.2), which have been two of the most efficient porphyrin and phthalocyanine dyes utilized in DSSCs, with efficiencies of 7.1% and 3.5% respectively.

On the other hand, very recently, Graetzel and co-workers reported on a more than 12% efficiency DSSC, which exploits a porphyrin-based dye, in combination with a Cobalt(II/III)-based redox system[3]. This result clearly demonstrate that real efficiency improvement can only be obtained taking into account and carefully tailoring the complex interplays between the different cell components.

Eventually, we should mention that great opportunities for improving efficiency derive from the use of co-sensitizers and energy relay dyes. In co-sensitization, dye moieties with different absorption spectra are co-adsorbed on the oxide. The most significant challenge

of co-sensitization using NIR dyes is maintaining a large V_{OC}, which requires that each dye adequately prevents recombination. The problem of V_{OC} reduction is likely to be even more pronounced with NIR dyes because they have small band-gaps. The resulting energy and hole transfer from neighbouring visible sensitizing dyes can increase recombination and lower V_{OC}[24].

Energy relay dyes (ERDs) instead decouple the light-harvesting and charge-transfer processes: ERDs absorb sunlight and then transfer energy non-radiatively to the sensitizing dyes, which are responsible for charge separation[25, 26]. ERDs have been placed inside the electrolyte and the semiconductor, co-sensitized[24] on the semiconductor surface, and tethered to sensitizing dyes[26]. The use of ERDs has several important advantages over co-sensitization. In particular, as ERDs do not participate in the charge-transfer process, they do not require precise energy level alignment for charge transfer. Moreover, ERDs do not need to attach to the semiconductor surface in order to contribute to light-harvesting, and thus their addition can both widen and strengthen the overall absorption spectrum for the same film thickness.

2.3.1.1 Anchoring Group

Most of the properties of sensitizers does not rely only on the dye characteristics, but can be strongly affected by the interaction between the semiconductor substrate and the dye itself. To this regard, the choice of the most suitable anchoring group for each dye/semiconductor interface is clearly of great relevance. Several types of anchoring groups have been trialled for DSSCs. The binding interaction can in principle occur through hydrogen bonding mechanisms, as well as electrostatic interactions and hydrophobic interactions, although these provide only a weak electronic interaction with the semiconductor. More commonly, the anchoring group is designed to form a permanent chemical bond with the semiconductor. Strong anchoring of the dyes is indeed essential for long-term stability. Desorbed dyes can lead to an unwanted filter effect, dye degradation and decrease of the counter electrode performance. Moreover, to facilitate electron transfer from the dye into the semiconductor,

the ligand could be conjugated and display an electron withdrawing character.

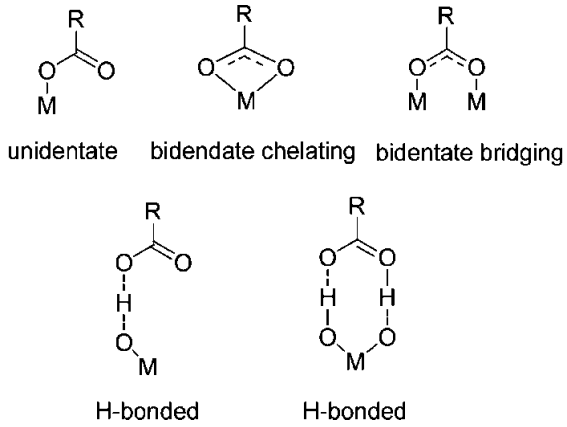

Figure 2.3.3: Binding modes for carboxylate unit on TiO_2 surface.

Typically, the anchoring group is chosen for its ability to react with surface hydroxyl groups of the semiconductor oxide to form chemical bonds. The standard anchoring group for sensitizers is carboxylic acid (-COOH). Its derivatives, such as ester, acid chloride, acetic anhydride, carboxylate salt, or amide, have also been used. There are different binding modes between the oxide surface and the carboxylic acid[31]. In general, the carboxylic acid group can coordinate to the TiO_2 surface in three ways:[32, 33] unidentate mode, chelating mode, and bridging bidentate mode. The binding modes can be determined by the molecular structure and adsorption environment[34]. The bidentate structure is superior to unidentate structure in the stability of the anchored dye and interfacial quantum yields of electron injection due to the intimate contact with the semiconductor surface[33].

Other chemical moieties employed for anchoring purpose include sulfonic acids (R-SO_3H)[28], phosphonic acids (R-PO_3H)[29], and Catechols[30] ($C_6H_4(OH)_2$). The latter will be fully addressed in section 3.3

2.3.2 Semiconducting Oxide

When choosing the semiconductor in DSSCs, several factors have to be considered. First, the semiconductor must have conduction band energy and density of states that allow efficient electronic coupling with the dye energy levels. These conditions facilitate charge separation and minimize recombination. Second, the semiconductor morphology must present high surface area to maximize light absorption by the dye monolayer, while maintaining good electrical connectivity to the substrate. During the last years, large efforts have been paid to optimize the morphology of the nanostructured electrode and a large range of nanostructures has been tested, spanning from random assemblies of nanoparticles to organized arrays of nanotubes and single-crystalline nanorods. These studies are motivated by the expectation of an improved and directed charge transport along the rods and tubes and by an improved pore filling of hole conductor materials for solid-state DSSC.

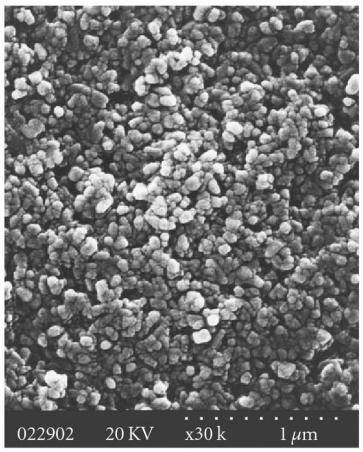

Figure 2.3.4: A top-view SEM image of rutile - TiO_2 electrodes.

Currently, TiO_2 still gives the highest efficiencies. However, replacing of TiO_2 with alternative oxides, such as ZnO, SnO_2, and Nb_2O_5 on one hand, and ternary oxides ($SrTiO_3$ and Zn_2SnO_4) as well as core-shell structures (as for instance ZnO-coated SnO_2) is currently widely investigating. Indeed, some advantages can be expected in replacing TiO_2 with other materials. TiO_2 is for instance characterized by slow charge transport, due to

poor mobility. Other systems such as WO_3, ZnO, or SnO_2 have a much higher electron mobility, and in some cases a higher injection yield. Moreover, reducing the conduction band energy level of the semiconductor will lead to more efficient electron injection from dyes with low LUMO energies. To this aim, materials such as SnO_2, In_2O_3, or WO_3, which possess a lower ECB value than TiO_2, has been taken into consideration.

Zinc oxide (ZnO) is one of the most promising alternative candidate to TiO_2 in DSSCs. It has similar electronic properties, but is characterized by a much higher electron mobility. ZnO can be rather easily and inexpensively grown in a large variety of nanostructured morphologies, such as nanowires, nanorods, tetrapods and branched nanostructures, via a wide range of techniques. Nanostructures of ZnO have been demonstrated to be advantageous if used as photoelectrode film in DSSCs. They can offer larger specific surface areas for dye adsorption than bulk film material, direct pathways for electron transport, and light-scattering effects that extend the traveling distance of light within the photoelectrode film.[35]

On the other hand, the chemical stability of ZnO is rather poor compared with that of TiO_2 as it tends to dissolve under acid conditions. The resulting Zn^{2+} ions form insoluble complexes with dye, causing precipitation of these complexes in the pores of the film. This determines a decrease in the net yield for charge carrier injection. Thus, careful control of the dye adsorption conditions is necessary for ZnO-based DSSCs and preferably, sensitizers with an anchoring group without protons should be developed. Notably, some organic dyes do not precipitate in the presence of Zn^{2+} ions and can therefore be used more easily in combination with ZnO.

Moreover, for ZnO with Ru-based dyes, the electron injection is dominated by slower components relative to TiO_2, leading to a difference of more than 100 times in the injection rate constant. The different injection dynamics most likely originate from the conduction-band structures of the semiconductors. That is, the ZnO conduction bands are largely derived from the empty s and p orbitals of Zn 2p, while the TiO_2 conduction band is comprised primarily of empty 3d orbitals from Ti 4p[36]. The difference in band structure results in a different density of states and, possibly, different electron coupling strengths.

Indeed, the density of conduction band states near the band edge is as much as two orders of magnitude higher in TiO_2, due to the larger effective mass of the conduction-band electron in TiO_2 than that in ZnO.

Bibliography

[1] B. O'Regan, M. Graetzel, Nature, 1991, 353, 737.

[2] M. K. Nazeeruddin, F. De Angelis, S. Fantacci, A. Selloni, G. Viscardi, P. Liska, S. Ito, B. Takeru, M. Gratzel J. Am. Chem. Soc. 2005, 127, 16835.

[3] A. Yella, H-W Lee, H. N. Tsao, C. Yi, A. K. Chandiran, Md.K. Nazeeruddin, E. W-G Diau, C-Y Yeh, S. M. Zakeeruddin, M. Grätzel Sci. 2011, 334, 629.

[4] Hagfeldt, A.; Boschloo, G.; Sun, L.; Kloo,L.; Pettersson, H.; Chem. Rev. 2010, 110, 6595.

[5] S. Koops, B. C. O'Regan, P. R. F. Barnes, J. R. Durrant, J. Am. Chem. Soc. 2009, 131, 4808.

[6] B. O'Reagan, S. Scully, A.C. Meyer, J. Phys. Chem. B, 2005, 109, 4616.

[7] J. Nelson, Coord. Chem. Rev., 2004, 248, 118.

[8] L. M. Peters Phys. Chem. Chem. Phys., 2007, 9, 2630.

[9] S. A. Haque, Y. Tachibana, R. L. Willis, J. E. Moser, M. Graetzel, D. R. Klug, J. R. Durrant J. Phys. Chem. B 2000, 104, 538.

[10] R. Memming Semiconductor Electrochemistry; Wiley VCH: Weinheim, Germany, 2001.

[11] R. Schlesinger, Y. Xu,O. T. Hofmann, S. Winkler, J. Frisch, J. Niederhausen, A. Vollmer, S. Blumstengel, F. Henneberger, P. Rinke, M. Scheffler, N. Koch, Phys. Rev B 2013, 87, 155311.

[12] H. Ishii, K. Sugiyama, E. Ito, K. Seki, Adv. Mater. 1999, 11, 8.

[13] R. W. Zehner, B. F. Parsons, R. P. Hsung, L. R. Sita Langmuir 1999, 15, 1121.

[14] V. De Renzi, R. Rousseau, D. Marchetto, R. Biagi, S. Scandolo, U. Del Pennino, Phys. Rev. Lett. 2005, 95, 046804.

[15] V. De Renzi, Surf. Sci. 2009, 603, 1518.

[16] A. Tada, Y. Geng, Q. Wei, K. Hashimoto, K. Tajima, Nat Mat. 2011, 10, 450.

[17] J. Krueger, U. Bach, M. Graetzel, Adv. Mater. 2000, 12, 447.

[18] C. Goh, S. R. Scully, M. D. McGehee, J. Appl. Phys. 2007, 101, 114503.

[19] U. B. Cappel, S. Plogmaker, E. M. J. Johansson, A. Hagfeldt, Phys. Chem. Chem. Phys. 2011, 13, 14767.

[20] F. De Angelis, S. Fantacci, A. Selloni, M. Gratzel, M. K. Nazeeruddin Nano Lett., 2007, 7, 3189.

[21] S. Ruehe, M. Greenshtein, S.-G. Chen, A. Merson, H. Pizem, C. S. Sukenik, D. Cahen, A. Zaban, J. Phys. Chem. B 2005, 109, 18907.

[22] A. J. Mozer, P. Wagner, D. L. Officer, G. G. Wallace, W. M. Campbell, M. Miyashita, K. Sunaharac, S. Mori, Chem. Comm., 2008, 4741.

[23] R. Katoh, M. Kasuya, A. Furube, N. Fuke, N. Koide, L. Han, Chem. Phys. Lett., 2009, 471, 280.

[24] B. E. Hardin, A. Sellinger, T. Moehl, R. Humphry-Baker, J.-E. Moser, P. Wang, S. M. Zakeeruddin, M. Graatzel, M. D. McGehee J. Am. Chem. Soc. 2011, 133, 10662.

[25] B. E. Hardin, E. T. Hoke, P. B. Armstrong, J.-H. Yum, P. Comte, T. Torres, J. M. J. Frechet, Md K. Nazeeruddin, M. Graetzel, M. D. McGehee Nature Photon. 2009, 3, 406.

[26] C. Siegers, J. Hohl-Ebinger, B. Zimmermann, U. Würfel, R. Mülhaupt, A. Hinsch, R. Haag Chem. Phys. Chem. 2007, 8, 1548.

[28] D. H. Taffa, M. Kathiresan, T. Arnold, L. Walder, M. Erbacher, D. Bauer, F.- P. Montforts, J. Nordmann, M. Haase, J. Photochem. Photobiol. A, 2010, 216, 35

[29] P. Wang, C. Klein, J.-E. Moser, R. Humphry-Baker, N.-L. Cevey-Ha, R. Charvet, P. Comte, S. M. Zakeeruddin, M. Graetzel, J. Phys. Chem. B, 2004, 108, 17553.

[30] B.-K. An, W. Hu, P. L. Burn, P. Meredith, J. Phys. Chem. C, 2010, 114, 17964.

[31] E. Galoppini, Coord. Chem. ReV. 2004, 248, 1283.

[32] Z. S. Wang, K. Hara, Y. Dan-Oh, C. Kasada, A. Shinpo, S. Suga, H. Arakawa, H. Sugihara, J. Phys. Chem. B 2005, 109, 3907.

[33] M. K. Nazeeruddin, R. Humphry-Baker, P. Liska, M. Graetzel, J. Phys. Chem. B, 2003, 107, 8981

[34] H. N. Tian,X. C. Yang, R. K. Chen, R. Zhang, A. Hagfeldt, L. J. Sunt, J. Phys. Chem. C 2008, 112, 11023.

[35] Q. Zhang, C. S. Dandeneau, X. Zhou, G. Cao Adv. Mater. 2009, 21, 4087.

[36] R. van de Krol, A. Goossens, E. A. Meulenkamp, J. Appl. Phys. 2001, 90, 2235.

Chapter 3

Dye/metal-oxide model systems

In this chapter the literature on some relevant dye/metal-oxide model systems is briefly reviewed. We will mainly focus on those results which provide better understanding of the basic mechanisms which govern energy alignment at dye/semiconductor interface. We are in particular interested in the interfaces formed by catechol and phthalocyanines on the ZnO non polar surfaces. Nevertheless, as only few works have addressed in details details these interfaces, while the most studied dye/oxide interfaces are those where TiO_2 surfaces are involved, we will also review the main results regarding these systems.

3.1 TiO_2 structural and electronic properties

TiO_2 exists naturally in three crystalline polymorphs, namely rutile (tetragonal a = b = 4.58 Å, c = 2.953 Å), anatase (tetragonal, a = b = 3.78 Å, c = 9.50 Å) and brookite (rhombohedral, a = 5.44 Å. b = 9.17 Å, c = 5.14 Å). Rutile is the most stable TiO_2 polymorph. Only rutile and anatase play a significant role in the applications of TiO_2 which are here of interest.

A schematic diagram of the rutile and anatase bulk structure is shown in Figure 3.1.1.

In both structures, the basic building blocks consist of a titanium atom surrounded by six oxygen atoms in a more or less distorted octahedral configuration. In both TiO_2

structures, the stacking of the octahedron results in threefold coordinated oxygen atoms. The most stable and therefore most studied surfaces of the two polymorphs are the rutile (110) and anatase(101).

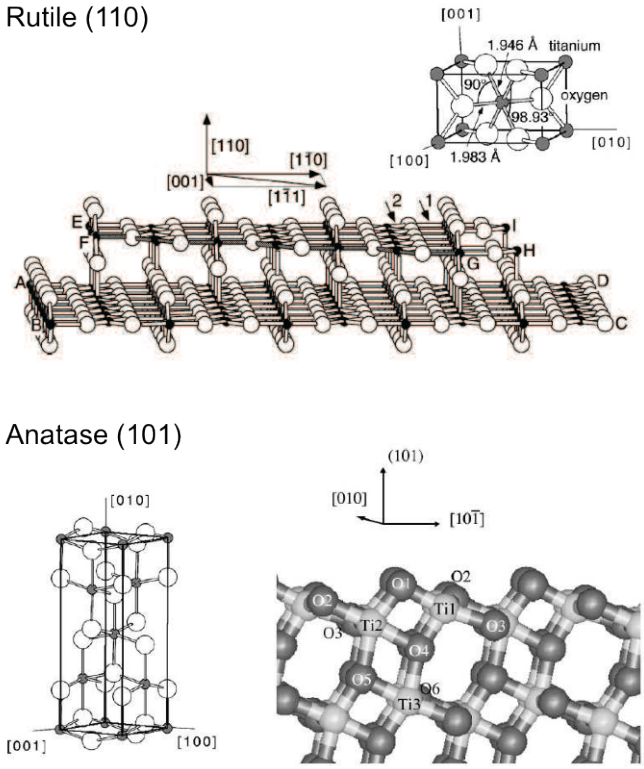

Figure 3.1.1: Top of the panel: the structure of the rutile stoichiometric (110) surface. Bottom of the panel: The structure of the anatase stoichiometric (101) surface.

The rutile (110)-(1x1) surface shown in Figure 3.1.1 contains two different kinds of titanium atoms. Along the [001] direction, rows of six fold coordinated Ti atoms (as in the bulk) alternate with fivefold coordinated Ti atoms, with one dangling bond perpendicular to the surface. Two kind of oxygen atoms are present as well. Within the main surface plane, they are threefold coordinated as in the bulk. The so-called bridging oxygen misses one bond to the Ti atom in the removed layer and is twofold coordinated.

The anatase(101) surface, which is shown in Figure 3.1.1, is very corrugated with a characteristic sawtooth profile perpendicular to the [010] direction. On it, both fivefold- and sixfold-coordinated Ti-atoms are present (denoted Ti1 and Ti2, respectively), as well

as twofold and threefold oxygens (O1 and O2, respectively). Each bridging oxygen (O1) is bonded to one Ti1 atom and one Ti2 atom.

The band gap of TiO_2 is about 3.0 eV for rutile and 3.2 eV for anatase, respectively. Since titanium-oxide has many stable chemical phases with a variety of crystal structures, TiO_2 can be reduced easily. Bulk reduction and the resulting color centers are reflected in a pronounced color change of TiO_2 single crystals from initially transparent to light and dark blue. The bulk structure of reduced $TiO_{2\text{-x}}$ is quite complex with various types of defects such as doubly charged oxygen vacancies, Ti^{3+} and Ti^{4+} interstitials, and planar defects. The defect structure varies with oxygen deficiency. These intrinsic defects result in n-type doping and high conductivity.

3.2 Zinc Oxide structural and electronic properties

Zinc oxide is a II–VI semiconductor, which has attracted a significant amount of attention in the past several years since it finds a number of applications in catalysis, gas sensing, and fabrication of microelectronic devices. In particular, ZnO has been actively sought as a replacement for the TiO_2 electrodes[1] in DSSCs. Indeed, the energy gap of ZnO is comparable with that of TiO_2, i.e. 3.37 eV, while its electron mobility is much higher than that of TiO_2. As for TiO_2, also ZnO presents usually an n-doped character, due to the presence of bulk defects and oxygen vacancies.

The lowest energy structure of ZnO is hexagonal wurtzite. In the hexagonal wurtzite crystal structure each Zn^{2+} ion is surrounded by a tetrahedron of four O^{2-} ions, and vice-versa[2]. This structure can be described schematically as a number of alternating planes of O and Zn ions stacked along the c-axis. Four low-index surfaces are of interest: the non polar $(1\ 0\ \bar{1}\ 0)$ and $(1\ 1\ \bar{2}\ 0)$ surfaces, and the polar $(0\ 0\ 0\ 1)$-Zn and $(0\ 0\ 0\ \bar{1})$-O surfaces. The non-polar surfaces are formed by breaking the same number of oxygen and zinc bonds and they contain an equal number of O and Zn ions, whereas the polar surfaces are either Zn or O terminated.

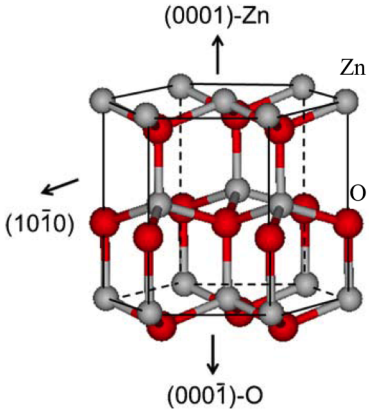

Figure 3.2.1: Schematic structure of ZnO with a stacking sequence of Zn and O layers.

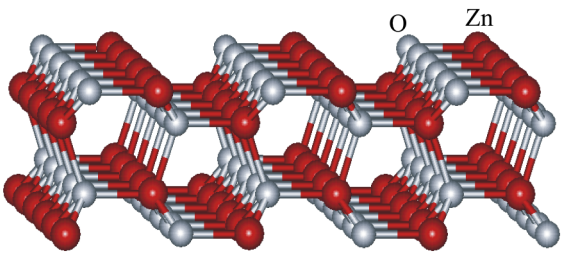

Figure 3.2.2: Structure of a bulk-truncated mixed-surface ZnO(10$\bar{1}$0)

The non-polar ZnO(10$\bar{1}$0) surface is, in contrast to its polar counterparts, electrostatically stable and does not reconstruct. This mixed-terminated surface is the energetically most favourable surface. It is therefore the most exposed surface in all ZnO crystal nanostructures. It is characterized by slightly tilted ZnO dimers, which are formed by threefold coordinated Zn and O atoms, as shown in Figure 3.2.2

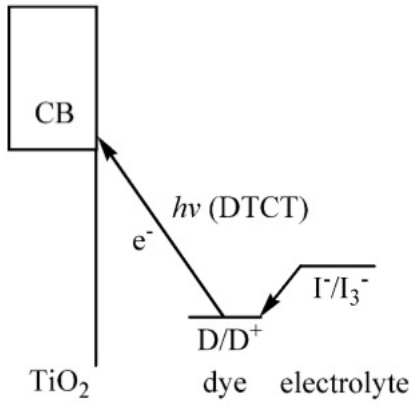

Figure 3.3.1: Types - II of electron injection pathways from an desorbed dye to TiO_2 in DSSC

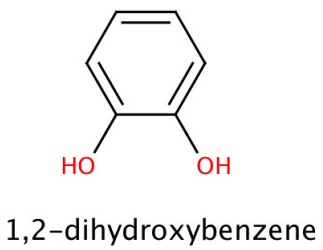

Figure 3.3.2: Structure of the catechol molecule

3.3 Catechol/metal-oxide interfaces

3.3.1 An introduction to catechol

The catechol molecule ($C_6H_4(OH)_2$) is one of the smallest organic sensitizing chromophores. It consists of a benzene ring and two hydroxyl groups. There are two main reasons that motivate the investigation on catechol adsorption on both TiO_2 and ZnO substrates.

First of all, catechol can be used in DSSC as an anchoring group for the dye molecules and has received particular attention because its binding to TiO_2 is stronger than any other type of anchoring group[3].

Moreover, optical absorption measurements showed that the onset of absorption of catechol-functionalized TiO_2 and ZnO nanocrystallites is red-shifted compared to unmod-

ified nanoparticles[3]. For instance, Duncan and Prezhdo have performed optical absorption measurements on free and bound catechol molecules on anatase TiO_2 (101) [4]. The spectra of their optical absorption measurements are shown in Figure 3.3.3. In free catechol the transition from the HOMO to the LUMO determines an absorption band at 270 nm. This band can be still observed in bound catechol. The spectra of bound catechol possess an additional absorption band at 420 nm. Similar results have been reported also in the case of catechol/ZnO adsorption[5, 6, 7]. The presence of this new band can be explained considering the catechol/metal-oxide interface as a typical example of the so called Type-II interfaces. In this kind of interfaces (see Figure 3.3.1) the HOMO of the molecule is localized within the semiconductor gap, while the LUMO lies above the CB edge. Low-energy absorption takes place when the excited HOMO electron passes directly from the dye to the metal-oxide conduction band.

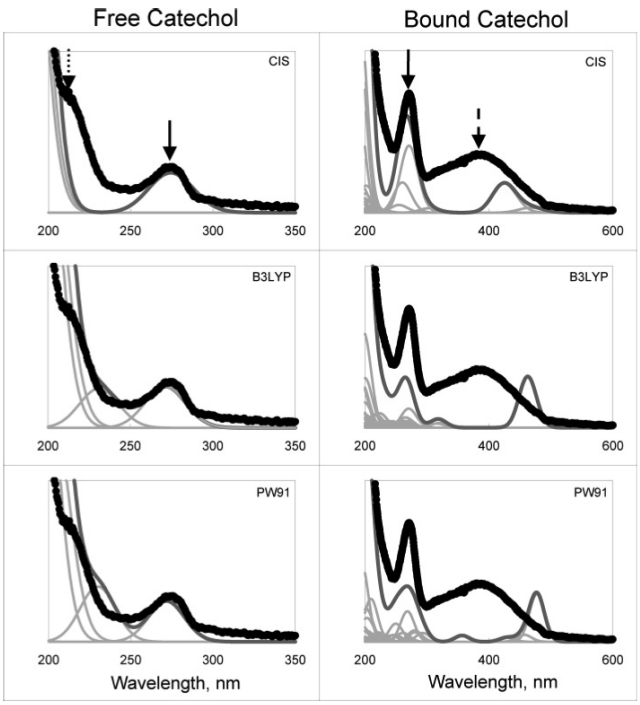

Figure 3.3.3: Spectra of free and bound catechol measured experimentally (black dots merging into a thick black line) and calculated theoretically (gray lines) by several ab-initio approaches, as indicated in the plots and detailed in the main text. The left column corresponds to free catechol, while the right column represents bound catechol.

In order to understand in details both the mechanism of molecular adsorption and the electronic properties of catechol/metal-oxide interfaces, several works have investigated the model systems in which catechol moiety is adsorbed on well-defined semiconductor single crystal surfaces, i.e. mainly rutile $TiO_2(110)$ and anatase $TiO_2(101)$. Only few works dealt with catechol adsorption on ZnO and, to the best of our knowledge, no experimental structural investigation has been performed.

3.3.2 How catechol adsorbs on TiO_2

When catechol adsorbs on a rutile $TiO_2(110)$ surface, the H atoms from both hydroxyl groups are split off and donated to bridge-bonded surface O atoms. This results in a catecholate entity bonded to neighbouring surface Ti sites via two Ti-O bonds[8].

A combined theoretical and experimental (STM, photoemission) study of catechol adsorption on rutile $TiO_2(110)$ found that at saturation catechol forms an ordered (4×1) overlayer. This structure is attributed to catechol adsorbed on rows of surface Ti atoms with the molecular plane tilted from the surface normal in an alternating fashion. This superstructure corresponds to two different full-coverage H-bonded structures, comprising either monodentate only or mixed monodentate-bidentate molecules. These two structures can easily convert from one into the other via proton exchange between the surface and the adsorbed catechol.[9]

Photoemission and near-edge X-ray absorption fine structure (NEXAFS) techniques have been used by Syres et al. to study the adsorption of catechol on anatase $TiO_2(101)$ and rutile $TiO_2(110)$ single crystals. Photoemission results confirm the catechol molecule adsorbs on both surfaces predominantly in a bidentate geometry. The carbon K-edge NEXAFS spectra recorded for catechol on anatase TiO_2 (101) and rutile $TiO_2(110)$ showed that the phenyl rings of the molecule are oriented roughly 30° from the surface normal for both substrates[10].

Diebold, Selloni and co-workers[11] have deeply investigated the growth and the organization of a catechol monolayer on the anatase (101) surface with scanning tunneling

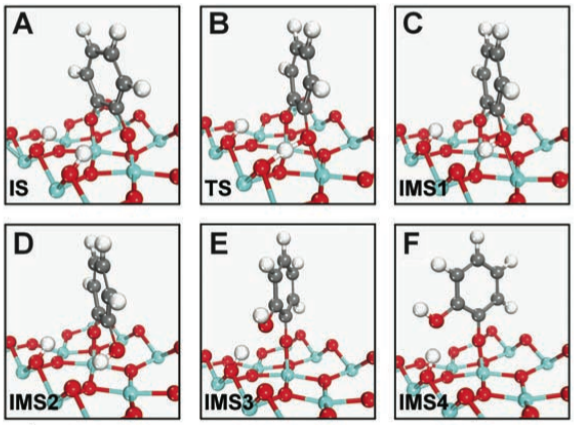

Figure 3.3.4: Calculated rotational (clockwise) pathway of a catechol on $TiO_2(110)$ with the lowest E_{act}. (A) Initial state of a catecholate adsorbed on a $TiO_2(110)$ surface: The catechol is fully dissociated, and the H's split off from both the OH groups sit on the neighboring O row. (B) TS: One O catechol-Ti5c bond is broken and a H atom is back-transferred from one of the O2c atoms. (C to F) The following IMSs during the first half of the rotation[9].

microscopy and density functional theory calculations. They found that isolated molecules adsorb preferentially at steps, while additional molecules are distributed across the terraces. In the low coverage limit molecules adsorbed on terraces are preferentially sticked to subsurface defect sites. Indeed, calculations showed an enhancement of the catechol adsorption energy in close proximity of the subsurface defects.

As on rutile (110), the three basic adsorption geometries of catechol on anatase (101) surface correspond to undissociated molecular (D0), dissociated monodentate (D1), and dissociated bidentate (D2) adsorption. By DFT calculations the lowest- energy configuration for each of these geometries were identified. In the D1 and D2 configurations, one proton resulting from the dissociation is transferred to a neighboring surface O site on the left, and the molecular benzene-like ring is slightly tilted toward the resulting bridging hydroxyl. In D1, the undissociated OH forms a hydrogen bond (H-bond) with another O atom on the right, and in D2, the proton of the OH group is transferred to that O. Both monodentate (D1) and bidentate (D2) conformations are present in the dilute limit, and frequent interconversions can take place between these two species. With increasing catechol exposure, molecules assemble into small islands. These islands are strongly

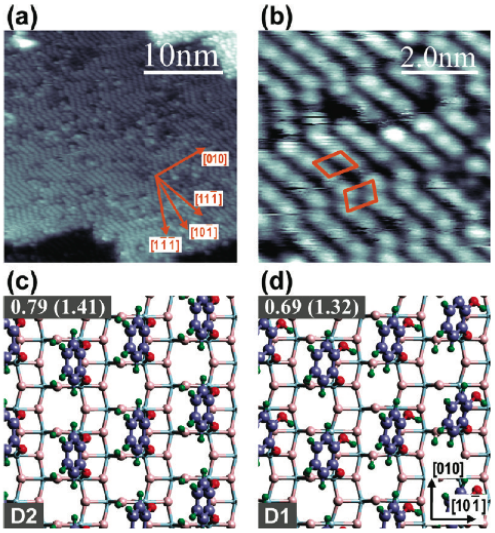

Figure 3.3.5: Full monolayer of catechol on anatase $TiO_2(101)$. STM images (U_{sample} = +1.9 V, I_{tunnel} = 0.17 nA) (a, b). DFT results of a layer of (c) fully dissociated (D2) and (d) partially dissociated (D1) molecules. The computed adsorption energies (in eV) per molecule are indicated[11].

elongated; often they consist of just a single molecular chain. By further increasing the coverage, the islands grow in size, always maintaining an elongated shape. At full coverage, a (2×1) overlayer evolves with nm-sized domains. The mechanism of island growth can be described as follows: initially, D1 catechols are mobile at room temperature and can explore the most favorable surface adsorption sites, whereas D2 are essentially immobile. When a D1 molecule arrives in proximity of another adsorbed catechol in an adjacent row, it is energetically convenient for them to pair up in nearest- neighbor positions taking a D2-D2 or D2-D1 configuration. This intermolecular interaction, which is largely substrate mediated, causes the formation of one-dimensional catecholate islands that can change in shape but are stable to break-up. As we shall see in the following paragraph, the details of adsorption mechanisms on TiO_2 surfaces have been shown to strongly affect also the energy level alignment across the interface.

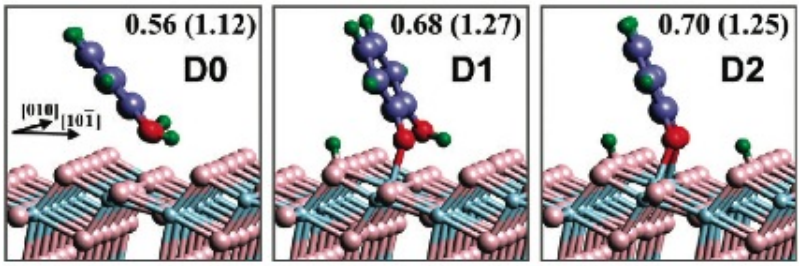

Figure 3.3.6: Adsorption configurations of isolated catechol molecules on anatase $TiO_2(101)$. (a) Molecularly adsorbed 'D0', (b) singly dissociated 'D1', and (c) doubly dissociated 'D2'[11].

3.3.3 Electronic properties of catechol/TiO_2 interfaces

Several work have addressed the electronic properties of the catechol/TiO_2 interface. In the case of catechol adsorption on rutile $TiO_2(110)$ surface[12], a gap state is observed at 2.4 eV binding energy, i.e. slightly more than 1 eV above the valence band edge. This finding clearly proves that the electronic structure of the hybrid system corresponds to a II-Type interface, characterized by the presence of molecular states in the gap. This state efficiently reduce the optical gap and allow for an ultrafast dye-to-substrate electron injection.

It is important to note that, according to DFT calculation, only the fully dissociated bidentate bonded (D2) catechol gives rise to gap states, while neither partially dissociated (only one H split off, D1) nor molecularly adsorbed (D0) catechol has its HOMO within the band gap region on rutile (110)[12]. Diebold et al. have also investigated the electronic properties of catechol adsorbed on anatase $TiO_2(101)$. The alignment between molecular states and semiconductor band was studied as a function of coverage, by means of UPS and XPS measurements. UPS measurements (see Figure 3.3.7 (a)) showed that new states within the semiconductor band gap are introduced upon catechol adsorption. The HOMO state is located about 1 eV above the valence band edge, a value slightly lower than that observed for catechol on rutile $TiO_2(110)$[8]. Most interestingly, as shown in Figure 3.3.7 (b), this gap state appears at a certain dosage, while it is absent for the lowest coverages. Catechol adsorbed at surface steps and at isolated point defect sites therefore does not introduce a state in the band gap. The authors correlate the formation of the band

gap states with the formation of catechol self-organized islands at terraces. These results clearly indicates that, at least in the case of TiO_2 surfaces, the interface electronic structure is strongly correlated with both the adsorption geometry and the degree of dissociation of the molecules. This correlation can play a significant role in photocatalysis and DSSCs.

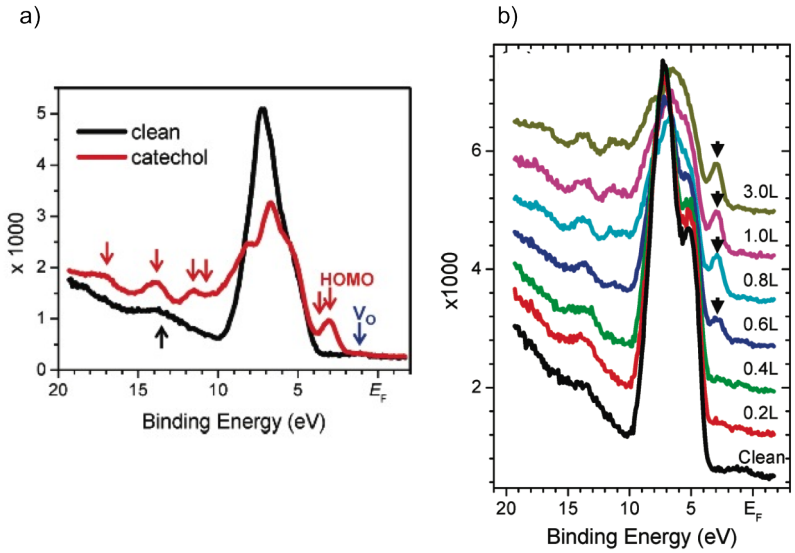

Figure 3.3.7: a) UPS spectra of clean anatase $TiO_2(101)$ (black) and with a saturation coverage of catechol (red). b) UPS spectra after catechol incremental dosages as indicated. Arrows mark the HOMO (band gap state). [8]

3.3.4 How catechol adsorbs on ZnO surfaces

The catechol/ZnO interface is less investigated relative to its TiO_2-based counterpart. Adsorption of different catecholate moieties on the $ZnO(10\bar{1}0)$ surface has been theoretically investigated by Calzolari and co-workers. Catechol adsorbs on the surface forming two Zn-O chemical bonds through the hydroxyl terminations of the molecule, in a similar fashion as the case of TiO_2 surfaces. Calzolari et al.[13] follows the adsorption reaction during the relaxation path, showing that the molecule spontaneously deprotonates, releasing a H^+ ion from one hydroxyl group. The H proton is captured by the oxygen atom of the next neighbor dimer (Figure 3.3.8 (a)). The other OH termination rotates and points toward the frontal oxygen atom of the lateral dimer. The final position of the OH groups leads

to formation of two parallel H bonds with the surface. The two Zn-O bond lengths are very similar (2.1 and 2.0 Å), with the deprotonated catechol oxygen slightly closer to the Zn atom. The surface does not exhibit structural distortions, except for the adsorption sites, where the substrate de-relaxes, removing only the buckling of the dimers involved in the bonding process. Formation of two covalent and two hydrogen bonds per molecule strongly stabilizes the structure. As shown in Figure 3.3.8, the molecular orientation is almost perpendicular to the surface.

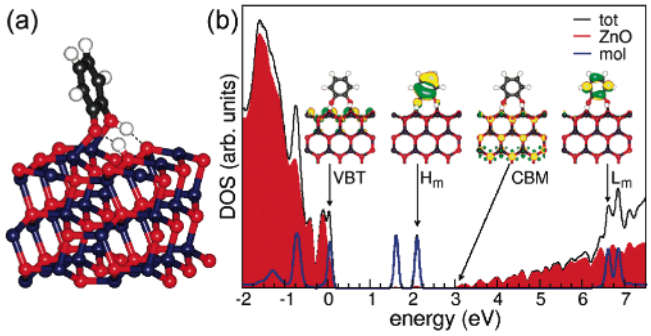

Figure 3.3.8: (a) Side view of the atomic structure of catechol adsorbed on ZnO(1010). (b) Total DOS (black line) and projected contributions on ZnO substrate (shaded area) and catechol (blue line) for the molecule/ surface interface. Inner panels show representative single-particle states[13].

3.3.5 Electronic properties of catechol/ZnO interfaces

Experimentally, Rangan et al. investigated the electronic properties of catechol adsorbed on the ZnO(11$\bar{2}$0) surface, i.e. the other ZnO non-polar surface, by means of UPS and inverse photoemission spectroscopy (IPS).

This investigation provides information on the molecular level alignment relative to the semiconductor bands. The HOMO state is found to lie within the gap, at 2.5 eV binding energy, i.e. roughly 0.5 eV from the valence band edge. The energy difference between this occupied state and the 2.8 eV feature observed in the IPS unoccupied states and attributed to the molecular LUMO, yield a π–π^* gap value of 5.3 eV. This number is comparable to the HOMO - LUMO gap of free catechol and gives an estimate of the energy needed for direct intramolecular optical excitation. As expected for this molecule,

this energy is much higher than the semiconductor band gap (3.4 eV). On the other hand, the effective gap for direct injection, i.e. the HOMO−CB distance, is estimated as roughly 2.8 eV, much smaller than the band gap of the substrates. We should here note that this value represents a rough estimate, as it is affected by the non trivial relative alignment between UPS and IPS data.

The level alignment between catechol derivatives and ZnO($10\bar{1}0$) surface has been theoretically investigated by Calzolari et al.[13] for different catecholate moieties. As a first approximation, the molecular energy alignment with respect to the semiconductor bands has been considered as dictated by the relative values of the molecular and semiconductor ionization potentials. To investigate this aspect the authors considered a set of molecules with different lateral attached groups, and analyzed the alignment of the HOMO and LUMO states within the ZnO band gap (see Figure 3.3.9). They showed that it indeed varies according to ionization potential values, and suggested that appropriate chemical functionalization could be used for tailoring the interface electronic properties. Among several different catecholate moieties, this work considered 4-nitrocatechol and aminocatechol (4-amino-1,2-benzendiol) molecules, i.e. catechol molecule functionalized with a strong electron acceptor, NO_2, or a strong electron donor, NH_2, respectively. The nitro functional group polarizes the molecule, reducing the electron accumulation in the OH anchor group and thus the lone pair repulsion. This results in a downward shift of the molecular HOMO energy position, relative to that of the catecholate interface. On the other hand, the aminocatechol HOMO is found to lie above the CB_{min} of the ZnO, possibly acting as an effective n-dopant for the system. We must note that these prediction are based on simple alignment of the isolated molecular levels with the semiconductor bands. In few selected cases, the full theoretical calculation at the molecule/ZnO interface has been performed. In the case of 4-nitrocatechol/ZnO for instance, the single molecule results are partially recovered, though energy differences between catechol and 4-nitrocatechol alignment resulted definitely smaller in the complete calculation than in the simple single-molecule based case.

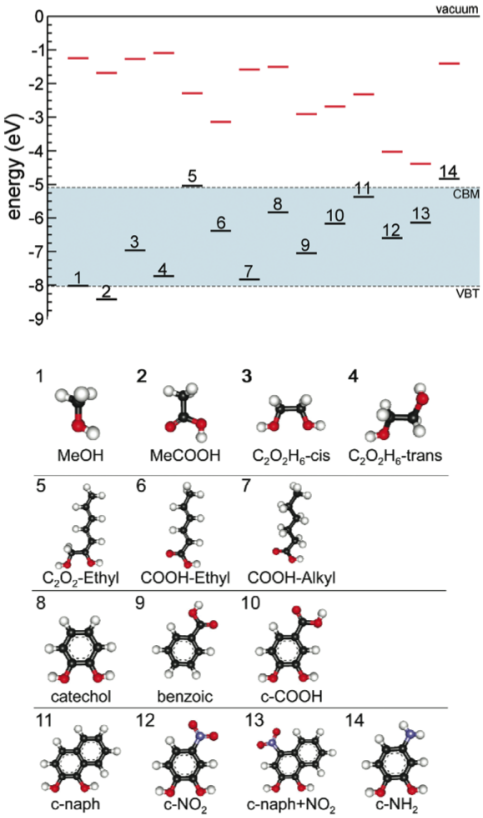

Figure 3.3.9: In the top panel are represented the HOMO (black) and LUMO (red) energy position for the different molecules in the gas phase, with respect to the vacuum level. Shaded area identifies the band gap of clean ZnO(1010) surface. Labels refer to the molecule in the bottom panel[13].

3.4 Phthalocyanine/metal-oxide interfaces

While the adsorption of phthalocyanines on metal surfaces has been very extensively investigated in the last decades, adsorption on metal oxide semiconductor surfaces has been only relatively recently addressed.

3.4.1 Metal-Phthalocyanines on TiO_2 surfaces

The adsorption of Cu-phthalocyanine (CuPc) on the $TiO_2(011)$ surface has been investigated by Godwelsky et al.[14] by means of STM, for coverages going from single molecule adsorption up to 2 ML , in a broad range of annealing temperature, from room temperature to desorption. For low coverage, surface defects, such as vacancies and hydroxyls, act as anchoring points favoring molecular adsorption. In particular, molecules are found at terrace edges. The observed STM image of this single molecules is consistent with the shape of the LUMO of the molecule, indicating a rather weak interaction (physisorption, or "soft" chemisorption) with the substrate and only slight distortions of the electronic structure. Upon increasing coverage, molecules are found to adsorb on terraces in different configurations. A significant fraction of them are found to interact with the substrate, presumably through N-Ti bonding. On the other hand, hydrogen bond formation between a hydrogen atom from the molecule and a surface oxygen is rather unlikely, due to the small polarization of the molecular aromatic hydrogens. Upon further coverage increase a second layer is formed, in which molecules lie flat on the surface. Interestingly upon annealing at 200 ^{o} C, the molecules in the second layer are somewhat unexpectedly found to re-orienter themselves from the flat-lying to an up-right geometry.

Zn-phthalocyanine (ZnPc) is characterized by fully-filled Zn d-orbital, deeply hidden below the organic ligand frontier orbitals, and its behavior should be therefore to a first approximation comparable to that of CuPc. The adsorption mechanism and electronic properties of ZnPc during initial stages of growth on TiO_2 has been investigated by Yu et al[15] by means of XPS, UPS and NEXAFS measurements. According to NEXAFS results, the molecules bind to the surface with the molecular plane roughly 30° from the

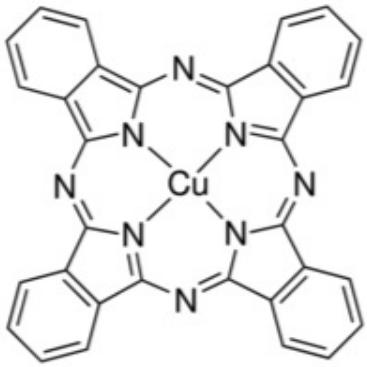

Figure 3.4.1: Structure of Cu-phthalocyanine molecule

surface plane.

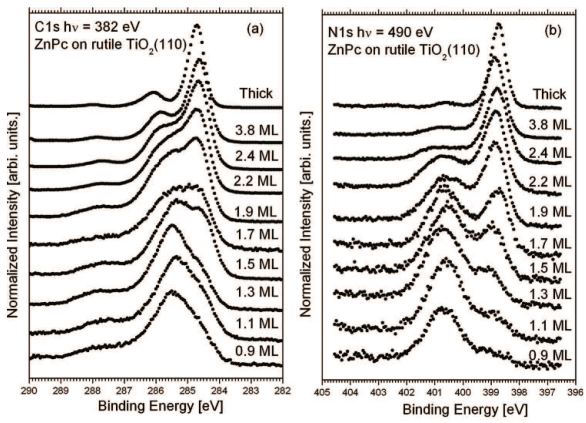

Figure 3.4.2: Core level spectra of C1s (a) and N1s (b) from ZnPc on TiO_2[15].

The evolution of the C1s and N1s core level spectra has been followed as a function of coverage: as shown in Figure 3.4.2 for both core levels, the submonolayer spectra present a component at high binding energies, while with increasing coverage the spectra shift to lower binding energies. The energy difference between the submonolayer spectra and the thick film ones is of 1.7 eV for the N1s core-level. In the case of C1s a modification of the line-shape is also observes, as the component attributed to pyrrole carbon shifts by 1.5 eV, while for that attribute to benzene the energy shift is smaller (0.8 eV). The observed shifts are attributed to a charge transfer from the molecule towards the surface. The differences in the energy shifts of the atoms located in the inner part of the molecule

(i.e. nitrogens and pyrrole carbons), and the benzene carbons, located at the outer part, were assumed to reflect differences in the electronic environment of the inner and outer parts of the molecule[15].

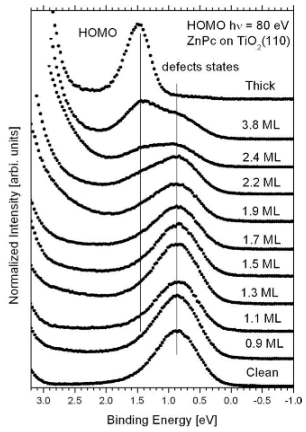

Figure 3.4.3: VB spectra: HOMO region at different coverages of ZnPc on TiO_2[15].

A similar behavior was also reported by Palmgren et al. for Fe-phthalocyanine (FePc) adsorbed on rutile TiO_2[16]. UPS measurements as a function of coverage have been also reported (see Figure 3.4.4). At low coverage the spectra does not display any HOMO structure. As the coverage increases, the HOMO gradually emerges at 1.4 eV, aligned with the HOMO of the thick film. A similar behavior was also observed for ZnPc[15] and was attributed to a depletion of the HOMO electron density for interfacial molecules. This explanation nicely fits with the absence of the shake-up structure of the C1s core level peak (derived by HOMO-LUMO transitions) at low coverage. The HOMO of ZnPc is mainly derived by contributions from pyrrole carbons and is therefore mainly localized in the inner part of the molecule. Its low-coverage absence is therefore in agreement with the indication of core-level shifts, which showed a stronger charge transfer toward the surface for nitrogen and pyrrole atoms relative to the benzene ones.

3.4.2 Metal-Phthalocyanines on ZnO surfaces

As far as we know, no structural study of the CuPc/ZnO($10\bar{1}0$) interface has been reported in literature. We therefore refer to works on the similar ZnPc/ZnO($10\bar{1}0$) system.

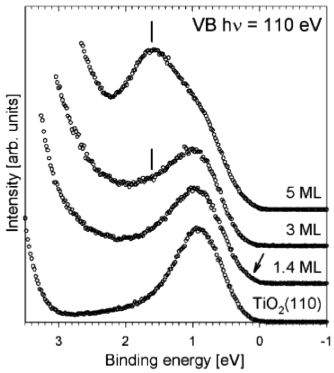

Figure 3.4.4: VB spectra of the FePc/TiO_2. Vertical bars indicate the HOMO position in the thick film case. The arrow indicates a possible state related to the HOMO in the first-layer FePc molecules[16].

Adsorption of ZnPc on the ZnO($10\bar{1}0$) surface has been theoretically extensively investigated by Mattioli and co-workers[17]. At sub-monolayer and monolayer coverage ZnPc molecules tend to form planar aggregations in the form of dimers and J-stripes. The molecule binds to the surface by a combination of two joined interactions: on one hand the formation of a chemical bond involving the molecular Zn and one of the surface O atoms, on the other a "face-to-face" interaction involving the broad molecular macrocyclic system and the rather flat ZnO surface, primarily due to van der Waals forces.

The "face-to-face" interaction has been found to induce a high polarization of electronic charge at the molecule-surface interface. More specifically, a fraction of the ZnPc charge density is shared with the ZnO surface in agreement with the donor tendency of the molecule and the acceptor tendency of the surface. On the experimental side, only few studies have investigate metal-phthalocyanine adsorption on ZnO surfaces by means of electronic spectroscopies. Komolov at al.[18] investigated the interaction of CuPc with the ZnO($000\bar{1}$) surface by means of Auger electron spectroscopy (AES), showing strong interaction between the molecule and the surface, leading to partial molecular decomposition at low coverages. This result is somewhat questionable, as it is well known that the AES high energy electron beam itself could induce molecular decomposition.

3.4.2.1 Electronic properties: work function change and molecular level alignment

In a recent work Park and co-workers[19] investigated the deposition of CuPc on ZnO(0001) thin film by means of XPS and UPS, for different ZnO film conditions and for overlayer thickness ranging between 0.2 nm and 20 nm (i.e. roughly between half a monolayer up to 50 ML). In Figure 3.4.5 the UPS spectra of the CuPc film grown on the clean ZnO film are reported. An interface dipole (i.e. variation of the ionization potential) of 0.2 eV was observed while no substrate band bending occurred. The variation in ionization potential is attributed to charge transfer from the molecule to the substrate. On the other hand a band bending of 0.3 eV is reported to occur within the molecular film, for coverages above 2.0 nm. The energy offset between the CB_{max} of ZnO and the HOMO of CuPc was 1.0 eV for the cleaned ZnO interface.

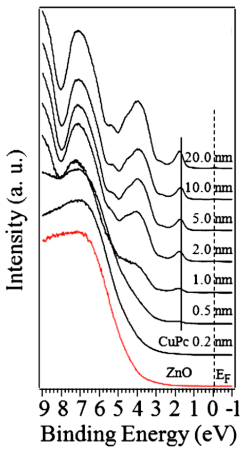

Figure 3.4.5: Valance band region of UPS spectra for CuPc deposited on ZnO film[19].

The issue of ionization potential changes induced by metal-phthalocyanines adsorption on different substrates have been quite intensively investigated in the case of metal and graphite surfaces. Fukagawa et al.[20, 21] investigated by means of UPS, the changes in the W_F of phthalocyanine/graphite systems as functions of coverage. Few phthalocyanine moieties were considered, which differ for the value of their molecular dipole moment. In the case of TiO-phthalocyanine (OTiPc)[21], which is characterized by a significant

permanent dipole moment perpendicular to the surface, the work function increases as a function of coverage, reaching a maximum for one monolayer (ΔW_F= - 0.3 eV). This indicates that the molecule is oriented with the Ti-O group pointing outside the surface. For increasing coverage, the W_F decreases back to the clean surface value. This behavior is rationalized assuming that the second molecular layer adsorbs on the surface with the dipole moment oriented in the opposite direction relative to the first one, so that the total dipole moment at the interface tends to vanish. The results show that the dipole-dipole repulsive interaction impacts the growth and structure of these systems, which are characterized by weak intermolecular and molecule-substrate electronic coupling. On the other hand in the case of CuPc[20], the molecule, which has a planar geometry, does not present any permanent dipole moment. Accordingly, an almost negligible W_F change is observed in this case (less than 0.1 eV). As we shall see, this is at variance with our results on W_F change upon adsorption in the case of CuPc on the ZnO surface.

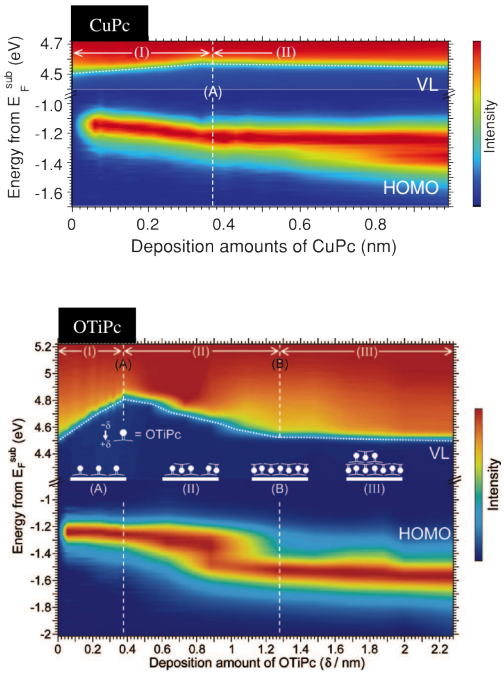

Figure 3.4.6: Map of He I UPS spectral intensities for VL and HOMO band regions of the CuPc-HOPG[20] and OTiPc/HOPG[21] systems as a function of deposition amount (δ). The vertical axis represents the electron energy relative to E_F^{sub}. VL corresponds to the cutoff of the secondary electron (indicated by the white dotted line). Top: (I)–(II) indicate regions of monolayer and double-layer formation, and (A) corresponds to δ of the monolayer being formed. Bottom: (I)–(III) indicate the regions of the monolayer and double layer formation, and (A) or (B) corresponds to δ of the monolayer and double layer being formed.

Bibliography

[1] R. Jose, V. Thavasi, S. Ramakrishna J. Am. Ceram. Soc. 2009, 92, 289.

[2] C. Woll Prog. Surf. Sci. 2007, 82, 55.

[3] I. A. Jankovic, Z. V. Saponjic, M. I. Comor, J. M. Nedeljkovic J. Phys. Chem. C 2009, 113, 12645.

[4] W. R. Duncan, O. V. Prezhdo J. Phys. Chem. B 2005, 109, 365.

[5] P. Kamat, R. Huehn, R. Nicolaescu, J. Phys. Chem. B 2002 106, 788.

[6] G. Ramakrishna, H. N. Ghosh, Langmuir 2003, 19, 3006.

[7] S. Rangan, J.-P. Theisen, E. Bersch, R. Bartynski, Appl. Surf. Sci. 2010, 256, 4829.

[8] S.-C. Li, Y. Losovyj, U. Diebold Langmuir 2011, 27, 8600.

[9] S.-C. Li, L. N. Chu, X.-Q. Gong, U. Diebold, Science 2010, 328, 882.

[10] K. L. Syres, A. G. Thomas, W. R. Flavell, B. F. Spencer, F. Bondino, M. Malvestuto, A. Preobrajenski, M. Gratzel J. Phys. Chem. C 2012, 116, 23515.

[11] L.-M. Liu, S.-C. Li, H. Cheng, U. Diebold, A. Selloni J. Am. Chem. Soc. 2011, 133, 7816.

[12] S.-C. Li, J.-G.Wang, P. Jacobson, X.-Q. Gong, A. Selloni, U. Diebold, J. Am. Chem. Soc. 2009, 131, 980.

[13] A. Calzolari, A. Ruini, A. Catellani J. Am. Chem. Soc. 2011, 133, 5893.

[14] S. Godlewski, A. Tekiel, J. S. Prauzner-Bechcicki, J. Budzioch, A. Gourdon, M. Szymonski J. Chem. Phys. 134, 224701 (2011).

[15] S. Yu, S. Ahmadi, C. Sun, P. T. Z. Adibi, W. Chow, A. Pietzsch, M. Gï¿œthelid J. Chem. Phys. 136, 154703 (2012).

[16] P. Palmgren , K. Nilson , S. Yu , F. Hennies , T. Angot , C. I. Nlebedim, J.-M. Layet , G. Le Lay , M. Göthelid J. Phys. Chem. C, 2008, 112, 5972.

[17] G. Mattioli, C. Melis, G. Malloci, F. Filippone, P. Alippi, P. Giannozzi, A. Mattoni, A. A. Bonapasta J. Phys. Chem. C 2012, 116, 15439.

[18] A. S. Komolov, P. J. Moller, J. Mortensen, S. A. Komolov, E. F. Lazneva Surf. Sci. 2005, 586, 129.

[19] S. H. Park, H. J. Kim, M-H Cho, Y. Yi, S. W. Cho, J. Yang, H. Kim Appl. Phys. Lett. 2011, 98, 082111.

[20] H. Fukagawa, S. Hosoumi, H. Yamane, S. Kera, N. Ueno Phys. Rev. B 2011, 83, 085304.

[21] H. Fukagawa, H. Yamane, S. Kera, K. K. Okudaira, N. Ueno Phys. Rev. 2006, 73, 041302.

Chapter 4

Experimental techniques

4.1 Photoelectron spectroscopy (PES)

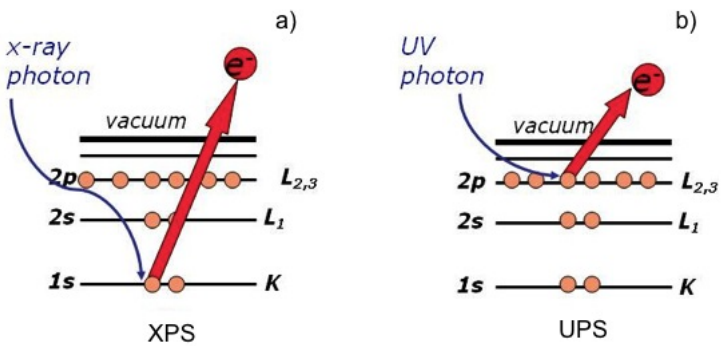

Figure 4.1.1: Panel a): scheme of X-ray photoemission of a core electron. Panel b) scheme of a UV photoemission of a valence electron.

The most important and widely used experimental technique to gain information about occupied electronic states is photoemission spectroscopy. The essential parts of the experimental set-up are a monochromatic light source, the sample contained in an UHV vessel, and an electron energy analyser with detector. The experiment is based on the photoelectric effect. The solid surface is irradiated by mono-energetic photons with energy hν, and the emitted electrons are analyzed with respect to their kinetic energy E_{kS}. A photoelectron spectrum gives therefore the number of detected electrons per energy interval

(intensity) as a function of their kinetic energy. We talk about UV photoelectron spectroscopy (UPS) when we use photons in the ultraviolet spectral range. Otherwise, when X- rays are used for excitation, the technique is called X-ray photoelectron spectroscopy (XPS).

The kinetic energy E_{kS} of the photoemitted electron, as measured by the analyser, is given by:

$$E_{kS} = h\nu - E_b - W_F \tag{4.1.1}$$

where E_b is the binding energy (relative to the Fermi level) of the the electron in the sample, and W_F is the work function of the analyser.

A rigorous theoretical approach to the photoemission process requires a full quantum-mechanical treatment of the complete coherent process in which an electron is removed from an occupied state within the solid and deposited at the detector. A much simpler and instructive approach is the so-called three-step model, in which the photoemission process is artificially separated into three independent parts :

- (i) The first step of this process is the optical excitation of an electron from an initial into a final electron state within the crystal. The cross section for this process depends on the energy, polarization and momentum of the photon, as well as to the energy and orbital character (s, p, etc.) of the initial electron state.
- (ii) In the next step, the electron travels through the surface, to the vacuum/surface interface. A large number of electrons undergo inelastic scattering processes; they lose part of their energy by electron-plasmon or electron-phonon scattering. Such electrons contribute to the continuous background in the photoemission spectrum as they have lost the information about their initial energy.

The probability that an electron will reach the surface without inelastic scattering is given phenomenologically by the mean-free path λ. In general and as a first approximation, λ depends on the energy E of the photoelectron and on the composition and density of the

sample. The value of λ is typically between 5 and 20 Å , thus limiting the information depth to this spatial region. It is this second step of propagation to the surface which makes photoemission a surface sensitive technique.

- (iii) Eventually, in the third step, the electron crosses the surface and is emitted from the solid into the vacuum, where it is collected and analyzed. In doing so, the photoelectron has to overcome the surface barrier related to the sample work function.

4.1.1 X-ray Photoelectron spectroscopy (XPS)

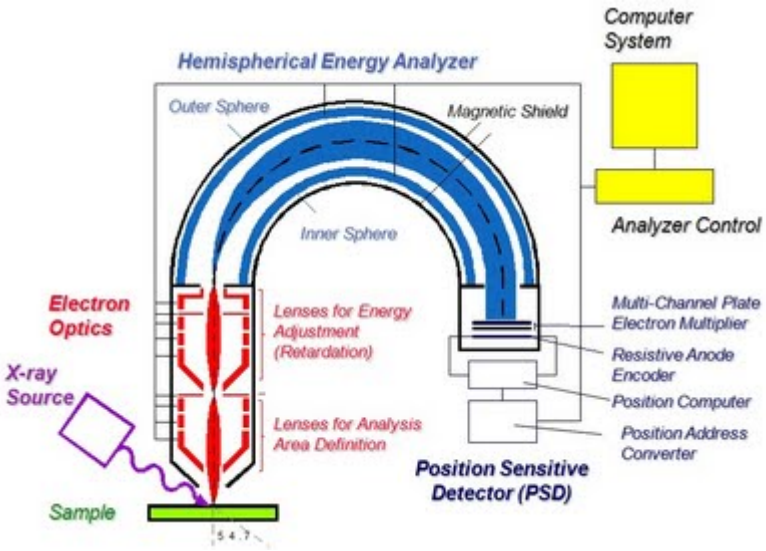

Figure 4.1.2: Representation of an XPS apparatus

X-ray photoelectron spectroscopy (XPS) is a type of photoelectron spectroscopy in which monoenergetic X-rays are used as probe. This technique probes the core-levels excitations and is therefore extensively used to obtain both elemental and chemical information about the near-surface portion (i.e. within few tens of Å) of the sample. It is therefore particularly well suited to study thin film composition and molecular adsorption.

Aluminum (Al) and Magnesium (Mg) are two most frequently used X-ray emitting targets: their energies (1486.6 eV for AlK_α and 1253.6 eV for MgK_α) allow to excite the core level electrons, and their relatively narrow line widths (0.85 eV for AlK_α and 0.7 eV

for MgK_α) allow for fair energy resolution even without the use of a monochromator. The energies of photoelectrons are analyzed using a concentric hemispherical analyzer (CHA).

XPS spectral lines are identified by the shell (core level) from which the electron is ejected. While the kinetic energy of the emitted electrons varies with the energy of the incoming X-rays, the binding energy stays unchanged for electrons from a certain element in a certain chemical state. Therefore, in an XPS spectrum the intensities of the emitted electrons are usually plotted versus their binding energies.

Each element has a unique set of binding energies, so XPS can be used to identify and determine the concentration of the elements within the surface region.

The core level retains atomic nature. Variations in the binding energies for a certain core level arise from different effects. These effects can be divided into two groups, namely initial and final state effects.

The initial state effects describe the phenomena independent on the photoemission event. Core binding energies are determined by electrostatic interaction between the core level and the nucleus. It changes with the electrostatic shield of the nuclear charge coming from all other electrons in the atom, including valence electrons. Removing or adding an electronic charge as result of changes in bonding therefore affect the core-level binding energy.

Indeed, the total charge that an electron experiences depends also on the neighbouring atoms, both intermolecular and intramolecular. Therefore in compounds, where ionic or covalent bonding occurs, the photoelectron core-level peak position may shift relative to that of the single elemental samples. We define the core-level chemical shift as the change in binding energy of a core electron of an element due to a change in the chemical bonding of that element. Atoms of a higher positive oxidation state exhibit a higher binding energy due to the extra coulombic interaction between the photo-emitted electron and the ion core. An example: the bonding energy of Si2p core level in pure Si is 99 eV, while for Si in SiO_2 it lies at 102.3 eV.

Final state effects on the other hand, are related to the photoemission process itself: when an electron is ejected it creates an excited state, which must relax to a new, low

energy state. The energy involved in this process, called relaxation energy, will affect the final state of the electron during the photoionization process. As a rule of thumb, we can say that the higher the electron density in the neighnorhood of the core hole, the more efficient is its screening. In turns this corresponds to higher kinetic energies (i.e. lower binding energies) of the photoelectron.

4.1.1.1 Quantitative analysis for XPS

The photoelectron intensity of core levels can be employed as a way to determine the concentration of an element in a sample.

However, the absolute intensity from the experiment cannot be directly compared for different elements or for different core levels of the same element.

Given an homogenous sample of thickness s, the intensity of a core level depends on several parameters and can be expressed as:

$$I = Kn\sigma\Theta d(\lambda(E))T \tag{4.1.2}$$

where n is the atomic density, K is a proportionality constant which depends on the experimental set-up (i.e. photon flux, illuminated area, etc.) , T is the photoelectron transmittivity (which depends on the photoelectron kinetic energy), and σ is the cross section for the optical excitation process, which depends on the transition itself, while Θ is its angular factor, related to the angle between the photon and the photoelectron trajectories. The product

$$\sigma\Theta T = S \tag{4.1.3}$$

is defined as Atomic Sensitivity Factor (ASF), and can be found tabulated for typical experimental conditions[1]

The term d(λ(E)) accounts for the effective thickness of the sample, i.e. the equivalent thickness of the material from which the measured photoemission signal would come if

there were no inelastic attenuation. It can be written as:

$$d \equiv \lambda(1 - e^{-s/\lambda}) \tag{4.1.4}$$

where s is the actual layer thickness and λ is the photoelectron inelastic mean free path (or IMFP). We recall that IMFP is defined as the average distance that an electron with a given energy travels between two successive inelastic collisions. Denser elements/compounds will have smaller IMFPs as will core electrons with greater binding energies (i.e. smaller kinetic energies).

Summarising, we can say that the intensity (i.e. the area) of a core-level peak is proportional to the atomic density of the related species; the proportionality constant depends on the element ASF and, as we shall see later in more details, on the spatial distribution of the element within the sample.

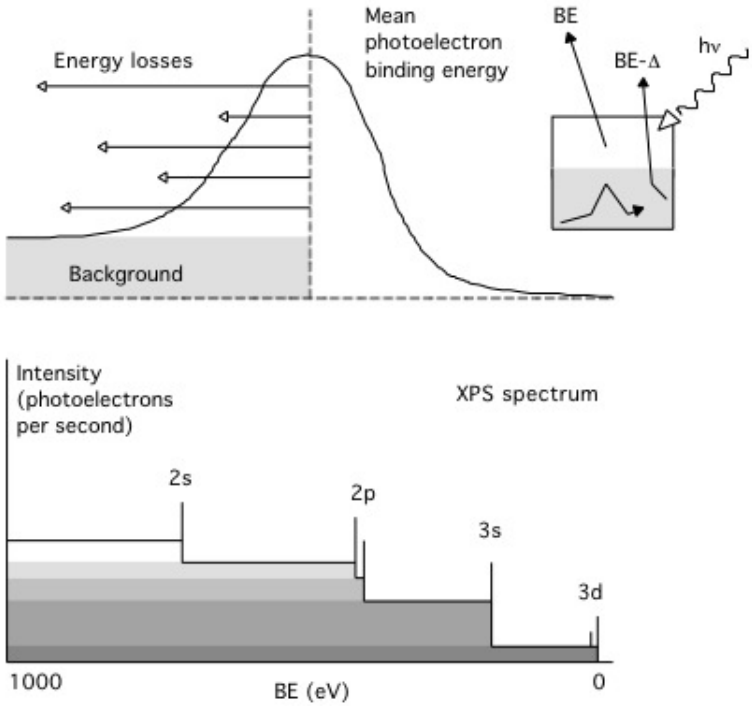

Figure 4.1.3: Top of the panel: a typical core level peak with an asymmetrical shape due to the presence of the background. Bottom of the panel: a drawing of a typical stepped background.

For quantitative analysis of the XP spectra, we need a proper evaluation of the area belonging to each core-level.

It is first of all therefore necessary to apply an appropriate background correction to the core-level spectra. As shown in figure (4.1.3), XPS spectra show a characteristic "stepped" background: its intensity in the high binding energy part of the photoemission peak is always greater than that in the low binding energy part. This shape is related to the inelastic processes suffered by secondary electrons: the smaller the kinetic energy, the larger is the number of secondary electrons.

Moreover, it is also necessary to describe the photoemission lines by model functions, since the intensities of overlapping contributions can only be determined by fitting the XP spectra with such functions. In simple cases, the width of a line contains the experimental broadening of the spectrum together with the natural line width. The former includes the line width of the photons and the resolution of the electron energy analyzer, and is usually described by a Gaussian function. The natural line width results from the lifetime of the excited state and leads to a line shape which can be described by a Lorentzian function. The core-level lineshape is therefore given by the convolution of the experimental Gaussian with the Lorentzian shape, giving a Voigt function.

In Figure 4.1.4 on page 64 are outlined the main steps for the quantitative analysis procedure used in this thesis. We are analyzing a system composed by a very thin organic layer adsorbed on a ZnO single crystal.

Step 1 - Background subtraction

To perform a fitting procedure on a core level spectrum it is necessary to remove its background. We chose a non-linear method for background subtraction, the so- called Shirley method [2]. The background intensity, at any given binding energy, is proportional to the intensity of the total peak area above the background in the lower binding energy peak range. Namely the background goes up in proportion to the total number of secondary photoelectrons below its binding energy position. The Shirley background can be defined

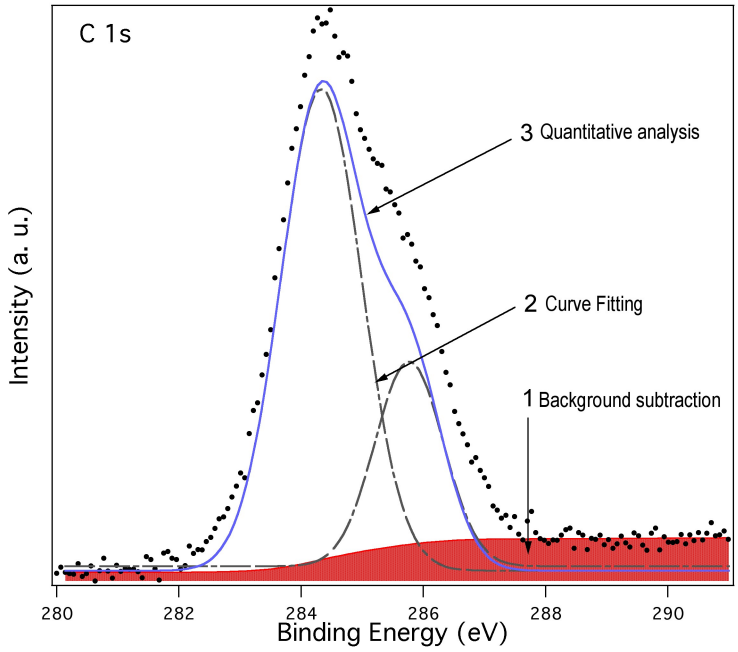

Figure 4.1.4: A C1s core level peak. In this cartoon the main steps for a quantitative analysis of an XPS core level peak are outlined.

by the following equation:

$$S(E) = N \int_{E}^{+\infty} I(E)dE \tag{4.1.5}$$

where I(E) is the measured spectrum at energy E and N is the normalization factor. In Figure 4.1.4 on page 64 an example of the Shirley background calculated on a C1s core level peak for catechol molecules on ZnO surface is shown.

Step 2 - Curve fitting

This procedure consists in fitting each core level line shape with a Voigt function.

$$f(x) = a0 + a1 \times V(\frac{\sqrt{ln2}}{w_g} \times (x - e), \frac{w_l}{\sqrt{ln2}/w_g}) \tag{4.1.6}$$

where the intensity of the peak is expressed by the coefficient *a1* and the binding

energy by the coefficient e. w_g is the coefficient which takes into account the width of the peaks related to the instrumental resolution. w_l is the coefficient which provides the Lorentzian weight.

As shown in Figure 4.1.4 on page 64, the fitting function for molecular core-level spectra presenting different components is given by the sum of different Voigt lineshape ((4.1.6)), one for each chemically-shifted component.

Step 3 - Quantitative analysis

The quantitative evaluation of the sample chemical and elemental composition starts from Eq. 4.1.2. If we are simply interested in finding the stoichiometric ratio between two elements present on the sample surface (like for instance two elements belonging to the same adsorbed molecule, in the low-coverage regime), we can consider the following relation:

$$\frac{n_1}{n_2} = \frac{I_1/S_1}{I_2/S_2} \tag{4.1.7}$$

where $\frac{n_1}{n_2}$ is the stoichiometric ratio between two elements present on the surface.

If we now consider a thin adlayer formed by the species (1) adsorbed on a bulk (species (2)), we get

$$I_1/I_2 = \frac{n_1 S_1 s_1}{n_2 S_2 \lambda_2} \tag{4.1.8}$$

where the effective thickness of the bulk sample becomes (as the sample thickness is is $s \gg \lambda$) $d = \lambda_2$, where λ_2 is the IMPF of photoelectron (2) in the bulk, and and the effective thickness of the adlayer coincides with its actual thickness s_1. From this equation, in the case of a single monolayer, it is possible to obtain the surface density of the adlayer species (1).

4.1.2 UV photoelectron spectroscopy (UPS)

UV-photoelectron spectroscopy (UPS), due to the relatively low energy of the UV radiation (He I 21.22 eV and He II 40.81 eV), is applied to investigate the valence electronic

structure of materials (see panel b) in Figure 4.1.1 on page 57). Since the valence orbitals are responsible for the formation of chemical bonds, UV-photoelectron spectroscopy is particularly suitable for the study of electronic structure of adsorbed molecules at surfaces. Therefore we can identify the adsorbed compounds by their "fingerprints", as well as obtain information regarding the type of adsorption (chemi-/physisorption) and the orbitals involved in the bond. For an unambiguous assignment of UPS signals, it is often necessary to take quantum chemical calculations. Unlike XPS, UPS is not a quantitative method, because the cross sections, at low photon energies for different energy levels, widely vary. Furthermore, the low kinetic energies lead to diffraction effects of the electrons. UPS here is used to study the valence structure of the adsorbate by comparison of the molecular orbitals of the adsorbed species with those of theoretical calculations.

4.1.2.1 Determination of work function

Further information, which can be obtained from UP spectra, includes the work function W_F of the a semiconductor sample.

Figure 4.1.5 on page 67 shows a schematic energy diagram of a n-type semiconductor. Valence bands and conduction bands are separated by the band gap (E_g).

In a semiconductor, the Fermi level is located within the band gap. This means that the work function is different from the ionization energy (energy difference between valence bands maximum (VBM) and vacuum level). In a semiconductor, the Fermi level becomes a somewhat theoretical , statistically defined, construct since there are no allowed electronic states within the band gap. Nevertheless, also in a semiconductor sample the work function can be measured by UP spectroscopy.

For this purpose the energy difference ΔE between the secondary electron cut-off (the minimal kinetic energy of photoelectrons $E_{Akin,min}$) and the energy of the UV light source (the maximum kinetic energy $E_{Akin,max}$) are needed. The work function is given by the difference between the energy of the incident UV light and ΔE, which is the energy difference between secondary electron cut off and the Fermi edge.

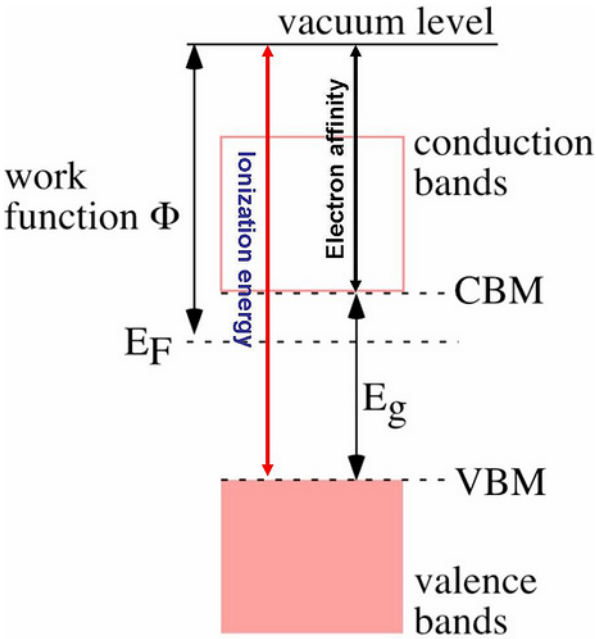

Figure 4.1.5: Schematic energy diagram of a n-type semiconductor.

$$\Delta E = E_{Akin,max} - E_{Akin,min} \tag{4.1.9}$$

Since electrons at the Fermi edge have zero binding energy ($E_b = 0$),

$$\Delta E = E_{Akin,max} - E_{Akin,min} = h\nu - W_F \tag{4.1.10}$$

thus

$$W_F = h\nu - \Delta E \tag{4.1.11}$$

4.2 Low-energy electron diffraction (LEED)

LEED is a technique for the determination of the surface structure of crystalline materials, obtained using a collimated beam of low energy electrons (20 - 300eV) and observing

diffracted electrons as spots on a florescent screen (see Figure 4.2.1 on page 68). The energy range below 300 eV is particularly suited to surface studies since the mean-free path of these slow electrons in the solid is short enough to give good surface sensitivity. Furthermore, according to the de Broglie relation

$$\lambda(\text{Å}) = \sqrt{150.4/E(eV)} \tag{4.2.1}$$

Typical LEED wavelengths are in the Å range, comparable with wavelengths used in X-ray crystallography, and of the same magnitude as the interatomic distances in a solid. The gun used in LEED technique includes an electron source which may be a heated tungsten filament or LaB6 source. Monochromatic electrons are emitted and then are accelerated and focused into a beam. Some of the electrons incident on the sample surface are backscattered elastically, and diffraction can be detected if the surface is well ordered. The diffraction pattern may then be recorded by a camera and displayed on a computer screen.

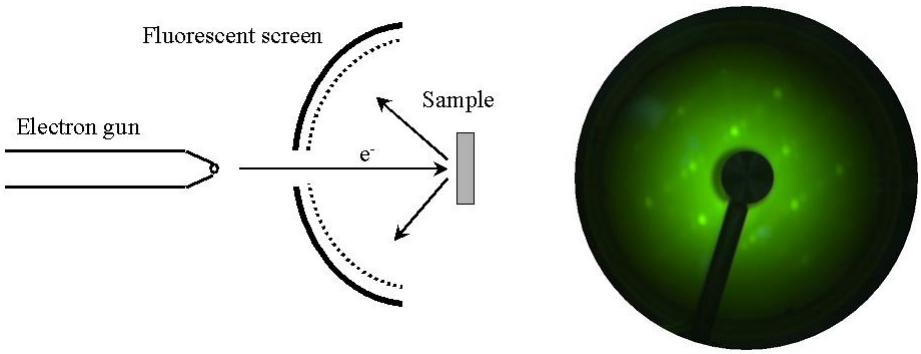

Figure 4.2.1: Scheme of a LEED apparatus and a typical diffraction pattern

LEED is a surface sensitive technique, because the inelastic mean free path of the elastically scattered electrons is only a few angstroms, thus only a few atomic layers are detected by the electron beam, and the contribution of deeper atoms to the diffraction progressively decreases. The LEED pattern is a representation of the symmetry of the surface of the sample. The position of the diffraction spots yields information regarding the long range order of the surface. The intensity of the diffracted spots can, if studied as

a function of surface incident energy, yield information regarding the basis when compared with theoretical data derived from appropriate structural models.

4.3 High resolution electron energy loss spectroscopy (HREELS)

HREELSis a technique that uses an electron beam to probe the properties of solid surfaces, such as phonon vibrations and vibrational modes of adsorbed molecules on the surface, as well as the surface geometry [3].

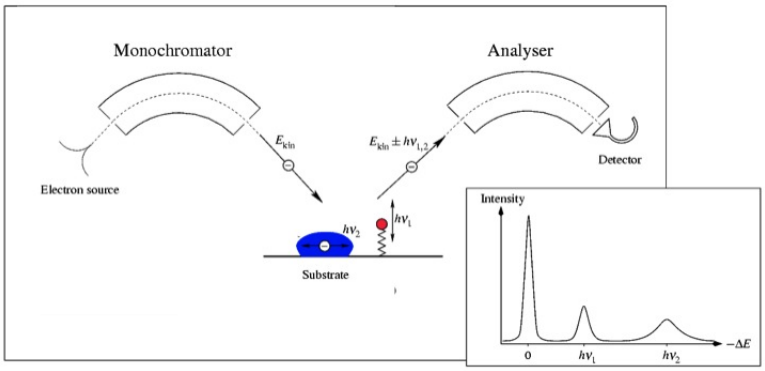

Figure 4.3.1: Schematic drawing of an HREELS experiment

In a typical HREELS experiment, a highly monochromatic beam with a low energy of E_0 impinging on the sample surface may excite quantized excitations within the sample (see Figure 4.3.1 on page 69). The result is the emergence of a scattered electron with energy, E_S, defined by:

$$E_S = E_0 - \hbar\omega_0 \tag{4.3.1}$$

where $\hbar\omega_0$ is the energy of a quantized excitation. An analysis of the energy loss spectrum of these backscattered electrons provides direct information on the chemical bonds existing on the sample surface. An incoming monochromatic electron beam (typically 1

to 10 eV) can be obtained by passing thermally emitted electrons through two 127° cylindrical monochromators arranged in series. The reflected electrons are then collected by an energy analyzer which has the same structure as the 127° cylindrical monochromator.

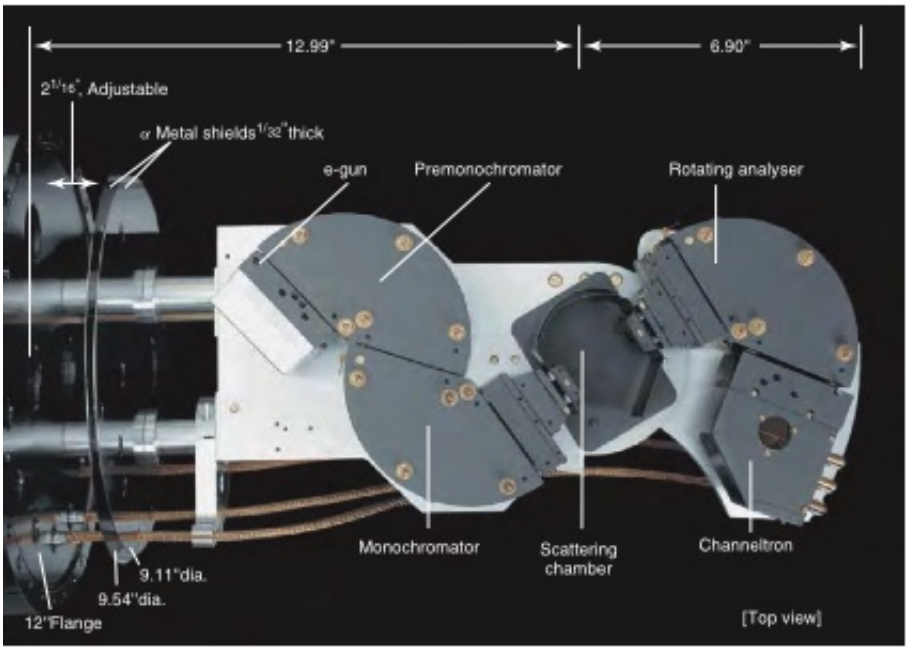

Figure 4.3.2: Photograph of a modern ultrahigh-resolution EEL spectrometer. (Reprinted from http://www.lktech.com/products/els5000.html, courtesy of LK Technologies, Inc)

The mechanisms by which electrons are inelastically scattered are complex due to the strong interactions between electrons and sample. However, such interactions can be split into three limiting cases between which there are no sharp or precisely defined boundaries:

(1) dipole scattering (2) impact scattering (3) intermediate negative ion resonance, or 'resonance', scattering .

In the "dipole scattering" mechanism (1), when the incident electrons interact with the adsorbed molecules, the electric field of the incident electron perturbs the oscillating field of dipole active vibrational modes via long-range coulombic forces at the surface. Therefore, only the vibrations with a dipole change normal to the surface are active. The inelastically scattered electrons appear in a "dipole scattering" within a degree of the specular condition. However, in the "impact scattering" mechanism (2), the incident

electrons are scattered by short range interactions, which are in the order of atomic dimensions. This short-range scattering mechanism involves a much larger momentum transfer and produces a broad angular distribution of inelastically scattered electrons, namely in specular direction and off-specular direction. Therefore, these two dominant mechanisms can be distinguished by moving the detector away from the specular direction. Another special and distinctive example of short-range impact scattering is the "negative ion resonance scattering" mechanism (3)[4]. In this resonance mechanism, the incident electron is trapped into a temporary negative ion state derived from the unoccupied orbitals of the molecule. The negatively charged molecule has a rather short lifetime (10^{-10} to 10^{-15} seconds), and its de-excitation process can lead to a vibrationally excited final state. The scattered electron loses the net excitation energy. The intensity of electrons scattered by this mechanism is strongly enhanced at certain primary electron energy (resonance) and has its distinctive angular distribution related to the symmetry of the molecule and the negative ion. Thus, by varying the orientation of the energy analyzer from the specular mode to the off-specular mode, it is possible to gain information on the direction of the individual vibrational mode.

Probing the surface with a beam of incident energy (E_i) variable of 2-10 eV or more we can study vibrational and electronic loss processes (plasmons). An HREELS spectrum covers a range of 0 - 50 eV of energy loss. In the energy loss region 0 - 500 meV we observe vibrational modes. In this region the interpretation of HREELS spectra follows that of IR spectroscopy. While HREELS are in meV, IR spectra are usually set in wavenumbers (1 meV = 8.065 cm-l). In the region of the spectrum from 0 to 50 eV electronic excitation are observed, giving information on the band gap and on the interband transition.

4.4 Experimental procedures

All measurements were performed in a UHV chamber with a base pressure of $7 \cdot 10^{-10}$ mbar.

XPS and UPS were performed with an unmonochromatized AlK_α source ($h\nu$= 1486.7

eV) and a He discharge-lamp ($h\nu$(He-I_α) = 21.22 eV), respectively. Electron energy distribution curves were measured by a hemispherical analyzer (Omicron EA125) with an overall energy resolution of 1.0 eV (0.1 eV for UPS).

HREELS measurements were performed in specular conditions ($\vartheta_i = \vartheta_0 = 70°$). The spectrometer (LK ELS5000) ensured an energy resolution better than 4 meV (32 cm^{-1}), as checked on Au(111) samples. On the ZnO surface instead, the energy resolution is limited to 20 meV with a primary energy of E_p=20 eV.

The ZnO $(10\bar{1}0)$ single crystal was cleaned by cycles sputtering - annealing. The sputtering has been carried with 0.5 keV and 10 μA for 15 min while the annealing has been performed reaching a temperature of 1073 K for 5 min.

Sample cleanliness and order were checked by XPS and low energy electron diffraction (LEED). In the initial stages of this work, we checked the dependence of the surface quality on different preparation parameters, such as in particular, annealing temperature (till 1173 K), O_2 pressure and quality of the base-pressure during the annealing process. We concluded that oxygen pressure and high temperature do not affect significantly the quality of the surface; rather the most critical parameter results the chamber base-pressure during the annealing. Accordingly the samples were prepared in the pre-chamber with a base pressure of $7 \cdot 10^{-10}$ mbar.

4.4.1 Dye deposition

1,2-Dihydroxybenzene (catechol) (99%, Sigma−Aldrich) was kept in a vial and purified through several pumping-thaw-freezing cycles. The vial is connected to the preparation chamber through a leak valve: 1,2-Dihydroxybenzene deposition on the clean ZnO surface was performed in UHV, opening the leak valve and reaching a pressure of few 10^{-8} mbar. Due to its high vapour pressure, the molecule sublimate at RT and after 1 min of exposure the surface was covered with 1 monolayer. 4-Nitrocatechol (97%, Sigma−Aldrich) was evaporated in UHV by means of a resistively heated glass vial, mounted on a differentially pumped stage, normally separated from the experimental UHV chamber by a gate valve which was opened only during deposition. The sublimation temperature was controlled

by a thermocouple embedded in the vial and molecular deposition was performed at 343 K. Under these conditions, the pressure in the experimental chamber raised to a few 10^{-8} mbar, while that in the evaporation stage was typically $3{\cdot}10^{-6}$ mbar. Molecular deposition was performed keeping the sample at room temperature, and saturation coverage was obtained after 10 min exposure.

Co-deposition of 4-nitrocatechol and ethanol has been performed evaporating the ethanol through a leak valve and than the 4-nitrocatechol with the crucible just described. The ethanol was dehydrated through 3 cycles of cooling at nitrogen liquid temperature and heating at RT under vacuum.

The CuPc was purchased from Sigma-Aldrich. The dye was placed in an evaporation cell in the preparation chamber and extensively outgassed. The current used to sublimate the molecules was 3.44 A and the deposition rates were monitored with a quartz crystal microbalance, using 1.6 g/cm^3 as the bulk density.

Bibliography

[1] J. F. Moulder, W.F. Stickle, P.E. Sobol, and K.D. Bomben. Handbook of X-Ray Photoelectron Spectroscopy, Phisical Electronic Inc, 2005.

[2] D.A. Shirley. Phys. Rev. B 1972, 5, 4709.

[3] H. Ibach, D. L. Mills, Electron Energy Loss Spectroscopy and Surface Vibrations,Academic Press INC: London, 1982.

[4] R. E. Palmer, P. J. Rous, Rev. Mod. Phys. 1992, 64, 383.

Chapter 5

Results and discussion

In this chapter we will describe and analyze the results of our investigation on model dye/ZnO($10\bar{1}0$) interfaces. Our main interest regards modification of the interface electronic properties occurring when a dye adsorbs on the ZnO($10\bar{1}0$) surface. In the first part of the chapter we will describe the adsorption of catecholate moieties (catechol and 4-nitrocatechol) on the ZnO($10\bar{1}0$) surface, focusing our attention on the energy level alignment between the molecule and the ZnO bands. These molecules are characterized by an intrinsic dipole moment that, as we will demonstrate, in the case of 4-nitrocatechol strongly affects the energy level alignment at the interface. The experimental investigation on this system has been performed in strict collaboration with the theoretical group of A. Calzolari, A. Ruini and A. Catellani (Università di Modena e Reggio Emilia, CNR-Nano and IMEM-CNR) which performed DFT calculations on the structural and electronic properties of the same systems.

Starting from these results we decided to investigate a slightly more complicated system, obtained by evaporation of ethanol on the partially functionalized 4-nitrocatechol/ZnO surface. The obtained interface is characterized by the presence of two molecules with opposite dipole moments. The results of this study are reported in paragraph 5.4.

In paragraph 5.5, we consider the effect of photon irradiation on the 4-nitrocatechol/ZnO interface, aiming to highlight the possible effect of dye degradation on the electronic prop-

erties of the interface.

In paragraph 5.6 we will describe the adsorption of Cu-Phthalocyanine on the ZnO surface, characterizing the electronic properties of this system.

5.1 Characterization of the ZnO(10$\bar{1}$0) surface

The ZnO(10$\bar{1}$0) surface was prepared in UHV by sputtering-annealing cycles, as described in Chapter 5. The structural properties of the clean surface was investigated by means of LEED and STM, while XPS and HREELS was used to check surface cleanliness.

LEED and STM measurements

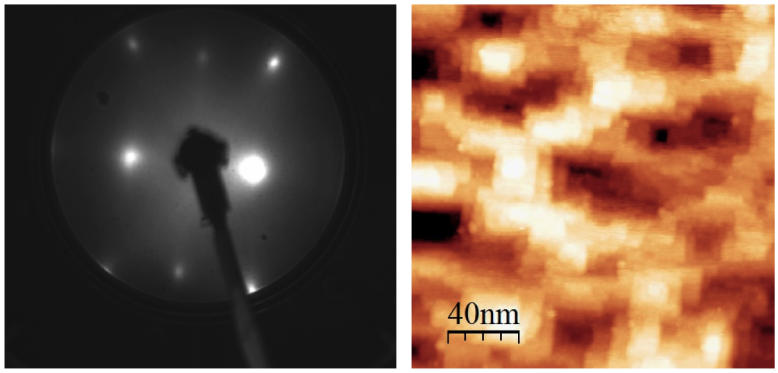

Figure 5.1.1: The right picture shows the LEED pattern of the ZnO(10$\bar{1}$0) taken with 70 eV beam energy. The left picture is an STM image of the ZnO surface, 200x nm, I_{tun}= 0.05 nA, V= 2 V.

Figure 5.1.1 shows a typical LEED pattern of the clean ZnO(10$\bar{1}$0) surface. It corresponds to a (1×1) structure, indicating, as expected, that the surface does not reconstruct. The lateral profile of the spots is quite broad, indicating that the surface is characterized by quite small domains. The surface morphology was investigated by STM, showing indeed that the surface is formed by small sized (roughly 20 nm wide) square-shaped terraces, and exposes several successive atomic planes. This morphology is quite typical of metal-

oxide surfaces and clearly indicates that terrace edge could play a quite relevant role in the determination of the surface properties.

XPS and HREELS characterization

Surface cleanliness was checked by means of XPS. In Figure 5.1.2 the core level peaks of Zn2p and the O1s are shown. The line shapes of the core levels of the XP spectra were fitted with Voigt multiplets with fixed Lorentzian width (w_l, see Table 5.1.1). The O1s core level is clearly skewed on the high binding energy side. It was fitted with two components: the main one is located at 530.9 eV binding energy and corresponds to bulk oxygen contribution, while the shoulder at 532.9 eV binding energy corresponds to oxygen atoms of adsorbed hydroxylic group. This second component is therefore a clear indication of the presence of adsorbed water on the surface, as reported in literature[1].

	w_l	w_g	BE (eV)
Zn 2p	0.4	0.8	1022.2
O $1s_a$	0.1	0.7	530.9
O $1s_b$	0.1	0.8	532.9

Table 5.1.1: Fitting parameters of the O 1s components and the Zn 2p core level.

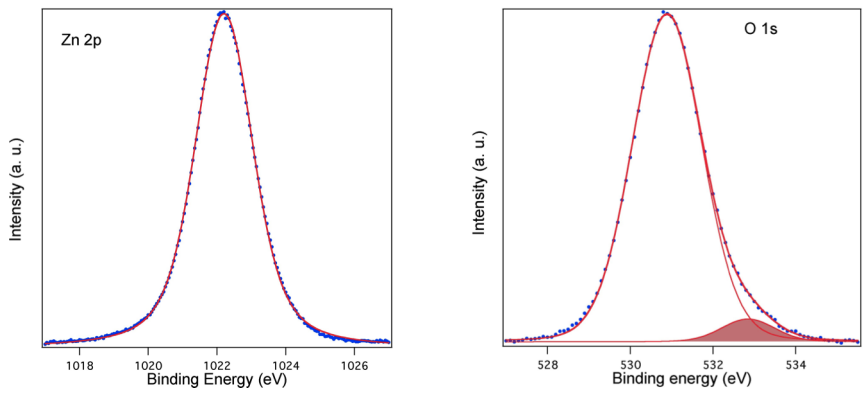

Figure 5.1.2: XPS core levels of the ZnO(10$\bar{1}$0) clean surface. (a) O1s core level, (b) Zn2p core level

This finding is also supported by HREELS measurements. Figure 5.1.3 panel a) shows the vibrational region of the clean surface HREELS spectrum.

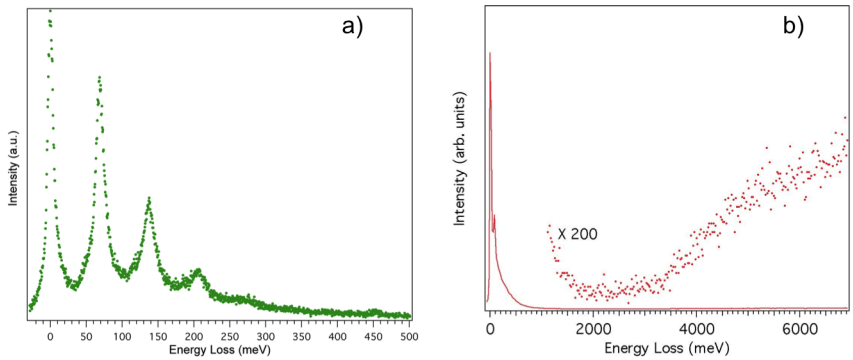

Figure 5.1.3: In the panel a) the vibrational region of the HREELS spectrum for the ZnO clean surface is shown. The panel b) shows the electronic transition region.

An extremely intense loss peak is located at 69 eV, which is due to the Fuchs-Kliewer optical phonon. Its replicas are also visible. The intensity of those features dominates the energy loss spectrum in the 0-300 meV region, where usually fingerprint molecular vibrations are observed. Nevertheless, a feature at 456 meV (3675 cm^{-1}) is clearly visible, which is attributed to the OH stretching mode of partially dissociated water adsorbed on the surface[2], confirming XPS results.

Figure 5.1.3 panel b) shows the HREEL spectrum in the 0-7 eV energy loss region, where fingerprint of electronic transition could be observed. Despite the very small intensity, the onset of electronic transition can be clearly observed at 3.4 eV, corresponding to the ZnO band gap value. This result shows that, despite the fact that the surface could not be considered as ideal (due to the presence of terrace edges, sputtering induced defects and water contamination), the band gap preserve its ideal bulk-like value.

Evaluation of Fermi level position

As explained in Chapter 3, due to the presence of intrinsic defects formed during the crystal growth, ZnO is typically n-doped. The value of the carrier density determines the position of the Fermi level in the gap, and is therefore a relevant parameter for the discussion of

the interface electronic properties. For this reason, we have performed Hall measurements on the ZnO sample, previous to functionalization. The measured Hall resistance (R_H) is related to the n-type carrier density n by :

$$R_H = \frac{1}{ned} \tag{5.1.1}$$

where e is the electron charge (C/cm^2) and d is the lateral dimension of the sample (0.5 mm). The measured value of R_H was 49.9 Ohm/T , leading to an estimated value for $n = 2.5 \cdot 10^{14} cm^{-3}$

From this value we obtain the energy position of the Fermi level in the ZnO gap as:

$$E_F = \frac{E_g}{2} + kTln\frac{n}{n_i} \tag{5.1.2}$$

where E_g is the energy gap of the ZnO, 3.4 eV, and n_i is the intrinsic carrier density (which can be calculated knowing the values of the electron and hole effective masses: 0.24 m_e and 0.59 m_e respectively). We thus obtained that in the bulk, the Fermi level is located at 3.1 eV from the valence band edge, i.e 0.3 eV below the ZnO conduction band.

5.2 The catechol/ZnO interface

5.2.1 Catechol adsorption

Catechol adsorption on the ZnO surface has been characterized by means of XPS. Saturation coverage was obtained at a catechol dosage of 1000 Langmuir. The XPS quantitative determination of the coverage, calculated as explained in the experimental section, gives a rough estimate of 0.12 molecule per ZnO unit cell, corresponding to one catechol molecule every eight ZnO unit cell. A possible explanation of this quite low value is given at the end of this paragraph.

In Figure 5.2.1 on page 82 the C1s core level peak of the catechol/ZnO interface at saturation coverage is shown. The C1s line-shape is quite broad and can be fitted by two

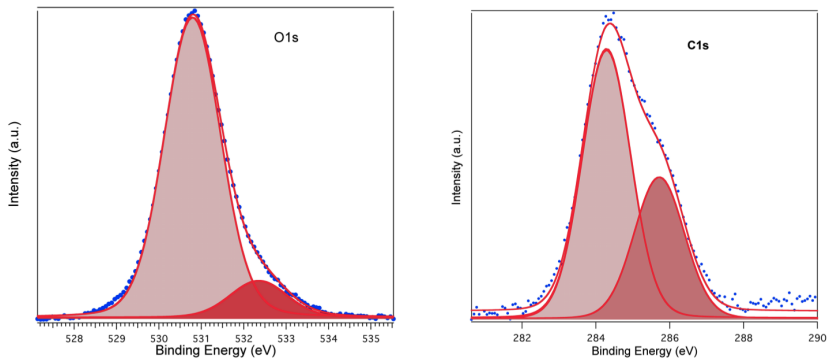

Figure 5.2.1: O1s and C1s core level peaks for the catechol/ZnO system for the saturation coverage

components at 284.3 eV and 285.7 eV binding energy, corresponding to aromatic carbon and to carbon bonded to the hydroxyl group, respectively[3, 4]. The ratio of their areas is stoichiometric (see Figure 5.2.1), demonstrating that the molecule adsorbs intact on the surface.

Figure 5.2.1 shows also the O1s line-shape for the saturation coverage. The peak presents a clear shoulder at the high energy side and is fitted with two components. The component at 532.4 eV ($O1s_b$) is ascribed to the oxygen atoms of the molecule and increases during catechol evaporation.

The ratio between the area of $C1s_b$ and $O1s_b$is not stoichiometric, presenting a clear excess of oxygen. This can be reasonably ascribed to the hydrophilicity of the molecule, i.e. to the fact that residual water remains most probably bonded to the catechol molecules during dosage, thus determining the co-adsorption of water and/or hydroxyl moieties on the surface. This might be also the reason for the measured low value of saturation coverage.

5.2.2 Electronic properties

The electronic properties of the catechol/ZnO($10\bar{1}0$) interface was investigated by means of UPS.

Figure 5.2.2, shows the UPS valence band spectra of the clean ZnO($10\bar{1}0$) surface and of the saturation coverage Catechol/ZnO system. For the clean surface, the Zn3d peak

	BE	I/I_{Zn}
O 1s $_b$	532.4	0.13
C $1s_a$	284.3	0.13
C $1s_b$	285.7	0.06

Table 5.2.1: Value of the binding energy (BE) of the C1s and O1s core levels components for functionalized surface. The intensities of the components normalized to the respective intensity of Zn core level peak (I/I_{Zn}) are shown. The area ratio is normalized with the atomic sensitivity factor (ASF)

is located at 10.85 eV binding energy, while the two features located at 7.85 and 4.6 eV binding energy are related to oxygen states. When Catechol adsorbs on the ZnO surface, the Zn 3d peak shifts to lower binding energy, at 10.70 eV. In the lower binding energy region of the spectrum we find a new feature at 6.7 eV, which is attributed to molecular states[5, 6]. More interesting, a feature appeared at 2.3 eV binding energy, which is attributed to the HOMO of the molecule[5, 6]. The molecular HOMO therefore lies in the energy gap of the ZnO, at roughly 0.7 eV from the valence band edge. This finding is in agreement with the results reported by Rangan et al.[6] on the ZnO($11\bar{2}0$) surface and with the theoretical calculations of Calzolari et al.[7] on the catechol/ZnO($10\bar{1}0$) system, confirming the type-II character of this interface.

The modification of the interface ionization energy has been evaluated from photoemission data, taking into account both the work function (W_F) and the band bending variations ΔV_{bb} induced by molecular adsorption, according to the following equation[8]:

$$\Delta I = \Delta W_F + \Delta V_{bb} \tag{5.2.1}$$

where I is the ionization energy, defined as:

$$I = W_F + (E_F - E_{Vb}) + (E_{Vb} - E_{Vs}) \tag{5.2.2}$$

where E_{Vb} and E_{Vs} are the energy VB maximum in the bulk and at the surface respectively.

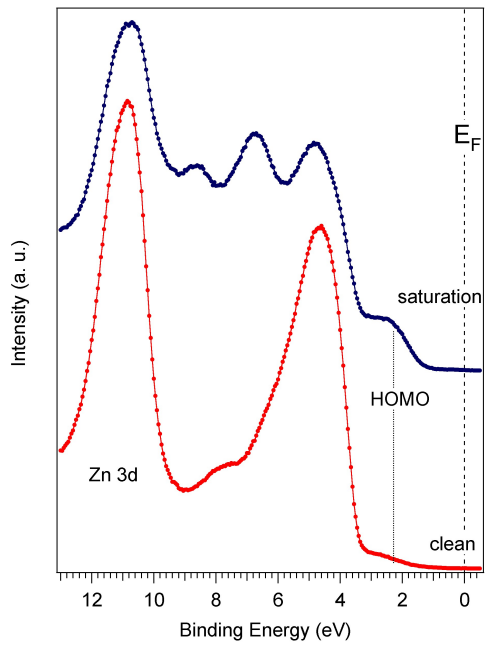

Figure 5.2.2: UP spectra of clean ZnO(10$\bar{1}$0) surface and the saturation coverage.

Analyzing UPS valence band spectra, we noticed that the Zn3d shifts by 0.15±0.1 eV towards lower binding energy upon catechol evaporation. This small shift is attributed to an upward band bending occurring upon the interface formation. The behavior of the interface work function upon adsorption was also measured by means of UPS, finding that it increases up to 0.45±0.1 eV at saturation coverage. This data corresponds to a variation of the ionization energy of $0.45 - 0.15 = 0.3 \pm 0.1\, eV$.

This small increase in the ionization energy value indicates the formation of an interface dipole layer which points towards the surface, i.e. with the positive charge near the surface and the negative charge towards the vacuum. The catechol isolated molecule is characterized by a dipole molecular moment of 0.94 D, directed form the hydroxyl groups to the benzene ring. As the molecule is bonded to the surface through the hydroxyl groups, a decrease of the ionization potential should actually be expected upon adsorption, at variance with our observation. Two possible explanation for this finding can be found: on one hand, as mentioned before, a certain amount of water is brought to the surface together with the catechol moiety. This presence could undoubtedly affect the ionization

potential value, due to the dipole moment of water and/or hydroxyl groups. As the exact geometry and chemical state of the adsorbed water molecule is not known, it is difficult to quantitative evaluate its role. Moreover, following the results of Calzolari et al.[7], we note that the catechol moiety undergoes a distortion upon adsorption, characterized by the moving upward of the OH "arms". This distortion surely affects the molecular dipole moment, possibly reducing its value. A more precise evaluation of this effect will be considered in paragraph 5.3, where 4-nitrocatechol adsorption is discussed.

5.3 The 4-Nitrocatechol/ZnO interface

The experimental results presented in the following were extensively compared to the results of a DFT theoretical calculation performed by A. Calzolari et al [7]. In some case their analysis is strongly based on these theoretical predictions. For this reason and for sake of completeness, in the following we will briefly summarize the main details of this calculation.

The calculations of adsorption geometries, electronic properties of the functionalized surface, and core level shifts (CLS) were carried out by A. Calzolari et al. within the Density Functional Theory (DFT) framework, in the planewave pseudopotential implementation, as coded in the Quantum-Espresso package[9]. The C 1s core level shifts were calculated in the pseudo-potential formalism by using the final state theory[10, 11], the specific pseudo-potential reproduces the core-excited electron configuration C*(1s1 2s2 2p2). Calculations were performed in supercells with 3×2 ZnO($10\bar{1}0$) lateral periodicity and six ZnO bilayers, with one 4-nitrocatechol molecule symmetrically adsorbed on each surface. Slab replicas were separated by 12 Å of vacuum, and each structure was fully relaxed, until forces on all atoms become lower than 0.03 eV/Å.

The structure optimization of the ZnO($10\bar{1}0$) surface reveals the formation of ordered rows of buckled Zn-O dimers along the polar [0001] direction [12]. The initial configuration of the hybrid system was prepares by setting the molecule at $\sim$ 3.2 Å from the surface, with the phenyl ring perpendicular to the surface dimers. During relaxation, the molecule

chemisorption occurs spontaneously by creation of two Zn-O bonds with the Zn atoms belonging to two consecutive Zn-O dimers, and formation of two hydrogen bonds between the molecule and the substrate[7]. The surface does not exhibit structural distortion, except for the buckling removal occurring for the dimers involved in the chemisorption. The final adsorption geometry is sketched in Figure 5.3.1.

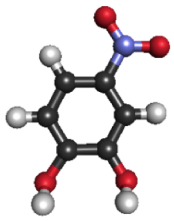

Figure 5.3.1: Theoretical adsorption model of 4-nitorcatechol on ZnO(10$\bar{1}$0) surface, distorted configuration

5.3.1 4-Nitrocatechol adsorption

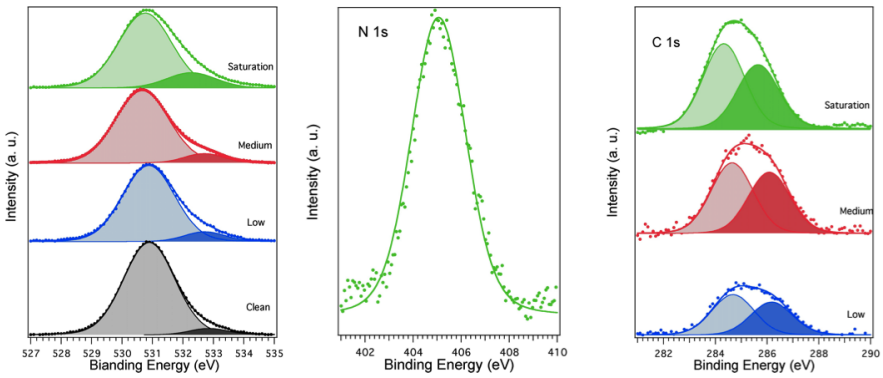

Figure 5.3.2: Left panel: O1s core level peak for the clean ZnO(10$\bar{1}$0) surface, low, medium and saturation coverage of 4-nitrocatechol on ZnO(10$\bar{1}$0) surface. Middle panel: N1s core level peak of the saturation coverage 4-nitrocatechol/ZnO(10$\bar{1}$0) surface. Right panel: C1s core level peaks for different evaporation rate.

The adsorption of 4-nitrocatechol on the ZnO(10$\bar{1}$0) has been characterized by means of XPS. As the evaporation conditions for this molecule are more controlled than for the catechol moiety, we expected to obtain a more defined interface, and therefore to be able to quantify in more details the effect of molecular adsorption on the electronic properties

of the interface.

In Figure 5.3.2 the O1s core level of 4-nitrocatechol/ZnO($10\bar{1}0$) is reported. It has been fitted with two components: the main peak, corresponding to bulk oxygen, lies at 530.7 eV, while the second component at 532.3 eV is attributed to the -NO_2 and OH Oxygens of the 4-nitrocatechol molecule[13]. The N1s core level is also shown in Figure 5.3.2: a single component at 405.15 eV binding energy is observed, and attributed to the NO_2 species[13].

Saturation	BE (eV)	w_g	w_l	I/I_{Zn}
O $1s_b$	532.8	0.9	0.08	0.42
C $1s_a$	284.2	0.8	0.08	0.50
C $1s_b$	285.0	0.7	0.08	0.16
C $1s_c$	285.8	0.8	0.08	0.23
N1s	405.1	1.0	0.7	0.14

Table 5.3.1: Fitting parameters and intensity of molecular C1s, N1s and O1s core level spectra related to the saturation coverage.

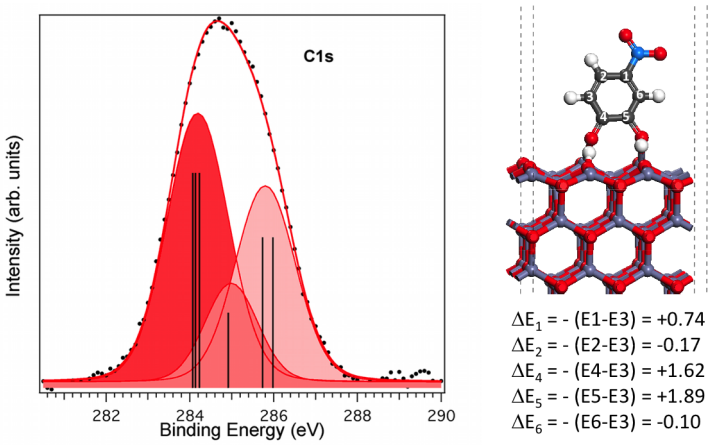

Figure 5.3.3: Left panel: C1s core level peak of saturation coverage 4-nitrocatechol/ZnO($10\bar{1}0$) surface. Right panel: the front view of the 4-nitrocatechol molecule chemisorbed on ZnO($10\bar{1}0$) surface and the relative position in binding energy of the C1s core level components.

In Figure 5.3.3 the spectrum of the C1s core level at saturation coverage is shown. The presence of molecular carbon atoms in different chemical states gives rise to a broad

shape. Our instrumental resolution did not allow us to directly resolve each component. We nevertheless were able to draw a quantitative analysis of the C1s core level comparing our data with the theoretical prediction of the C1s core level shift calculated by A. Calzolari and co-workers explicitly for the 4-nitrocatechol/ZnO system. In the left panel of Figure 5.3.3 the theoretical results are reported as vertical line superimposed to the experimental spectrum. They found that the three aromatic carbons are almost degenerate in energy, and therefore built up a single component at low binding energy; according to theory the core level C-NO_2 contribution is shifted by +0.83 eV to higher binding energy, while that of the two C-OH atoms are shifted by +1.75 eV with respect to the aromatic carbon core levels. On the basis of these theoretical results, we fit the experimental core level shape with three components, as shown in Figure 5.3.3. As reported in Figure 5.3.1, the main C1s component is located at 284.2 eV, while the other two are at 285 eV and 285.8 eV, respectively, corresponding to core level shifts of 0.8 and 1.6 eV, in excellent agreement with theory. The areas of the three components also follow the theoretical prediction, being in a 3:1:2.2 ratio. In addition, the area ratio between N1s, C1s and the molecular component of O1s core levels are also in agreement with molecular stoichiometry. These finding clearly indicates on one hand that the molecule adsorbs intact on the surface, preserving its stoichiometry. On the other hand they show that in this case the presence of co-adsorbed water is almost negligible. The molecular coverage based on quantitative XPS analysis (see Chapter 4) gives a saturation molecular density of 0.18 molecules per ZnO unit cell. This saturation coverage corresponds roughly to one 4-nitrocatechol molecule every six ZnO unit cell.

5.3.2 UPS and HREELS - Electronic properties

The electronic properties of 4-nitrocatechol/ZnO interface were characterized combining the results of UPS and HREELS measurements and comparing with the results of DFT calculations.

In Figure 5.3.4 the experimental valence band (VB) spectra of the clean ZnO surface

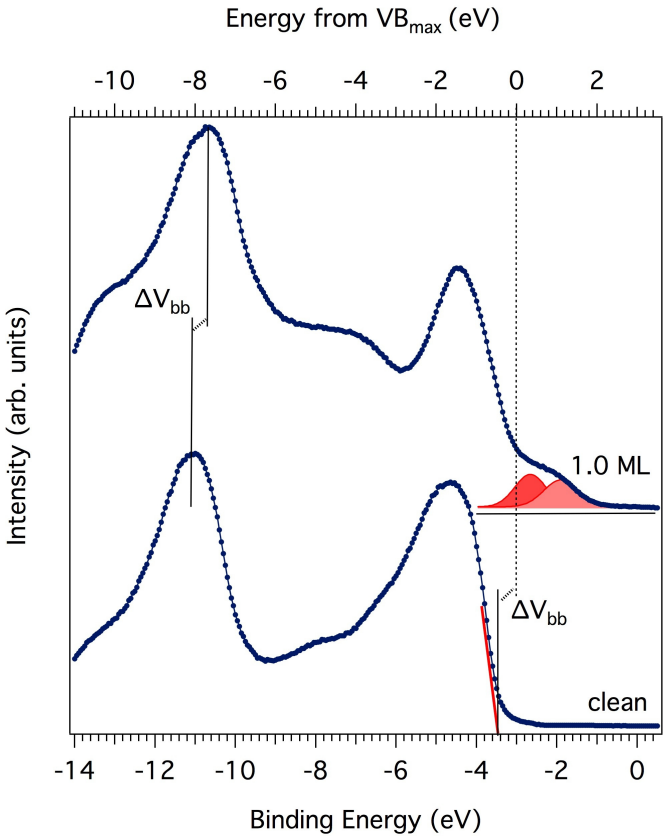

Figure 5.3.4: UPS valence band spectra of the clean ZnO(10$\bar{1}$0) surface and 4-nitrocatechol/ZnO system.

and 4-nitrocatechol/ZnO interface are reported. The spectra are dominated by the Zn3d peak, located 10.65 eV binding energy, and by a lower binding energy feature located at roughly -4 eV, which is mainly due to Oxygen states. Upon increasing coverage, a distinct feature appears in the energy gap region of the UPS spectra. Figure 5.3.4 shows the spectral shoulder fitted with two Gaussian components located at 1.1 eV (HOMO) and 0.4 eV (HOMO-1) above ZnO valence band top.

For these assignments we referred to theoretical prediction by Calzolari and co-workers. Figure 5.3.5 shows the total density of state for the 4-nitrocatechol/ZnO system. In the gap region two feature are visible, labelled with H, corresponding to the HOMO and

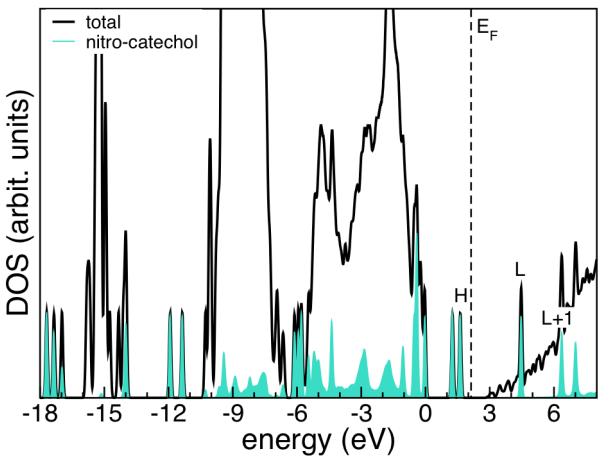

Figure 5.3.5: Total density of states (black line) and its projected contribution on 4-nitrocatechol (cyan line) for the molecule/ZnO interface system. The zero of the energy scale corresponds to the valence band top of the ZnO substrate. The peaks corresponding to the molecular frontier orbitals are also indicated.

HOMO-1 molecular states. The agreement between experimental and theoretical value of the HOMO and HOMO-1 position with respect to the valence band edge is quite good. We note that the slight energy discrepancy between the experimental and theoretical states can be traced back to small differences in the adsorption geometry details between the ideal and the real surfaces. The residual presence of H_2O molecules and -OH groups in the experimental system may also affect its electronic properties. Moreover in the case of catechol adsorption on anatase, the energy position of the HOMO state has been found to vary with the molecular adsorption sites (i.e. surface defects vs flat terraces). Furthermore a possible influence of molecular dimer formation on the HOMO position has been proposed[5]. As in the case of catechol, also 4-nitrocatechol forms a staggered type-II interface with non-polar ZnO surface, with unperturbed molecular states in the substrate pristine band gap. We here note that the predicted effect of the molecular ionization energy on the alignment of the molecular levels relative to the metal-oxide bands[7] cannot be observed experimentally. Indeed, the HOMO position is almost the same in both the catechol and 4-nitrocatechol systems. Again, this discrepancy might be due to the non-ideality of the real interfaces.

The energy determination of the empty states of the 4-nitrocatechol/ZnO($10\bar{1}0$) system

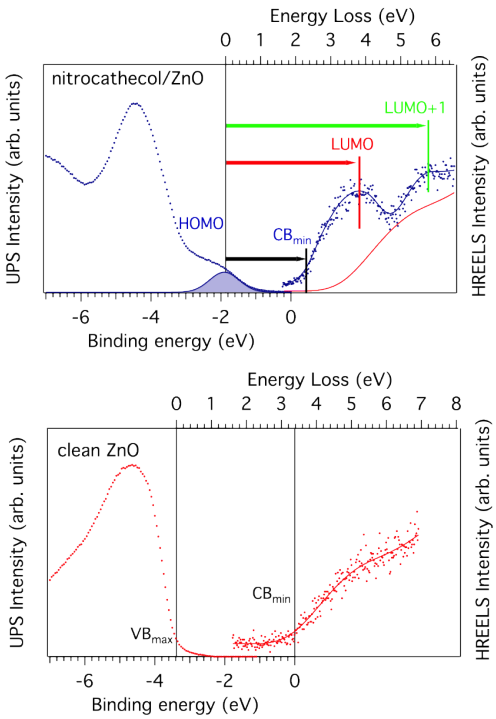

Figure 5.3.6: (a): UPS VB spectrum (left axis) and HREELS spectrum (right axis) of the clean ZnO(10$\bar{1}$0) surface. (b): UPS VB spectrum (left axis) and HREELS spectrum (right axis) of the 4-nitrocatechol/ZnO(10$\bar{1}$0) surface. For both the HREELS data, a spline curve is also shown as guide for eyes.

has been obtained by combining UPS results with HREELS measurements taken in the electronic transition energy loss region (0 - 7 eV). In Figure 5.3.6 the energy loss spectrum of the clean ZnO(10$\bar{1}$0) (a) and 4-nitrocatechol/ZnO(10$\bar{1}$0) (b) surfaces are reported, suitably matched with the corresponding UPS VB spectra: in (a) the UPS valence band edge, i.e the highest occupied level, is made to coincide with the zero of the HREEL spectrum; in (b) this zero coincides instead with the HOMO position.

As already discussed, the HREELS clean surface curve displays an onset at 3.4 eV, which correspond to the electron excitation across the ZnO band gap. Upon 4-nitrocatechol adsorption the electron transition onset reduces to 2.3 eV and two broad pronounced features appear at 3.8 eV and 5.8 eV. The red shift of the onset correspond to a HOMO$-$CB$_{\mathrm{min}}$ electronic transition, and reflects the narrowing of the interface band gap due to the pres-

ence of molecular states inside the ZnO gap. The feature at 3.8 eV is attributed to the HOMO−LUMO transition, while that at 5.8 eV corresponds to HOMO−(LUMO+1) transition. The assignments are in agreement with optical absorption measurements on 4-nitrocatechol in aqueous solution, that reported two main absorption peaks at 3.59 eV and 5.21 eV, attributed to HOMO−LUMO and HOMO−LUMO+1 transitions, respectively[14]. The experimental results set the LUMO and LUMO+1 levels 1.5 eV and 3.5 eV above the CB_{min}, respectively.

The simulated DOS reported in Figure 5.3.5 reproduces the same spectral features (Figure 5.3.4) dominated by two prominent peaks, corresponding to the unperturbed LUMO (∼1.4 eV above CB_{min}) and LUMO+1 (∼ 3.4 eV above CB_{min}) molecular states degenerate with the ZnO conduction band.

5.3.2.1 Band bending

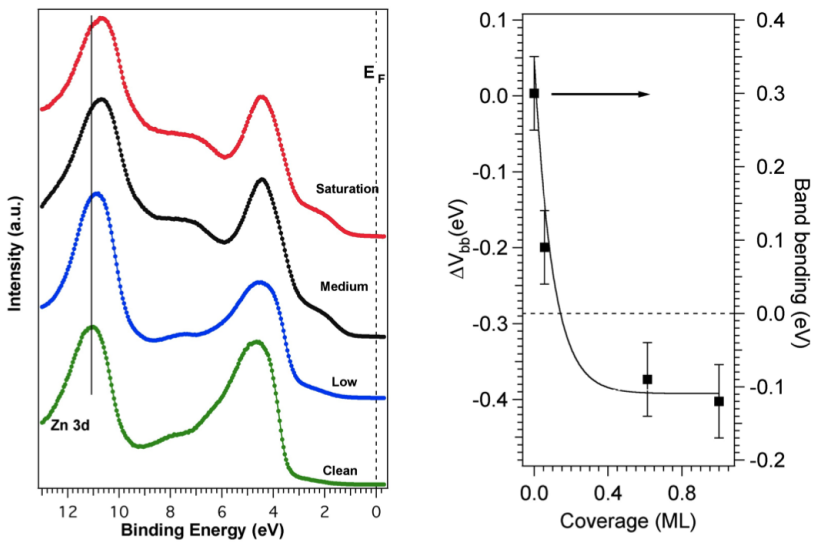

Figure 5.3.7: Left panel: VB spectra of the clean surface and different coverages. Right panel: band bending as a function of 4-nitrocatechol coverage. The right axis shows the variation of band bending relative to the flat band condition (horizontal dashed line), as determined by the bulk Fermi level position.

For the clean surface, extrapolation of the low-energy leading edge of the spectrum to

zero intensity set the energy position of the valence band maximum (VB_{max}) at 3.4±0.1 eV below the Fermi level, indicating that Fermi level is degenerate with the conduction band minimum (CB_{min}). As obtained with Hall effect measurement in the bulk, the Fermi level lies 0.3 eV below CB_{min}[14]. This means that on the clean surface the bands are slightly downward bended (V_{bb}= 0.3 eV) in agreement with previous reports[15].

An accurate analysis of the VB spectrum of the 4-nitrocatechol/ZnO system points out a rigid shift of the whole spectrum towards lower binding energy upon 4-nitrocatechol adsorption, corresponding to an upward shift of the bands. The tracking of the energy position of the Zn 3d peak shows a band banding variation of -0.4±0.1 eV at saturation coverage as depicted in Figure 5.3.7. Adsorption of this chromophore determines therefore a overall upward band banding V_{bb}= -0.1 eV (as shown in Figure 5.3.7, right panel), leading to the formation of a small depletion layer at the ZnO surface.

5.3.2.2 Work function and ionization potential

The work function variation occurring upon molecular adsorption was measured following the shift of the photoemission secondary electron edge. In Figure 5.3.9 the changes in The work function and band bending values are reported as a function of 4-nitrocatechol coverage: the change in band bending saturates at -0.4 eV, while the work function variation is 1.7 eV. The corresponding variation of the ionization energy is also shown in Figure 5.3.9, saturating at the quite impressive value of 1.3 eV. This leads to a strong downward shift of the whole valence band relative to the vacuum level.

As previously discussed, this variation is caused by the formation of an interface dipole layer upon 4-nitrocathecol adsorption. The origin of this dipole layer can be sought in the significant dipole moment of the 4-nitrocathecol molecule, which is directed from the NO_2 to the OH groups and therefore tends to shift up the vacuum level. A quantitative prove of this fact can be derived considering the results of DFT calculations. In Figure 5.3.10, the macroscopic average of the Hartree and external potential energies (ΔV_{macro}) of the clean and the 4-nitrocathecol functionalized ZnO surfaces, calculated as described

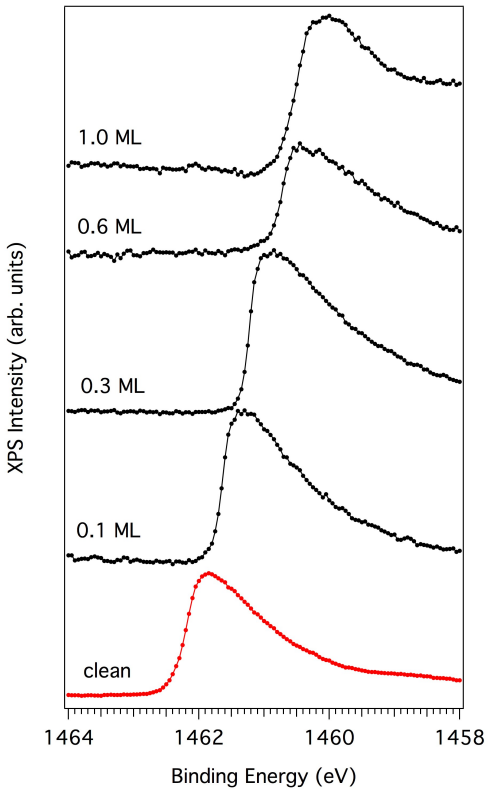

Figure 5.3.8: XPS spectra in the secondary electron cutoff region as a function of 4-nitrocatechol coverage.

in Ref.[16], are reported. In each curve, the asymptotic value of ΔV_{macro} (for positive z values outside the surface) provides an estimate of the system vacuum level position. The difference between the values of the two curves is a measure of the ionization energy change induced by functionalization[17]. In this frame, the theoretical prediction for ionization energy variation is 1.6 eV, which reproduces quite well the experimentally observed value. In simpler terms, the variation in the ionization energy induced by the interface dipole layer can be expressed within the simple parallel-plate capacitor[17], as:

$$\Delta I = \frac{e\mu_{\perp}\theta}{\epsilon_0} \tag{5.3.1}$$

where $\mu_{\perp}$ is the component of the molecular dipole moment perpendicular to the surface, θ is the molecular density and ε_0 the vacuum dielectric constant. Considering a

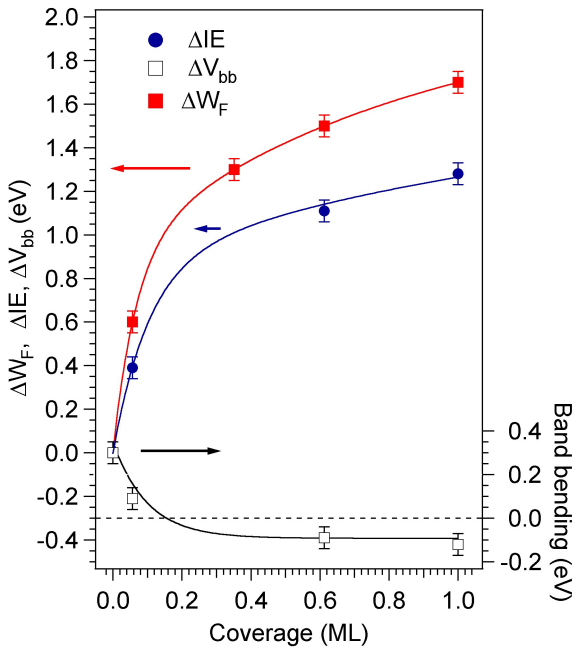

Figure 5.3.9: Variation of work function, band bending and ionization potential energy as a function of 4-nitrocatechol coverage.

molecular density corresponding to the (3×2) structure (which is also consistent with the experimental molecular density value), this model easily provides an estimate of $\mu_\perp$ from the value of ΔI. If the experimental value ΔI=1.3 eV is considered, we obtain $\mu_\perp$=3.7 D. This value coincides with the theoretically calculated value for the dipole moment of the isolated molecule, thus demonstrating that the observed ionization potential variation can be fully accounted for by just considering the molecular dipole moment in the adsorbed geometry. We note that the small discrepancy between theoretical and experimental values could be easily rationalized considering the inevitable differences, in terms of defects, step edges and small amounts of contaminants, between the ideal and the real interface.

The results here presented lead to few further considerations.

The combined UPS and HREELS data for 4-nitrocatechol/ZnO system point out that surface functionalization preserve the clean ZnO band gap value, i.e. the distance between CB_{min} and VB_{max} is not affected by adsorption. Indeed, it is easy to show from the HREELS value of the HOMO$-CB_{min}$ distance (2.3 eV) and the position of the HOMO

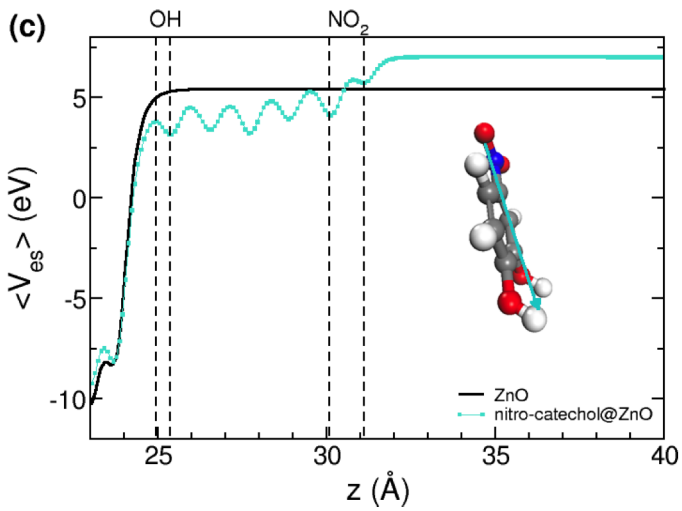

Figure 5.3.10: Macroscopic average of the electrostatic potential for the clean (black line) surface and 4-nitrocatechol/ZnO surface (cyan line). The inset shows the molecule geometry in the chemisorbed configuration: the corresponding electric dipole is also indicated as an arrow.

state derived by UPS (1.1 eV from the VB_{max}), the distance between the semiconductor band edges (3.4 eV) does not change relative to the clean surface. This means that molecular adsorption does not induce significant density of states around the CB_{min}, i.e. that ionization energy and electron affinity are affected in the same way by molecular adsorption.

The simple capacitor model implies a direct relationship between the orientation of the molecular dipole (inward/outward the surface) and the upward/downward shift of the ionization energy. This, along with the observed rigidity of the band-gap, provides also a connection between the orientation of the molecular dipole and the modification of the conduction band, and consequently of the open-circuit voltage of DSSCs. It is interesting to note that the slightly higher value of the ΔI theoretical prediction (1.6 eV) relative to the experimental one, corresponds also to a higher value of $\mu_{\perp}$= 4.57 D. Indeed, the calculated dipole molecule of the adsorbed molecule, which is characterized by a distorted configuration due to the upward bending of the OH groups, is higher than that of the isolated molecule. This theoretical results clearly indicates that the details of molecular adsorption and in particular possible molecular distortions, could play a

significant role in the exact determination of vacuum level variations. To this regards, UHV-based spectroscopic investigations can provide precise evaluations of the dipole layer effect in real dye/semiconductor interfaces.

5.4 Co-evaporation of 4-nitrocatechol and ethanol

DSSC are characterized by an extended interface, in which several components are in intimate contact. Disentangling the role of each component in the determination of DSSC activity and in particular of energy level alignment is a complex task. In this thesis work, we are investigating model systems which could help understanding the mechanisms of interface level alignment. The previously exposed results have clearly shown the importance of the molecular dipole moment in the determination of the interfacial ionization energy and electron affinity. We pursued this idea considering how co-adsorption of different molecules can alter both the interface dipole layer and the molecular level alignment. We therefore decided to investigate the effect of Ethanol (EtOH) co-evaporation on the 4-nitrocatechol functionalized surface. We chose EtOH for two reasons: it is the solvent used for the pastes of DSSC and it is characterized by an opposite dipole momentum with respect to the 4-nitrocatechol.

5.4.1 Ethanol/ZnO interface characterization

We first investigated the adsorption of EtOH on the clean ZnO($10\bar{1}0$) surface. The molecule was evaporated till saturation coverage, corresponding to 420 L (where 1 Langmuir = 10^{-6} Torr $\cdot$ s) . The adsorption of the molecule was checked using XPS technique. In Figure 5.4.1 the O1s core level peaks for the clean ZnO surface and the EtOH/ZnO system are shown. We fitted both peaks with two components. For both systems the component $O1s_a$ at 530.9 eV binding energy is attributed to the bulk Oxygen. For the clean surface the component at 532.5 eV, the $O1s_{b,}$ is attributed to the OH groups present on the surface due to dissociated water. In the EtOh/ZnO spectrum, the component at 532.4

eV binding energy corresponds to the OH group of the EtOH molecule. The EtOH/ZnO C1s core level peak was fitted with two component (see Figure 5.4.1). The component at 284.9 eV binding energy is attributed to the methyl Carbon (-CH_3) while the component at 286.2 eV binding energy ($C1s_b$) is attributed to the Carbon bonded to the hydroxylic group.

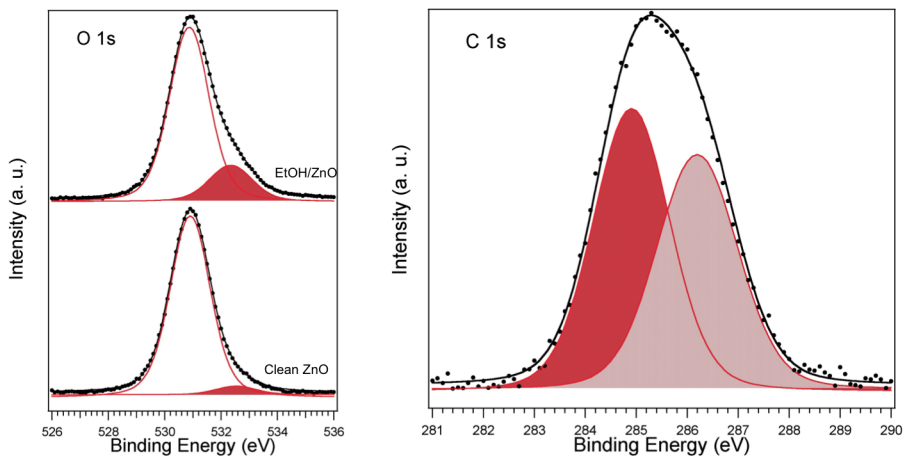

Figure 5.4.1: XPS measurements of EtOH/ZnO system. Left panel: O1s core level spectrum for the clean (bottom) and the evaporated surface (top). Right panel: C1s core level spectrum for the evaporated surface.

The intensity ratio between the two C1s components is 1:1.17, i.e. fairly stoichiometric. The ratio between the $C1s_b$ and the $O1s_b$ components is 0.6, which means that a small excess of water is present on the surface, probably dosed together with the EtOH molecule. The estimated coverage corresponds to one EtOH molecule every two ZnO unit cell.

	BE(eV)	W_g	Cov
$O1s_a$	530.8	0.7	0.78
$O1s_b$	532.4	0.77	0.26
$C1s_a$	284.9	0.8	0.23
$C1s_b$	286.2	0.85	0.20

Table 5.4.1: Fitting parameters for the O1s and C1s core level analysis for the EtOH coverage (Cov). Intensity normalized the the Zn2p core level area are also shown.

We investigated the electronic properties of this system using UPS technique. Figure 5.4.2 shows the valence band UPS spectra for the clean and evaporated surface. In the EtOH/ZnO spectrum the Zn3d peak lies at 10.95 eV binding energy and is therefore shifted by 0.45±0.05 eV relative to the clean surface (E_{Zn}= 10.50 eV).

The observed shift in the Zn3d UPS peak upon EtOH adsorption is related to surface band bending. This downward band bending is probably due to electron donation from the molecule to the substrate, similar to what has been reported in the case of H_2 adsorption on the same surface[18]. It is important to notice that no clear feature due to molecular states is revealed, in particular in the gap region.

Moreover, work function measurements gives a variation ΔW_F of - 0.8±0.1 eV, i.e. in the direction opposite to that of 4-nitrocatechol. We therefore conclude that, while EtOH adsorption does not introduce any relevant feature in the gap region of the semiconductor, it significantly affects the semiconductor band position relative to both the Fermi level (downward band bending) and the vacuum level. Indeed, the decrease of the ionization energy corresponds to -0.35 eV and is consistent with the direction of the EtOH dipole moment, which points from the OH group to the CH_3, i.e. outwards relative to the surface plane.

5.4.2 Ethanol/4-nitrocatechol/ZnO interface characterization

The second step of this investigation is to evaporate 720 L EtOH (till saturation) on the ZnO surface which has been previously partially functionalized with 4-nitrocatechol. From XPS measurements we can estimate the 4-nitrocatechol coverage as roughly one fifth of the saturation value. In Figure 5.4.3, left panel, the O1s core level peak of the partially functionalized surface is shown. It can be fitted with two components, set at 530.9 eV and 532.6 eV binding energy respectively. The first feature is due to the bulk Oxygen while the second one is attributed to the NO_2 and hydroxylic groups of the 4-nitrocatechol molecule. The right panel of Figure 5.4.3 shows the C1s core level spectrum of EtOH evaporated on ZnO surface compared to C1s core level of EtOH evaporated on 4-nitrocatechol/ZnO and of the 4-nitrocathecol/ZnO interface. The difference between the C1s intensity of

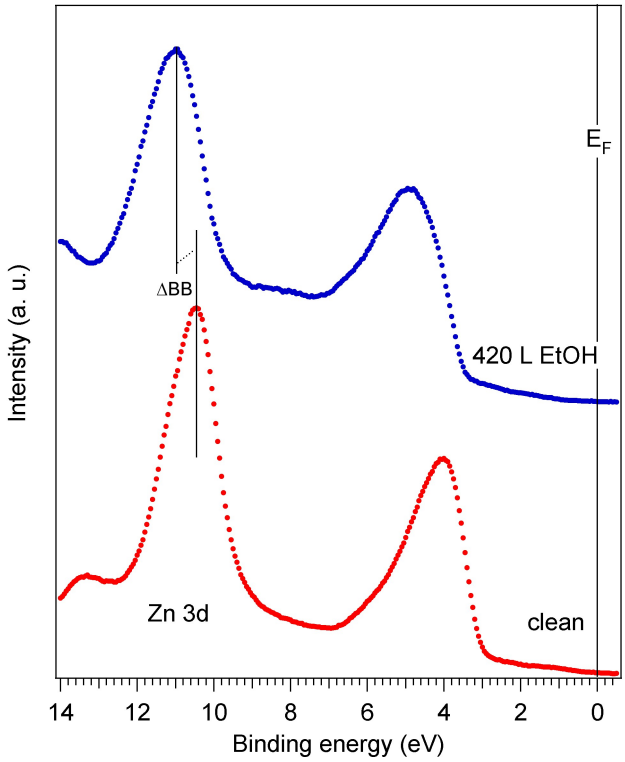

Figure 5.4.2: UPS VB spectra of the clean ZnO surface and the functionalized surface.

EtOH/4-nitrocatechol/ZnO and that of 4-nitrocatechol/ZnO gives us an estimate of the amount of co-adsorbed EtOH molecules. This amount is quite small, and corresponds roughly to 0.15 of the EtOH saturation coverage.

When EtOH is added to the 4-nitrocatechol pre-dosed surface, the Zn 3d peak moves toward higher binding energy. The band banding variation, measured with respect to that of the 4-nitrocatechol, is -0.15 eV and is in the same direction of that caused by EtOH adsorption on the clean surface. This finding can be explained considering that EtOH adsorption takes place in those surface areas left clean by 4-nitrocatechol, and has therefore an effect similar to that observed on the clean surface. Upon EtOH adsorption the W_F shift back by -0.3±0.1 eV relative to the 4-nitrocatechol value. Overall, the ionization energy change due to EtOH adsorption amounts to -0.23 eV.

This variation can be ascribed to the EtOH dipole moment, which is opposite to that of 4-nitrocatechol. This finding shows that it is possible to modify the interface

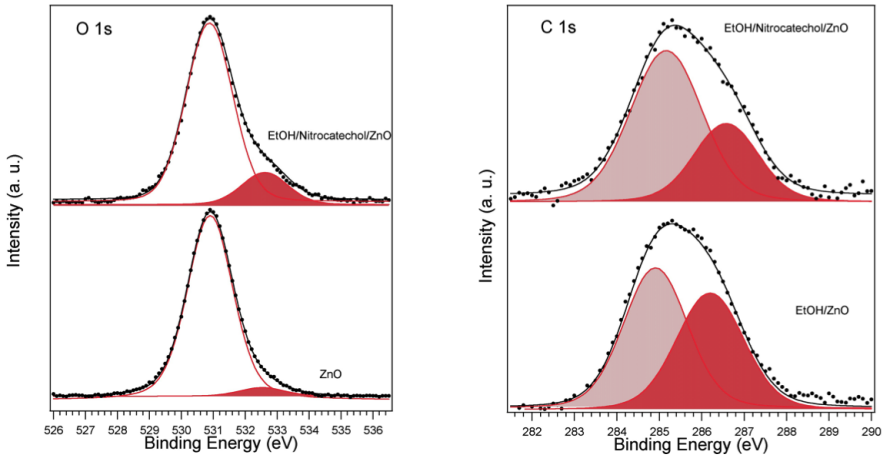

Figure 5.4.3: Left panel: O1s core level of the clean surface and the EtOH/4-nitrocatechol/ZnO system. Right panel: C1s core level spectra of the EtOH/ZnO and EtOH/4-nitrocatechol/ZnO

	ΔW_F(eV)	ΔV_{bb}(eV)	ΔI (eV)
EtOH/ZnO	-0.80	0.45	-0.35
4-nitrocatechol/ZnO	1.70	-0.40	1.30
4-nitrocatechol(partial)/ZnO	1.15	-0.23	0.92
4-nitrocatechol/EtOH/ZnO	-0.30	0.07	-0.23

Table 5.4.2: ΔW_F ΔV_{bb} ΔI values for different EtOH and 4-nitrocatechol co-evaporation are shown.

ionization energy by evaporating a molecule with opposite dipole moment with respect to the 4-nitrocatechol. Interesting, the ionization energy variation is larger than it would be expected if, in agreement with Eq 5.3.1, proportionality to the amount of adsorbed molecule is supposed. This finding suggests that the EtOH dipole moment in the co-adsorbed system is larger than that of the homogenous EtOH saturation layer and can be explained taking into account the depolarization effect, which is known to occur at high molecular density. On the other hand, we have also to consider the orientation of the EtOH molecules relative to the surface normal, that determines the perpendicular dipole of the molecule. We may tentatively suppose that EtOH molecules adsorbed in a tilted geometry in the case of the EtOH monolayer, while in the the case of the co-adsorption

they may have a more upright orientation, i.e. a larger perpendicular dipole moment.

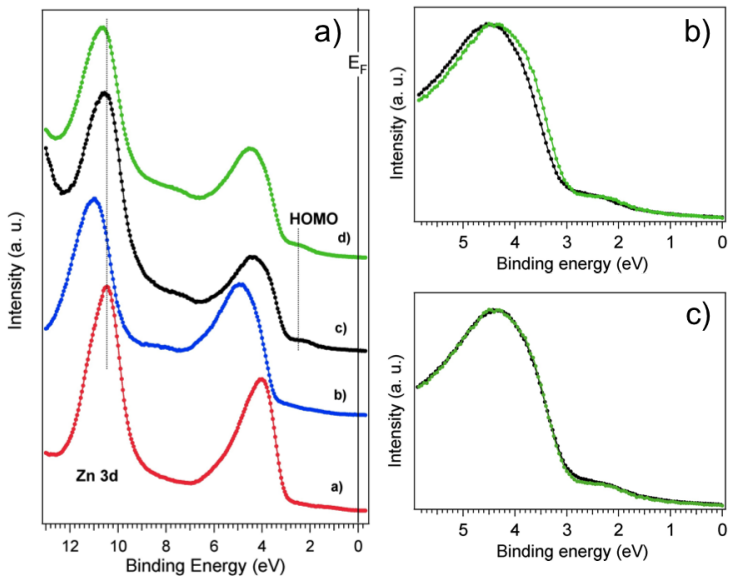

Figure 5.4.4: (a) UPS VB spectra of a) clean ZnO surface, b) EtOH/ZnO, c) 4-nitrocatechol/ZnO, d) EtOH/4-nitrocatechol/ZnO. (b) UPS low binding energy region of 4-nitrocatechol/ZnO (green dashed line) and EtOH/4-nitrocatechol/ZnO (black dashed line) and (c) UPS of EtOH/4-nitrocatechol/ZnO shift of ΔV_{bb}.

Eventually, we are interested in analyzing the effect of the co-adsorption induced band bending on the energy level alignment of the 4-nitrocatechol molecular states. In particular, we focus on the behavior of the HOMO level, which is observed at 2.3 eV binding energy on the 4-nitrocatechol/ZnO valence band spectrum of Figure 5.4.4. Upon EtOH adsorption the HOMO state shifts to higher binding energy by the same amount of band bending variation (i.e. 0.15 eV). This is evident in the right panel of Figure 5.4.4, were the low energy region of the 4-nitrocatechol and EtOH/4-nitrocatechol interfaces are shown: If the EtOH/4-nitrocatechol spectrum is shifted back by 0.15 eV, so that the valence band edge of the two spectra coincides, also the two HOMO features overlap. This means that the HOMO molecular level in the semiconductor gap shifts rigidly with the semiconductor bands, following the band bending variation.

5.5 From 4-nitrocatechol to aminocatechol

During XPS and UPS experiments on the 4-nitrocatechol/ZnO system, we noticed a gradually degradation of the 4-nitrocatechol molecule induced by UV and X-ray irradiation. A similar effect has been observed also in the case of nitrobenzene moiety adsorbed on the Si(111) surface by Roodenko and co-workers[13]. They found, analyzing the N1s core level spectrum, that the nitro group in the aromatic compound can be converted into amino species by X-ray irradiation. As shown in Figure 5.5.1 we also observe the same behavior: the N1s core level spectrum gradually modifies upon X-ray or UV irradiation, and a new feature forms at 399.8 eV, attributed to the reduction of nitro group of 4-nitrocatechol molecule into amino species.

This observation allow us to address the problem of dye degradation in DSSC by solar irradiation, which is well known to produce a decay in the power conversion efficiency. We indeed thought to investigate the changes that occur to the interface electronic properties upon dye degradation. To this aim, we follow the effect of X-ray irradiation as a function of time, checking the modifications of the XPS spectra every 25 min. Irradiation was performed using the X-ray lamp itself (Al K_α X-ray source with 240 W of emission power).

After each irradiation, XPS spectra were taken to monitor the chemical changes during the conversion of the nitro group into amino group. The N1s core level of the pristine layer is characterized by a peak centered at 405.1 eV binding energy ($N1s_2$) attributed to the Nitrogen of the nitro group. During irradiation the peak relative to the amino group ($N1s_1$at 399.8 eV) appears, and increases in intensity while the peak relative to NO_2 decreases. The O1s core level analysis confirms this trend. The O1s peak of the surface after irradiation has been fitted with two components, as for the evaporated surface. The component at 531.9 eV binding energy, related to the OH and NO_2 groups, decreases due to the chemical conversion.

In Figure 5.5.2 the C1s core level spectra corresponding to the pristine layer and to that exposed to 2 hours irradiation are compared, finding that in the latter the C1s core level line-shape shows a shoulder at high binding energy. We fitted the peak with three component: the $C1s_1$ component at 284.5 eV is relative to the aromatic Carbon, the $C1s_2$

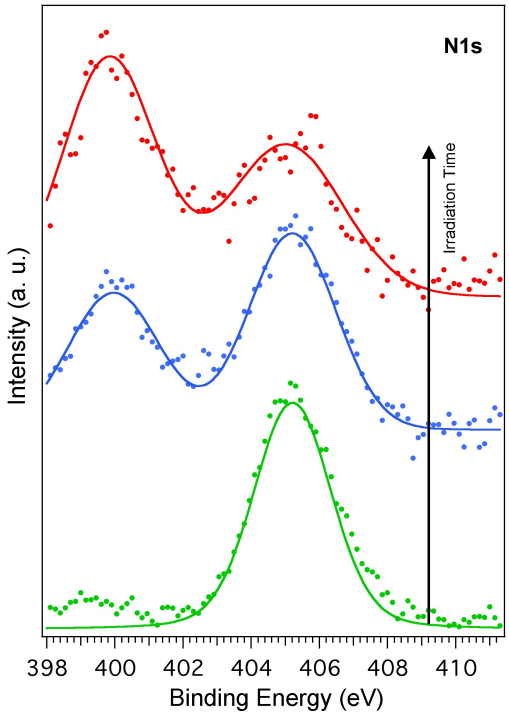

Figure 5.5.1: XPS N1s core levels spectra as function of irradiation time.

component at 285.9 eV is due to both carbon bonded to -NO_2 and to -OH, while the $C1s_3$ component relative to carbon bonded to -NH_2 is set at 287.9 eV. The fitting parameters and relative intensities are reported in Table 5.5.1.

In Figure 5.5.3 the intensities of the two $N1s_1$ and $N1s_2$ components are shown as a function of irradiation time.

While the total C1s intensity remains almost unchanged during irradiation, the overall intensity of the N1s spectra (i.e. the sum of $N1s_1$ and $N1s_2$) slightly decreases upon irradiation time. This finding suggests that irradiation also leads to cleavage of the C-N bond, possibly leaving a certain amount of adsorbed catechol molecules. Therefore three catecholate molecules are present on the surface after irradiation: catechol, 4-nitrocatechol and aminocatechol (i.e. 4-amino-1,2-benzendiol). The amount of catechol fraction as a function of irradiation time (green curve in Figure 5.5.3) can be tentatively estimated considering the difference between the pristine $N1s_1$ intensity and the sum ($N1s_1$ and $N1s_2$), as shown in Figure 5.5.3.

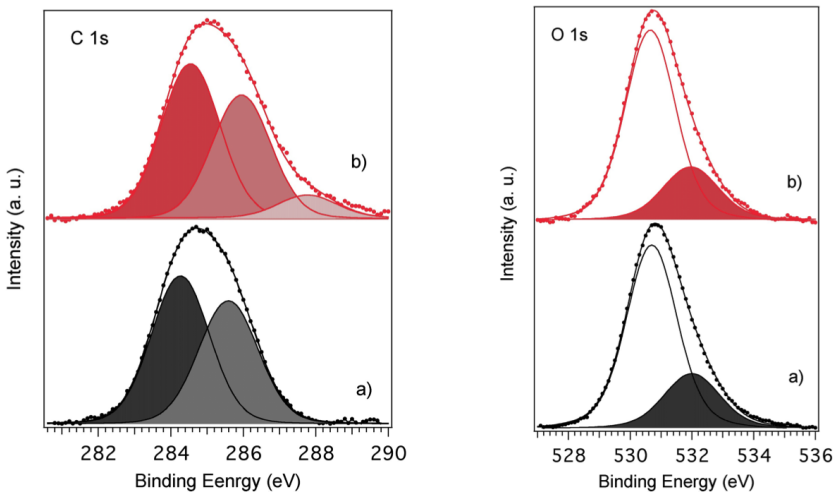

Figure 5.5.2: C1s and O1s XPS core levels spectra of 4-nitrocatechol/ZnO (a) and 4-nitrocatechol/ZnO after two hour of irradiation (b).

	B.E. (eV)	W_g	I/I_{Zn}
$N1s_1$	399.8	1.7	0.016
$N1s_2$	405.1	1.5	0.088
$C1s_1$	284.5	0.9	0.124
$C1s_2$	285.9	0.9	0.100
$C1s_3$	287.8	0.9	0.018

Table 5.5.1: Fitting parameters of C1s and N1s core level components for irradiated surface. The intensity of components has been normalized to Zn2p core level intensity.

5.5.1 Ionization energy variation

Aiming at characterizing the influence of irradiation-induced damage on the electronic properties of the interface, we measured the variation of both band bending and work function as a function of irradiation time using XPS technique. Band bending does not change upon irradiation. On the other hand, as Figure 5.5.3 shown, the work function (and therefore also the ionization energy) strongly varies, shifting by -0.75 ± 0.1 eV after 2hrs irradiation time. We ascribe this huge variation to a change in the interface dipole layer. Indeed, as previously described in paragraph 5.3.1 the 4-nitrocatechol is character-

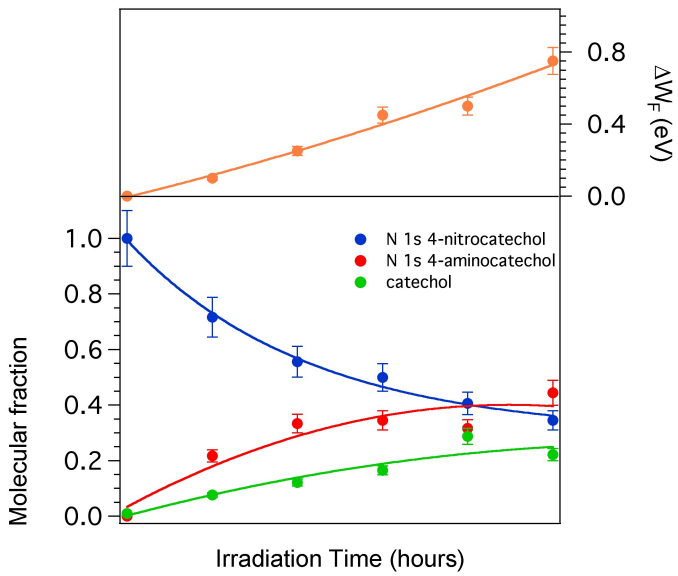

Figure 5.5.3: Top of the panel: variation of the WF measured as a function of time irradiation. Bottom of the panel: each curve represent the trend of the relative intensity of the N1s peaks for (a) 4-nitrocatechol, (b) aminocatechol and the (c) catechol in function of the irradiation time.

ized by a strong inward dipole moment; on the other hand the aminocatechol produced by NO_2 reduction is characterized by an opposite molecular dipole moment. The presence of aminocatechol moieties can therefore clearly explain the observed variation in the ionization potential. These findings nicely prove that chemical transformations which can occur to the functionalized surface upon irradiation, can significantly affect the dipole layer and thus the ionization energy of the system. This effect can have a significant influence on the efficiency of a complete DSS cell, in particular affecting V_{OC}.

5.6 Cu-Phthalocyanine on ZnO(10$\bar{1}$0)

In this last part of this chapter we present the results of our investigation on the adsorption and interfacial electronic structures of CuPc/ZnO(10$\bar{1}$0). We chose this molecule as a prototype of the phthalocyanine family, which is widely used as dye in DSSC. We are in particular interested to extend the important concepts developed in the case of catecholate interfaces and concerning the mechanisms of electronic level alignment. We investigated the molecular absorption by means of XPS measurements. In the case of phthalocyanines, the molecular growth proceeds through formation of subsequent layers, without any saturation. It is therefore necessary to estimate the film thickness, in terms of number of molecular layers, by XPS analysis. Molecular deposition has been made at constant rate, as measured with a quartz microbalance.

5.6.1 Cu-Phthalocyanine adsorption

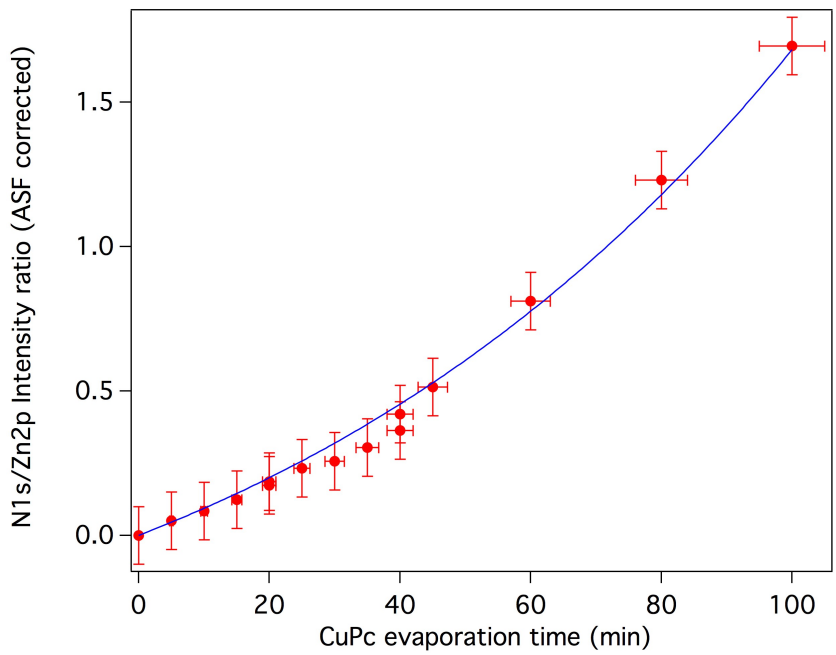

Figure 5.6.1: Intensity ratio between the N1s and Zn2p core level peak intensity as a function of evaporation time.

In Figure 5.6.1, the intensity ratio between the N1s and Zn2p core level peak intensity (ASF corrected) is reported as a function of evaporation time. To calibrate the evaporation rate the experimental data are fitted with the function (see paragraph 4.1.1.1):

$$\frac{I_N}{I_{Zn}} = \frac{n_N \lambda_N^{Pc} e^{\frac{rt}{\lambda_{Zn}^{Pc}}} (1 - e^{\frac{rt}{\lambda_N^{Pc}}})}{\lambda_{Zn}^{ZnO}} \tag{5.6.1}$$

where n_N is the number surface density of Nitrogen atoms in a monolayer, λ_N^{Pc}= 40 Å, λ_{Zn}^{Pc}= 21 Å, λ_{Zn}^{ZnO}= 11 Å are the mean free path of N1s and Zn2p photo-emitted electrons in the Pc layer and in ZnO, respectively, r is the deposition rate and t is the evaporation time. The fitting parameters provide a rough estimate of both the number surface density $n_N = \frac{1}{3}$ and the deposition rate r= $\frac{1}{25}$ ML/min. The maximum coverage achieved in the present set of measurements corresponds therefore roughly to 4 ± 1 ML. In Figure 5.6.2 XP spectra of the 4 ML C1s and N1s core levels are shown. The C1s core level peak has been fitted with three components. The first component ($C1s_a$) is set at 284.6 eV binding energy and has been attributed to carbon atoms in the benzene ring. The second component ($C1s_b$), at 286 eV, is related to carbon atoms in the pyrrole ring. The third component, at 287.9 eV binding energy has been attributed to shake-up satellites, which are due to the electronic transition from the HOMO to the LUMO of the molecule. The N1s core level peak has been fitted with two Voigt components. The main feature is set at 398.9 eV binding energy, and is due to the two non-equivalent nitrogen species in the pyrrole group, while at 400.5 eV binding energy is set the shake-up satellite associated to the intrinsic HOMO-LUMO excitation. These assignments are in agreement with literature, and in particular with previous observations on CuPc/Au(110) by Evangelista and co-workers[19].

In Figure 5.6.3 the XPS spectra of the C1s, N1s and Cu2p core levels are shown as a function of coverage. As Figure 5.6.3 shows, the $Cu2p_{2/3}$ core level peak is set at 935.7 binding energy for low coverage while for increasing coverage the peak shifts by -0.6±0.1 eV to lower binding energy.

The N1s core level peak shows the same behavior: it shifts by -0.7±0.1 eV with increasing coverage, moving from 399.3 eV to 398.6 eV. On the other hand, the C1s core level

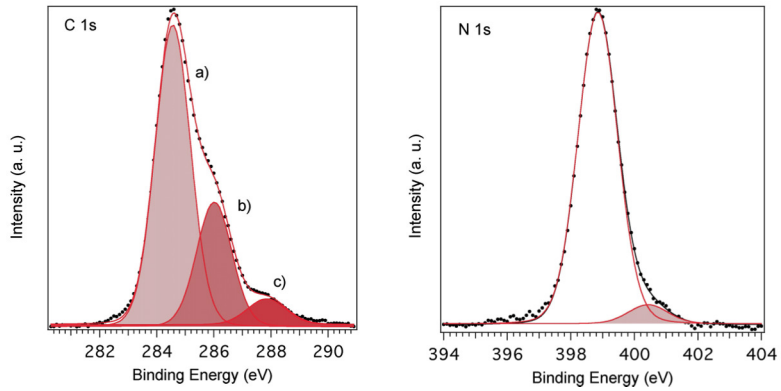

Figure 5.6.2: Left panel: C1s XPS core level peak of high coverage of CuPc/ZnO. Right panel: N1s XPS core level peak of high coverage.

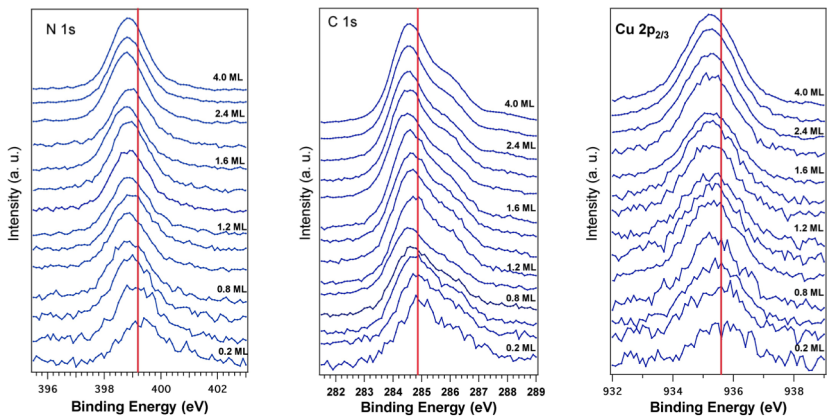

Figure 5.6.3: N1s (left), C1s (middle) and Cu2p$_{2/3}$(right) XPS core-level peaks as function of coverage.

shows a smaller shift. At low coverage the peak is set at 284.8 eV binding energy, shifting by -0.4±0.1 eV with the increase of coverage. The behavior of the core-level energies as a function of coverage is reported in Figure 5.6.4 showing that the shift to lower binding energy tend to saturate beyond 1ML.

5.6.2 CuPc/ZnO interface - electronic properties

The electronic properties of the CuPc/ZnO interface has been investigated by means of HREELS and UPS measurements. In Figure 5.6.5, the HREEL spectra of CuPc/ZnO in the electronic transition region are shown for different coverage up to 4 ML. A narrow

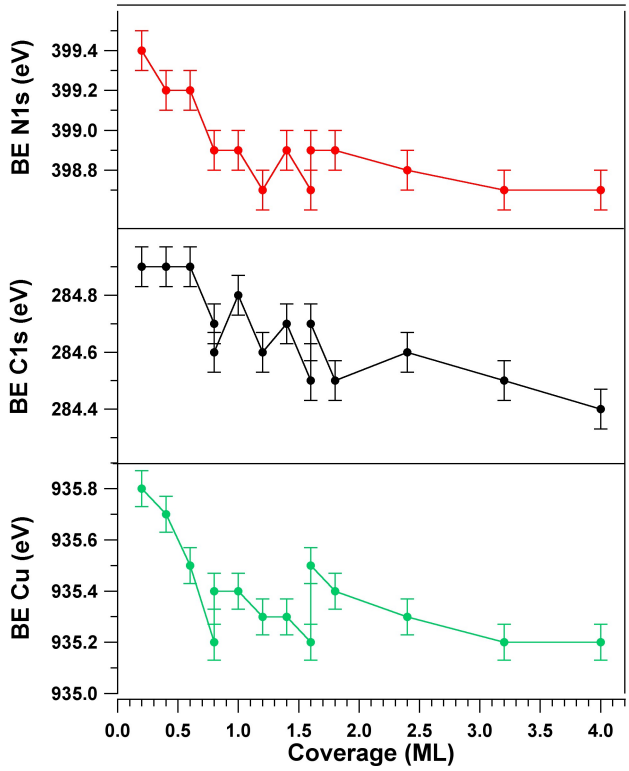

Figure 5.6.4: N1s, C1s and Cu2p$_{2/3}$core-level energies as function of coverage

peak located at 1700 meV energy loss appears already at 0.8 ML, and increases in intensity with coverage. This feature is attributed to the HOMO-LUMO transition of CuPc. Direct information on the HOMO level position can be derived by UPS valence band spectra. The valence band spectra are reported in Figure 5.6.6 for selected coverages. The main feature at 10.75 eV binding energy is the Zn3d peak: for high coverages this feature changes shape, due to the presence of molecular-related states. Another molecular-related state grows in intensity with coverage around 6.5 eV binding energy. The feature appearing at 1.4 eV binding energy for 0.8 ML coverage is attributed to the HOMO state of the molecule, in agreement with the results of Park and co-workers[21]. Its energy position remains essentially constant in the whole coverage range. Combining the value of the HOMO energy relative to the valence band edge, which can be estimated as 1.7 ± 0.1 eV, with the HOMO-LUMO distance derived by HREELS, we can conclude that the molecular LUMO lies 3.4 eV above the valence band, i.e. it is degenerate with the conduction band edge.

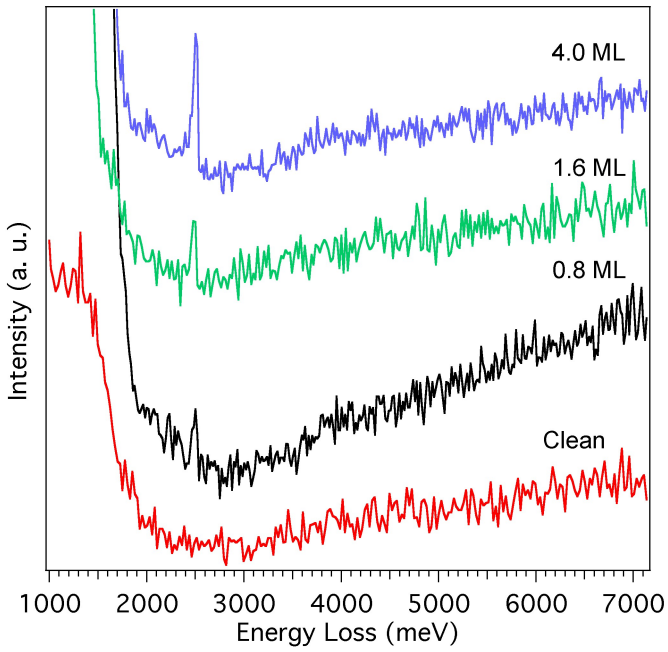

Figure 5.6.5: HREEL spectra: electron transition region for different coverage.

We here briefly discuss our results in view of those obtained by Yu. and co-workers on the similar ZnPc/TiO_2system[20]. In that case, a quite substantial core level shift (1.5-1.7 eV) was observed, while in UPS the HOMO state appeared only for coverage above 1 ML. These findings were interpreted as due to charge transfer from the molecular HOMO to the substrate which determine the quenching of the HOMO state at the monolayer. In that case, a quite substantial core level shift (1.5-1.7 eV) was observedupon molecular adsorption, while in UPS the HOMO state appeared only for coverage beyond 1ML. These findings were interpreted as due to a significant charge transfer from the molecular HOMO to the substrate, which determine the quenching of the HOMO state in the monolayer.

In our case on the contary, the presence of HOMO-related features both in UPS and HREELS data already at 0.8 ML proves that quenching does not occur (or is limited to very low coverage). This finding is also in agreement with the (0.6-0.7 eV) observed core-level shifts, which suggest a smaller amount of charge transfer in the case of ZnO relative to TiO_2. Despite the smaller value, this charge transfer significantly affects the energy alignment at the interface, inducing a remarkable shift in the ionization energy.

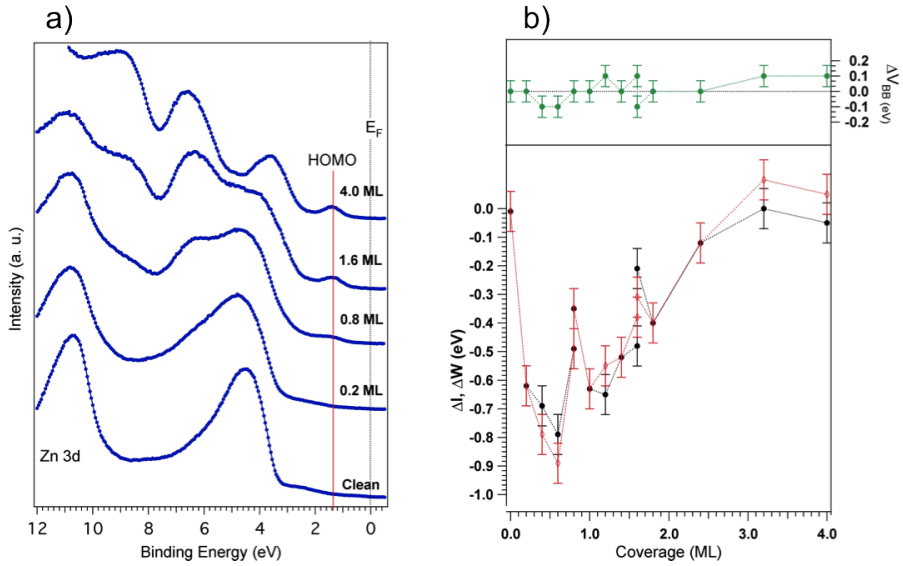

Figure 5.6.6: a) UPS valence band spectra of a) clean surface and different CuPc/ZnO coverage. b) V_{bb} variation (green dots) , W_F(red dots) and ΔI variations as a function of coverage.

Indeed, as shown in Figure 5.6.6 b), the W_F presents a minimum at around 0.5 ML. For higher coverage the W_F increases, and above 2 ML its variation almost vanishes. As the isolated molecule does not present any dipole moment, the interface dipole layer can be reasonably attributed to the charge transfer and/or polarization of the molecule towards the substrate. The sign of the ionization energy shift is indeed consistent with the direction of the molecular dipole moment induced by charge transfer. Interestingly, the minimum in ionization energy occurs between half and one monolayer: this may suggest that charge transfer mainly occurs at defects and step edges. The successive increase of the ionization energy and the vanishing of its variation for high coverage suggest that the amount of charge transfer may depend on coverage, reducing with the number of monolayers. This explanation is in general agreement with the core-level shift to lower binding energy, which saturates for coverage beyond 1 ML.

Bibliography

[1] K. Kotsis, V. Staemmler Phys. Chem. Chem. Phys. 2006, 8, 1490.

[2] Y. Wang, M. Muhler, C. Woll Phys. Chem. Chem. Phys. 2006, 8, 1521.

[3] S. G. Girol, T. Strunskus, M. Muhler, Ch. Woll J. Phys. Chem. B 2004, 108, 13736.

[4] J. M. Vohs, M. A. Barteau Surf. Sci. 1988, 201, 481.

[5] S.-C. Li, Y. Losovyj, U. Diebold Langmuir 2011, 27, 8600.

[6] S. Rangan, J-P Theisen, E. Bersch, R.A. Bartynski Appl. Surf. Sci. 2010, 256, 4829.

[7] A. Calzolari, A. Ruini, A. Catellani J. Am. Chem. Soc. 2011, 133, 5893.

[8] P. Zurcher, R. S. Bauer, J. Vac. Sci. Technol. A 1983, 1, 695.

[9] P. Giannozzi, S. Baroni, N. Bonini, M. Calandra, R. Car, C. Cavazzoni, D. Ceresoli, G. L. Chiarotti, M. Cococcioni, I. Dabo, A. Dal Corso, S. de Gironcoli, S. Fabris, G. Fratesi, R. Gebauer, U. Gerstmann, C. Gougoussis, A. Kokalj, M. Lazzeri, L. Martin-Samos, N. Marzari, F. Mauri, R. Mazzarello, S. Paolini, A. Pasquarello, L. Paulatto, C. Sbraccia, S. Scandolo, G. Sclauzero, A. P. Seitsonen, A. Smogunov, P. Umari, R. M. Wentzcovitch, J. Phys.: Condens. Matter 2009, 21, 395502. See also www.quantum-espresso.org.

[10] A. Pasquarello, M. S. Hybertsen, R. Car, Phys. Rev. B 1996, 53, 10942.

[11] A. Catellani, G. Galli, F. Gygi, Appl. Phys. Lett. 1998, 72, 1902.

[12] A. Calzolari, A. Catellani, J. Phys. Chem. C 2012, 116, 17158.

[13] K. Roodenko , M. Gensch , J. Rappich , K. Hinrichs , N. Esser , R. Hunger J. Phys. Chem. B 2007, 111, 7541.

[14] J.-P. Cornard, Rasmiwetti , J.-C. Merlin, Chem. Phys., 2005, 309, 239.

[14] E. Galoppini, Coord. Chem. ReV. 2004, 248, 1283.

[15] S. Rangan, J.-P. Theisen, E. Bersch, R.A. Bartynski Appl. Surf. Sci. 2010, 256, 4829.

[16] A. Baldereschi, S. Baroni, R. Resta, Phys. Rev. Lett. 1988, 61, 734.

[17] H. Lueth, Surface and Interfaces of Solid Materials, Springer, Verlag, Berlin.

[18] K. Ozawa, K. Mase, Phys. Rev. B 2011, 83, 125406.

[19] F. Evangelista, A. Ruocco, R. Gotter, A. Cossaro, L. Floreano, A. Morgante, F. Crispoldi, M. G. Betti, C. Mariani J. Chem. Phys. 131, 2009, 174710.

[20] S. Yu, S. Ahmadi, C. Sun, P. T. Z. Adibi, W. Chow, A. Pietzsch, M. Göthelid J. Chem. Phys. 136, 2012, 154703.

[21] S. H. Park, H. J. Kim, M-H Cho, Y. Yi, S. W. Cho, J. Yang, H. Kim Appl. Phys. Lett. 98, 2011, 082111.

Chapter 6

Conclusions

In this thesis work we studied and characterized the adsorption of few different dyes. i.e. catechol, 4-nitrocatechol and Cu-phthalocyanine on the ZnO($10\bar{1}0$) surface. The investigated systems can be considered as simple models of dye/metal-oxide interfaces and were studied combining several electronic spectroscopies, i.e. UPS, XPS and HREELS. The modification of the interface properties upon co-evaporation of ethanol and 4-nitrocatechol was also analyzed. Moreover we have investigated the changes in the electronic properties occurring at the 4-nitrocatechol/ZnO interface during x-ray and UV irradiation.

Initially, the investigation addressed the characterization of the catechol/ZnO interface. In agreement with previous works performed on different ZnO and TiO_2 surfaces and with theoretical calculations, UPS measurements found that the molecular HOMO lie within the semiconductor energy gap, at 0.7 eV from the valence band edge. Catechol/ZnO($10\bar{1}0$) represents therefore a type-II interface: in this type of interfaces direct injection from the molecular HOMO to the semiconductor conduction band can be envisaged, thus explaining the observed sensitizing effect induced on ZnO by molecular adsorption. Catechol adsorption has been also found to modify both band bending and the interface ionization energy. The variation of the ionization energy is associated to the formation of an interface dipole layer, though the presence of unwanted co-adsorbed water partially hinders a complete

analysis of its origin.

4-Nitrocatechol is characterized by a large molecular dipole moment, which makes it a promising candidate to probe the effects of molecular adsorption on the interface vacuum level position. Moreover, the presence of co-evaporating water can be strongly reduced in this case, leading to the formation of a more controlled interface relative to catechol. Strict collaboration with the theoretical group of A. Calzolari and co-workers allowed us to gain a comprehensive picture of the electronic properties and energy level alignment of the 4-nitrocatechol/ZnO interface, comparing the results of different electronic spectroscopies with those of DFT calculations[1].

Combining UPS and HREELS data we determined the energy position, relative to the semiconductor bands, of both filled (HOMO and HOMO-1) and empty (LUMO and LUMO+1) molecular states. These data resulted in agreement with DFT predictions and demonstrated the type-II character of this interface.

Band bending and work function measurements were performed as a function of 4-nitrocatechol coverage. From these quantities, the variation of the ionization energy was determined, finding a quite impressive value of ΔI=1.3 eV. In agreement with theoretical calculations, we concluded that the associated interface dipole layer is due to the strong inward dipole moment of the adsorbed molecule. Moreover, combining UPS information on the molecular filled state with HREELS data, we obtain the energy position of the conduction band edge. We were thus able to conclude that the interface dipole layer influences in the same way both ionization energy and electron affinity of the system, leading to a rigid shift of both valence and conduction bands. In other terms, no significant density of states around CB_{min} is induced by molecular adsorption. The electron affinity variation is relevant as it could determine, in a complete DSSC cell, a significant change in V_{OC}.

Furthermore, our results showed how co-evaporating two molecule with opposite dipole moment, like ethanol and 4-nitrocatechol, enable us to significantly modify the interfacial energetics of the system, affecting both its band bending and ionization energy. Moreover, we proved that a variation in band bending directly affects the molecular gap states energy,

i.e that molecular states moves rigidly together with the semiconductor bands.

During our investigations we observed that, exposing 4-nitrocatechol/ZnO system to X-ray and/or UV irradiation, it was possible to induce a chemical modification of the adlayer, reducing the nitro group of the 4-nitrocatechol to an amino group. The new molecule, aminocatechol, remained bound to the surface and is characterized by a dipole moment opposite to that 4-nitrocatechol. This chemical modification determined a significant variation of the interface dipole layer, which in turn corresponded to a strong decrease of the ionization energy. These findings nicely prove that chemical transformations which may occur to the functionalized surface upon irradiation, can significantly affect the dipole layer and thus the ionization potential of the system. This effect can have a significant influence on the efficiency of a complete DSS cell, in particular affecting V_{OC}.

In the last part of this work we investigated the adsorption of a more complex dye, Cu-phthalocyanine, on the ZnO($10\bar{1}0$) surface. XPS core level analysis provided indication that charge transfer from the molecule towards the substrate took place for submonolayer coverages. The amount of charge transfer appeared smaller than that occurring at the similar ZnPc/TiO_2 interface[2]. UPS measurements pointed out a pronounced decrease of ionization energy for submonolayer coverages, while above one monolayer this variation tends to vanish. This behavior can be related to the charge transfer occurring at the interface, suggesting that it may prevalently occur at surface defects and terrace edges.

Bibliography

[1] G. F. Arnaud, V. De Renzi, U. del Pennino, V. Corradini, R. Biagi, A. Calzolari, A. Ruini, A. Catellani J.Phys. Chem C *submitted*

[2] S. Yu, S. Ahmadi, C. Sun, P. T. Z. Adibi, W. Chow, A. Pietzsch, M. Göthelid J. Chem. Phys. 136, 2012, 154703.

Appendix A

In this work we investigated the different pathways through which N-allylurea molecules bind to Si(111)-7x7 surface, performing a UHV reaction. I acquired, analyzed and interpreted both XPS and HREELS spectra. In particular, I became acquainted with the fitting procedures of XPS core-level peaks, and with the interpretation of core-level components in XPS spectra of adsorbed organic moieties. These skills have been extremely important for the analysis and interpretation of the results obtained during the thesis work.

THE JOURNAL OF PHYSICAL CHEMISTRY C

Article

pubs.acs.org/JPCC

Competing Pathways in *N*-Allylurea Adsorption on Si(111)-(7 × 7)

Valentina De Renzi, Gaëlle F. Arnaud,* and Umberto del Pennino

Dipartimento di Fisica, Università di Modena e Reggio Emilia, via Campi 213/A, 41125, Modena, Italy, and CNR Institute of Nanoscience, S3 Center, via Campi 213/A, 41125, Modena, Italy

ABSTRACT: Functionalization of silicon surfaces with *N*-allylurea ($CH_2{=}CH{-}CNH{-}CO{-}NH_2$) represents a valuable strategy to obtain covalently bonded Si−C interfaces with amino and/or carbonyl termination. In this work, we studied *N*-allylurea adsorption on the Si(111)-(7 × 7) surface by combining X-ray and ultraviolet photoemission spectroscopy (XPS and UPS) with high resolution energy loss spectroscopy (HREELS) measurements. XPS core level analysis provides information on the molecular attachment process. Si−C covalent bonding is evidenced by the presence of a C 1s component at 284.8 eV, while interaction through N−Si bonding is proved by the presence of a N 1s component at 397.8 eV. Three different adsorption mechanisms are envisaged: (I) [2 + 2]-like cycloaddition occurring at the rest atom−adatom dimer through cleavage of the vinyl group, (II) Si−N bonding at adatom sites upon cleavage of NH_2 and rearrangement of the ureic group to form an imidol species (−N═C−OH), with release of a H atom, and (III) hydrosilylation at adatom sites, through cleavage of the vinyl group and involvement of H atoms provided by reaction II.

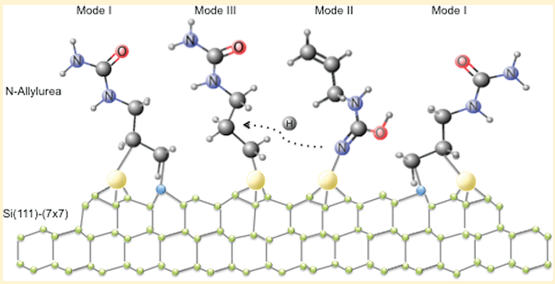

1. INTRODUCTION

Organic functionalization of silicon surfaces represents an extremely promising route for the development of silicon-based molecular devices.[1] Fabrication of hybrid organic/silicon systems with tunable properties requires the controlled and selective attachment of multifunctional compounds to silicon surfaces. Clean silicon surfaces are extremely reactive, meaning that multiple surface reaction pathways are possible even for seemingly simple molecules. Indeed, individuation of the reaction pathways leading to the required surface termination is by no means trivial. A complete understanding of the reactivity and selectivity of organic multifunctionalities with silicon surfaces is therefore of paramount importance and has been recently the object of extensive investigations.[2,3] In particular, the Si(111)-(7 × 7) surface, described by the dimer−adatom−stacking fault (DAS) model,[4] is characterized by multiple reaction sites with distinct reactivity and structural properties. It is therefore expected to display a diversity of reaction mechanisms for different organic molecules and can be considered as a model system to explore more complex situations.

Silicon functionalization with urea-like compounds is particularly interesting due to the presence of amino and carbonyl groups, which could act as end groups for further functionalization. Moreover, urea ability to form lateral intermolecular hydrogen bonds could be exploited to obtain stable and ordered adlayers. In the case of *N*-allylurea, the presence of the vinyl group should in principle allow a simple attachment strategy on silicon surfaces, with formation of covalent Si−C bonds through a [2 + 2]-like cycloaddition or through hydrosilylation.[5,6] Both attachment strategies guarantee the availability of the amine and/or the carbonyl as terminal groups. On the (7 × 7) surface, a cycloaddition-like mechanism, where cleavage of the C═C bond is followed by the formation of two Si−C bonds at neighboring rest atom−adatom sites, has been observed for instance for ethylene adsorption[7−9] and proposed also in the case of *N*,*N*-dimethylallylamine,[10] cyclohexene,[11] and *N*-methylpyrrole.[12] On the other hand, the hydrosilylation mechanism typically takes place at hydrogenated surfaces.[13−15] Indeed, for hydrosilylation to take place on the Si(111)-(7 × 7) surface, a proper amount of hydrogen atoms, possibly derived from other concomitant reactions, is required.

Besides vinyl-based attachment, the interaction of Si(111)-(7 × 7) surface with the urea functional groups (i.e., the two amines and the carbonyl) could also be envisaged. Reaction of amines with silicon surfaces, through cleavage of NH bonds and formation of Si−N bond, has been reported for instance in the case of *N*-methylallylamine[10] and of glycine and cysteine on Si(111)-(7 × 7).[16] Such reaction has also been proposed in the case of UV-assisted allylamine deposition on the Si(111):H surface.[17] Moreover, also the C═O group could interact with the Si surface in different ways. In the case of ethyl vinyl ketone adsorption on the Si(111)-(7 × 7) surface, through cleavage of the C═O double bond and formation of Si−O and Si−C bond in a [4 + 2]-like cycloaddition reaction, has been reported.[18] Finally, also the formation of a dative bond between oxygen and Si adatoms could in principle occur.[18,19]

Received: October 28, 2011
Revised: February 6, 2012
Published: February 8, 2012

 © 2012 American Chemical Society

In this work, we studied *N*-allylurea ($CH_2{=}CH{-}CNH{-}CO{-}NH_2$) adsorption on the Si(111)-(7 × 7) surface by means of combined X-ray photoelectron spectroscopy (XPS), ultraviolet photoelectron spectroscopy (UPS), and high resolution electron energy loss spectroscopy (HREELS) measurements and demonstrated that actually different adsorption mechanisms take place at this interface, competing with and mutually influencing each other. A quantitative estimate of the occurrence of the different reaction routes has been derived by careful analysis of XPS core level data. For the sake of comparison, *N*-allylurea adsorption on the Au(111) clean surface has also been studied. The paper is organized as follows: After a description of the experimental details in section 2, in section 3 XPS, HREELS, and UPS measurements are reported and analyzed. These results are further discussed in section 4, and some conclusions are drawn in section 5.

2. EXPERIMENTAL METHODS

All measurements were performed in an UHV chamber with a base pressure of 5×10^{-10} mbar. The Si(111) wafers were cleaned through cycles in organic solvent, preoxidized in a hot $H_2SO_4 + H_2O_2$ (1:1) mixture, followed by etching in a NH_4F 40% water solution for 10 min to obtain a hydrogenated Si(111) surface.[20,21] In order to remove traces of fluorine, the samples were washed with Milli-Q water and CH_2Cl_2. The (7 × 7) reconstruction was obtained by flashing the hydrogenated surface at 970 K in UHV. The Au(111) single crystal was cleaned by usual sputtering−annealing cycles at 700 K. Sample cleanliness and order were checked by XPS and low energy electron diffraction (LEED).

N-Allylurea was evaporated in UHV by means of a resistively heated glass vial, mounted on a differentially pumped stage, normally separated from the experimental UHV chamber by a gate valve which was opened only during deposition. The sublimation temperature was controlled by a thermocouple embedded in the vial and molecular deposition was performed at 330 K. Under these conditions, the pressure in the experimental chamber raised to a few 10^{-8} mbar, while that in the evaporation stage was typically 3×10^{-6} mbar. Molecular deposition was performed keeping the sample at room temperature, and saturation coverage was obtained after 5 min exposure.

The adsorption of *N*-allylurea on the Si(111)-(7 × 7) and Au(111) surfaces was studied by means of XPS, UPS, and HREELS. XPS and UPS were performed with an unmonochromatized Mg K_α source ($h\nu_{Mg\,K\alpha}$ = 1253.6 eV) and a He discharge lamp ($h\nu_{He-I}$ = 21.2 eV), respectively. Electron energy distribution curves were measured by a hemispherical analyzer (Omicron EA125) with an overall energy resolution of 1.0 eV (0.1 eV for UPS). HREELS measurements were performed in specular conditions ($\theta_i = \theta_o = 55°$) with primary beam energy of 7.7 eV. The spectrometer (LK ELS5000) ensured an energy resolution better than 4 meV (32 cm^{-1}), as checked on Au(111) samples. On silicon surfaces instead, the energy resolution was limited to 7 meV (56 cm^{-1}) due to the quasi-elastic contributions of the substrate free carriers to the width of all spectral features.[22]

3. RESULTS

The adsorption processes occurring at the Si(111)-(7 × 7) surface are quite complex, involving different reaction pathways and molecule−surface interactions. In order to gain a clear picture of the undergoing processes, information derived by different spectroscopic tools should be combined. In the following, the results of XPS, HREELS, and UPS investigations are reported and analyzed. Moreover, XPS and HREELS data obtained from *N*-allylurea deposited on Au(111) are also presented, providing an important reference for analysis and discussion.

3.1. XPS. Relevant information on the substrate/molecule interactions and adsorption mechanisms was obtained by a detailed analysis of C 1s, O 1s, and N 1s XPS core level peaks. After Shirley background subtraction, core level line shapes were fitted by Voigt multiplets with fixed Lorentzian width. The values of the main fitting parameters are reported in Table 1.

Table 1. XPS Analysis

	Au(111)			Si(111)-(7 × 7)		
	E (eV)	fwhm (eV)	fractional area (%)	*E* (eV)	fwhm (eV)	fractional area (%)
C 1s						
A				284.8	1.6	31.5
B	284.4	1.5	49.8	285.7	1.2	18.2
C	285.8	1.5	24.6	286.6	1.7	31.8
D	288.3	2.2	25.6	289.1	1.5	18.5
A + B			49.8			49.7
C + D			50.2			50.3
(C − D)			1.0			13.3
A/B						1.73
O 1s						
E	531.4	2.2		531.8	1.7	74
F				533.2	1.8	26
N 1s						
G	399.7	1.4		399.8	2.0	88.4
H				397.8	1.2	11.6

The Gaussian widths were left free to vary and assumed different values for different components (see Table 1). Indeed, this was necessary to obtain satisfying fits without arbitrarily increasing the number of components. This procedure is justified considering that, beyond experimental broadening (which is obviously constant), possible heterogeneity in the molecular adsorption details (i.e., different adsorption sites, presence of defects, intermolecular interactions) could influence the energy value of the core-level peak (through both initial and final state effects), thus determining a variable *effective* broadening for each component.

In Figure 1, the C 1s core-level line shapes of *N*-allylurea/Au(111) (curve a), clean Si(111)-(7 × 7) (curve b), and *N*-allylurea/Si(111)-(7 × 7) (curves c and d) are reported and compared. On the clean silicon surface, a small peak located at 283 eV is observed, which is attributed to a small amount of contaminating carbon atoms bonded to Si. This component is present also in the *N*-allylurea/Si(111)-(7 × 7) curve c with essentially unchanged intensity, proving that no further contamination occurs upon *N*-allylurea deposition. Therefore, for sake of simplicity in the discussion, we subtracted this small peak from curve c, as shown in curve d, and we do not further consider it in data analysis. For both *N*-allylurea/Au(111) (curve a) and *N*-allylurea/Si(111)-(7 × 7) (curve d) interfaces, the C 1s core level line-shapes display a broad main feature, sided by a smaller peak at higher binding energy. In the case of *N*-allylurea/Au(111) the main peak, which clearly appears skewed on the high-energy side, was fitted by two components,

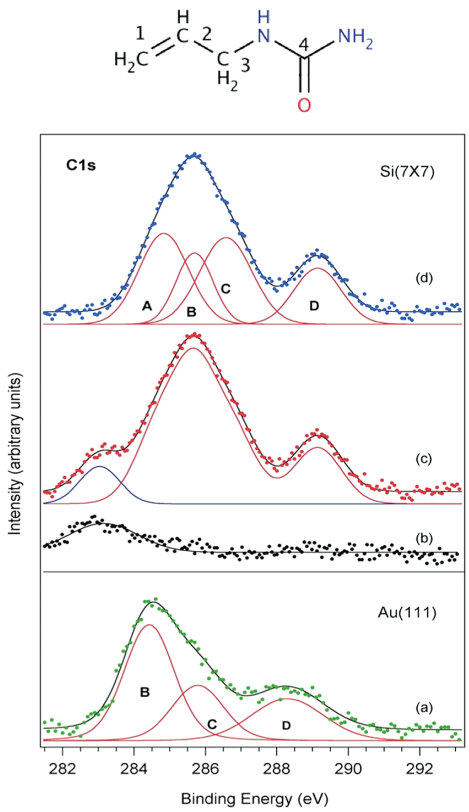

Figure 1. C 1s XPS spectra (filled circles) of *N*-allylurea adsorbed on the Au(111) surface (a); clean Si(111)-(7 × 7) surface (b); of *N*-allylurea chemisorbed on Si(111)-(7 × 7) (c); *N*-allylurea chemisorbed on Si(111)-(7 × 7), after subtraction of the contribution (blue curve solid line in panel c) of the small contaminant carbon component at 283 eV (d) (see text for details). For each spectrum, the fitting curves and multiplet components are also shown as solid lines (see Table 1 for detail of the fitting parameters). On top: *N*-allylurea molecule: the four C atom labeling is also indicated.

located respectively at 284.4 (B) and 285.8 eV (C). A further component (D), located at 288.3 eV reproduced the high-energy side peak. By comparison with the literature we attribute the B component to both C1 and C2 atoms in the vinyl group,[23,24] the C component to the C3 atom to the secondary amine, and the D component to the C4 atom in the carbonyl group[25−28] (see the molecule sketch in Figure 1, top panel).

In the case of *N*-allylurea/Si(111) the main feature of the C 1s spectrum has a more triangular and symmetric shape. Indeed, it was not possible to obtain a satisfying agreement with the experimental data by fitting the main peak of curve d with only two components, as in the case of the *N*-allylurea/Au(111). Therefore, we were forced to introduce a further component, on the low-energy side of the curve. The four components needed to fit the whole C 1s line shape are located respectively at 284.8 eV (peak A), 285.7 eV (peak B), 286.6 eV (peak C), and 289.1 eV (peak D).

Following the assignment of the *N*-allylurea/Au(111) C 1s components in curve a, we can attribute peak B to carbon in the vinyl group (C1 and C2) not interacting with silicon,[10,18] and peaks C and D to the carbon atoms bonded to nitrogen (C3)[10,16] and to oxygen (C4), respectively. We note that components B, C, and D on Si(111) are shifted to higher binding energies with respect to those on Au(111) (0.8 eV for C and D, 1.4 for B). This shift can be mainly ascribed to final state effects, i.e. different screening of the core hole by the substrate electron density. On the other hand, initial state effects, and in particular variation of core-level energies due to different interaction between the molecular functional groups and the surface, could also play a role and explain the different shift of component B, relative to C and D.

The new component observed in the case of *N*-allylurea/Si(111)-(7 × 7) (peak A at 284.8 eV in curve d) is shifted by −0.9 eV relative to peak B and is attributed, in agreement with the literature,[10,14,29] to carbon atoms (C1 and/or C2) directly bonded to silicon. The presence of this component clearly indicates that Si−C bond formation occurs for a fraction of adsorbed molecules via dissociation of the vinyl group.

The relative weight of the different components of C 1s line shapes are reported in Table 1 and provides further information on the details of *N*-allylurea adsorption on Si(111). In the case of *N*-allylurea/Au(111), molecular stoichiometry predicts that two carbon atoms (C1 and C2) over four contribute to component B, while C3 carbon contributes to component C and C4 to D. We expect therefore that (i) $A_B = (A_C + A_D) = 50\%\ A_{tot}$ and (ii) $A_C = A_D = 25\%A_{tot}$, where A_X indicates the area of component X and A_{tot} the total C 1s area. These conditions are indeed fulfilled with a discrepancy of less than 4% (see Table 1).

In the case of *N*-allylurea/Si(111), C1 and C2 atoms contribute to both A and B components, so that relation (i) in this case reads as $(A_A + A_B) = (A_C + A_D) = 50\%A_{tot}$. This condition is fulfilled within a 4% discrepancy also for *N*-allylurea/Si(111)-(7 × 7). Rather interestingly, condition (ii) instead is not respected, as peak D is definitely smaller than peak C. In particular, peak D is only 74% of its stoichiometric value, while peak C is 127% of it. Comparison with the case of *N*-allylurea/Au(111), for which $A_C = A_D$ within 4%, clearly demonstrates that the observed deviation from the expected stoichiometric relation is indeed significant. The reduction in weight with respect to the ideal value of peak D (−26%) matches almost perfectly with the increase of peak C (+27%). This fact can be explained assuming that for a fraction of adsorbed molecules, the component associated with C4 is shifted to lower binding energy, becoming partially degenerate with peak C. The fraction of molecules involved in this process can be estimated from the ratio $(A_C - A_D)/(A_C + A_D)$ as 27%. The exact value of the energy shift of this fraction could not be determined, as the introduction of a further fitting component is not sensible given the limited XPS resolution. Nevertheless, it could be estimated as roughly 2 eV, taking into account the energy position and the width of the C and D components. A similar energy downshift has been attributed in the literature to a reduction in bond order of the carbonyl species. In particular, a shift of −2.2 eV has been reported in the case of ethyl vinyl ketone adsorption on Si(111)-(7 × 7), where a [4 + 2]-like cycloaddition involving both C═C and C═O groups was proposed.[18] In that case, the binding energy downshift of the carbonyl species was interpreted as an initial state effect, induced by the lower electron-withdrawing character of oxygen in the C−O single bond relative to the C═O double bond.

Further information on the chemical state of the CO group and its interaction with the surface comes from the analysis of the O 1s core level. The O 1s line shapes of *N*-allylurea adsorbed on Au(111) and on Si(111)-(7 × 7) are shown in

Figure 2 as curves a and b, along with their best fit curves. Curve a shows a symmetric peak, located at 531.4 eV, while

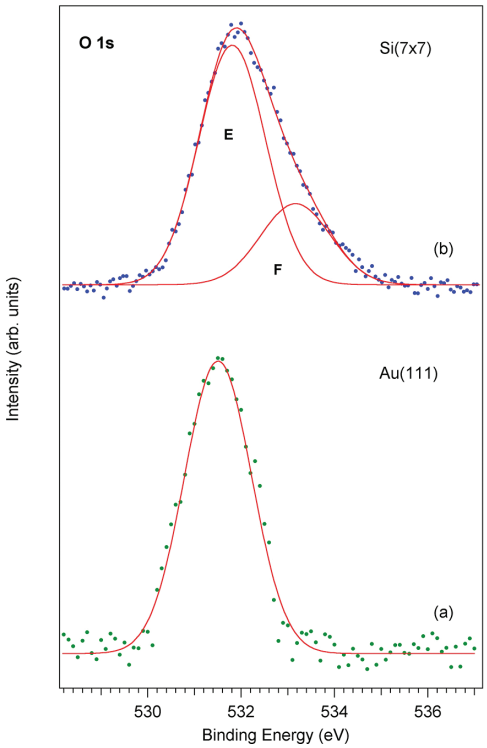

Figure 2. O 1s XPS spectra (filled circles) of *N*-allylurea/Au(111) (a) and *N*-allylurea/Si(111)-(7 × 7) (b) (filled circles). For each spectrum, the fitting curves and multiplet components are also shown as solid lines (see Table 1 for detail of the fitting parameters).

curve b is clearly skewed on the high binding energy side. It was fitted therefore with two components, located at 531.8 eV (E) and 533.2 eV (F), respectively. The intensity of the high-energy component F corresponds to 26% of the whole peak. According to the literature, binding of oxygen to Si upon cleavage of the C═O double bond leads to a slight shift to lower binding energies (∼ −0.4 eV) of the O 1s peak.[18] The high-energy component F therefore cannot be ascribed to covalent bonding of oxygen with the surface. On the other hand, though oxygen dative bonding would explain the energy position of component F,[18] it would not fit with the indication of C═O bond order reduction derived by C 1s line shape analysis, and can be excluded consequently. We therefore tentatively attribute component F to the formation of C−OH species.[30,31] This hypothesis, which is in agreement with C 1s analysis, is also supported by HREELS data, as it will be discussed in section 3.2. Moreover, the possible origin of H atoms required to form the C−OH species is figured out by the analysis of the N 1s core level line shape, as discussed in the following.

The N 1s core levels of *N*-allylurea/Au(111) and *N*-allylurea/Si(111) are reported in Figure 3 as curves a and b, respectively. The main peak (G) is located at 399.8 eV binding energy in curve b (399.7 eV in curve a), which is a typical value for amine nitrogen.[10,16] In the *N*-allylurea/Si(111) curve the shoulder observed at 397.8 eV binding energy, hereafter labeled

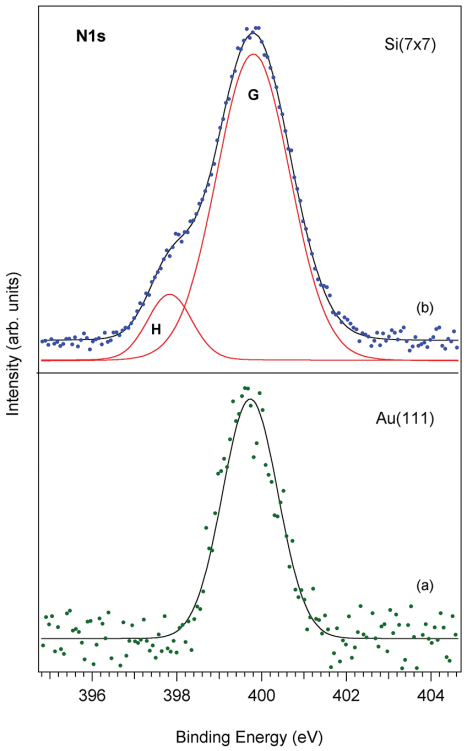

Figure 3. N 1s XPS spectra (filled circles) of *N*-allylurea on Au(111) (a) and Si(111)-(7 × 7) (b). For each spectrum, the fitting curves and multiplet components are also shown as solid lines (see Table 1 for detail of the fitting parameters).

as H, is indicative of the formation of a covalent bond between the terminal primary amine and silicon surface atoms,[32] while dative bonding could be excluded as it would require binding energies higher than 400 eV.[33,34]

Si−N covalent bonding implies cleavage of NH bond and release of hydrogen atoms, thus providing a source for the proposed oxygen protonation. The fraction of molecules interacting with the surface through nitrogen can be estimated from the intensity ratio between the low (H) and high (G) binding energy components of the N 1s peak as $2A_H/(A_G + A_H) = 23\%$ and fits remarkably well with the fraction of molecules involved in oxygen protonation.

The binding energy of component H (397.8 eV) corresponds to a downshift of −2.0 eV relative to the unreacted amine. In fact, Si−NH bond formation (with single bond cleavage) typically corresponds to a N 1s binding energy downshift of −1.5 eV,[10,33,35] while larger downshifts are attributed in the literature to double bond cleavage, as for instance in the case of acetonitrile adsorption on the Si(111)-(7 × 7) surface, where the −N═C group bonds to a Si adatom.[36] Our data therefore indicate that bonding through nitrogen occurs upon cleavage of both NH bonds at the terminal amine and formation of a Si−N═C− bonding.

We now itemize the relevant pieces of information provided by N 1s, C 1s, and O 1s line shape analysis as follows: (i) the relative intensity of peaks C and D is interpreted as due to a fraction (27%) of molecules in which bond order reduction of the C═O group occurs; (ii) component F of O 1s core level

indicates that 26% of the total amount of oxygen is protonated; (iii) almost the same fraction of molecules (23%) experiences Si−N═C− bonding, with release of two hydrogen atoms per molecule.

These findings can be nicely put together to conclude that roughly one-fourth of all molecules adsorbs through Si−N bonding, with a concomitant rearrangement of the ureic group to form an imidol species (−N═C−OH). Indeed, the proposed protonation of oxygen can take place thanks to the releasing of amine hydrogen atoms. This rearrangement, implying a C═O bond reduction, is consistent with the observed downshift of the carbonyl component in the C 1s core level manifold.[37]

In summary, XPS analysis clearly shows that (1) a fraction of molecules interacts with the Si surface forming Si−C bond, as evidenced by the presence of component A at 284.6 eV in the C 1s line shape and (2) roughly one-fourth of all adsorbed molecules interacts with the surface through Si−N bonding, forming an imidol species and releasing one further hydrogen atom per molecule. The quantitative evaluation of the amount of molecules involved in Si−C bonding and the influence of hydrogen release on surface reaction pathways will be discussed in detail in section 4, after presentation of the HREELS and UPS data.

3.2. HREELS. HREELS spectra of *N*-allylurea/Au(111) and *N*-allylurea/Si(111) are shown in Figure 4, as curves a and b,

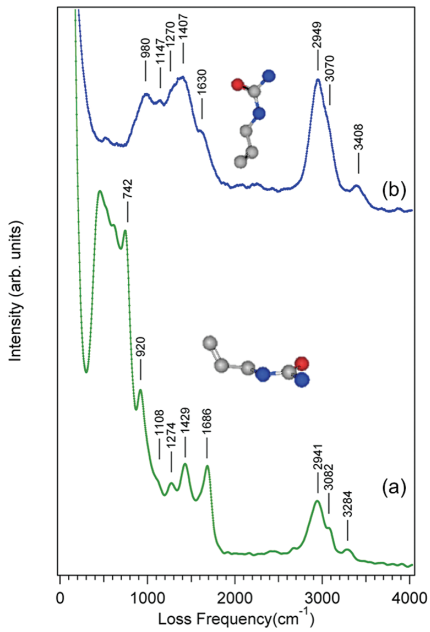

Figure 4. HREELS spectra of *N*-allylurea/Au(111) (a) and *N*-allylurea/Si(111)-(7 × 7) (b). A qualitative sketch of the different molecular orientation on the two surfaces is also shown.

respectively. The high-energy resolution (32 cm^{-1}) achievable at metal surfaces eases a clear attribution of the vibrational feature of the *N*-allylurea/Au spectrum, based on comparison with IR data of bulk *N*-allylurea[38,39] and HREELS data of similar adsorbed species,[10,18] as reported in Table 2. On the other hand, the lower energy resolution of HREELS on silicon (56 cm^{-1}) makes difficult a clear separation of all vibrational

Table 2. HREELS Vibrational Assignment

vibrational assignment[a]	*N*-allylurea/Au(111)	*N*-allylurea/Si(111)-(7 × 7)	*N*-allylurea IR[b]
−NH−, −NH_2 str/−OH str		3408	3440
−NH−, −NH_2 str	3284		3335
CHR═CH_2 str	3082	3070	3015
CH_3−CH_2 str	2941	2949	2984
NHC(O)NH_2/NHC(N)OH		1630	
NHC(O)NH_2	1686		1666
−CH_2−, CHR═CH_2 def i.p.	1429	1407	1421
−NH− comb. C−N def	1274	1270	1260
C−C═ def[c]	1108	1147	1017
CHR═CH_2 def o.o.p.	920	980	989
			928
−NH−, −NH_2 def o.o.p.[d]	742		

[a]Cross, A. D. *An Introduction to Practical Infrared Spectroscopy*; Butterworths: London, 1964. [b]http://webbook.nist.gov/chemistry. [c]Tang, H. H.; Cai, H. Y.; Ning, Y. S.; Lai, Y. H.; Xu, G. Q. *Surf. Sci.* **2007**, *601*, 3293. [d]Huang, J. Y.; Tang, H. H.; Shao, Y. X.; Liu, Q. P.; Alshahateet, S. F.; Sun, Y. M.; Xu, G. Q. *J. Phys. Chem. C* **2007**, *111*, 6732.

modes, especially in the fingerprint region. Comparison between the two spectra is therefore extremely useful and allows a thorough analysis of *N*-allylurea/Si(111) spectrum, as summarized in Table 2.

The highest intensity modes in the *N*-allylurea/Au(111) spectrum are observed in the region below 1000 cm^{-1} and can be attributed to a band of out-of-plane molecular bending modes. In particular, the peak at 742 cm^{-1} is attributed to the NH out-of-plane deformation, while the peak at 920 cm^{-1} is due to ═CH_2 out of plane deformation.[10,17,18] As the spectra are taken in dipole-scattering conditions, the higher intensity of these out-of-plane modes relative to the corresponding in-plane modes is a clear indication that *N*-allylurea adsorbs in an almost flat geometry, as qualitatively sketched in Figure 4a.[40] The region above 1000 cm^{-1} is characterized by three main features, at 1274, 1429, and 1686 cm^{-1}, attributed to in-plane deformations of the −NH and −CH_2 groups and to the ureic-group stretching mode, respectively. The stretching region around 3000 cm^{-1} is instead characterized by a main peak at 2941 cm^{-1}, attributed to the −CH_2 stretching mode, a peak at 3082 related to the ═CH_2 stretching, and another quite sharp peak at 3284 cm^{-1}, attributed to the NH stretching of both amines.[10,38,41,42]

Comparison between *N*-allylurea/Si(111) and *N*-allylurea/Au(111) spectra in Figure 4 immediately shows that the adsorption geometry on the two surfaces is quite different: in the Si spectrum (curve b) the out-of-plane modes locates below 1000 cm^{-1} are substantially suppressed, clearly indicating a more standing-up configuration, as qualitatively sketched in the same figure.

We note that, in principle, the HREELS region below 1000 cm^{-1} could provide important indication on molecule−substrate interactions from direct observation of Si−X stretching and bending modes, where X stands for the molecular atom directly bonded to the surface, i.e. C, N, or O. However, there is no general and clear consensus in the literature on the exact frequency of Si−C and Si−N stretching modes, as typical

reported frequencies spans from 500 to 800 cm^{-1} for both species.[11,13,17,35,41−43] In our case, the absence of intense features in this frequency range and the possible contribution of out-of-plane molecular modes (see the *N*-allylurea/Au(111) spectrum) hinder a clear identification of substrate−adsorbate modes. We therefore do not try to identify them in the experimental HREELS spectrum.

Important information on the adsorption mechanisms can be instead derived by inspection of the stretching region around 3000 cm^{-1}, where the presence of both $-CH_2$ and $=CH_2$ modes at 2949 and 3070 cm^{-1} is clearly observed. The presence of the 3070 cm^{-1} mode, seen as a clear shoulder of the main peak, shows that molecules with intact vinyl groups are present on the surface. This is confirmed also by the peak centered at 980 cm^{-1}, related to the $=CH_2$ and $=CH$ out-of-plane deformations. Actually, this peak appears shifted relative to the corresponding peak observed in *N*-allylurea/Au(111) spectrum (920 cm^{-1}), probably because of different weight in the intensity of $=CH_2$ and $=CH$ modes.[39] Though HREELS does not provide a quantitative estimate of the amount of each species present at the surface, the observation of vinyl group vibrational modes is in qualitative agreement with the XPS findings, indicating that a fraction of molecules binds to the surface through Si−N bond (with formation of an imidol species), thus leaving intact the vinyl group. Moreover, direct support to the imidol hypothesis is provided by comparison between the stretching region (>3000 cm^{-1}) in the *N*-allylurea/Si(111) and *N*-allylurea/Au(111) spectra: The feature observed at 3408 cm^{-1} in curve b occurs at higher frequency and is much broader (fwhm ∼200 cm^{-1}, well beyond the experimental resolution) than that attributed to NH stretching modes (3284 cm^{-1}) in the *N*-allylurea/Au(111) spectrum (curve a). These differences can be accounted for by considering a contribution to the *N*-allylurea/Si(111) spectrum of the OH stretching modes, which typically lies above 3400 cm^{-1}.[39] The presence of OH vibrational features confirms the protonation of a fraction of molecular oxygen atoms, in agreement with O 1s analysis. Moreover, it is important to note that the frequency of the N=C stretching modes in imidol is expected to fall in the same region of C=O and C=C modes, i.e., 1600−1700 cm^{-1}, and is therefore consistent with the broad shoulder observed in the HREEL spectrum at 1630 cm^{-1}.

3.3. UPS. In Figure 5, the UPS spectra of the valence band top of the clean Si(111)-(7 × 7) surface and of *N*-allylurea/Si(111)-(7 × 7) are reported and compared. The valence band spectrum of the clean Si(111)-(7 × 7) surface (curve a) is characterized by two features located at 0.8 and 0.3 eV binding energy, attributed in the literature to rest atom (Re) and adatom (Ad) surface states, respectively. The behavior of these features upon molecular adsorption provides some information on the molecular attachment sites. Typically, quenching of one or both of these states is observed upon molecular adsorption, caused by the redistribution of the dangling-bond electron density.[8,34] In the UPS valence band spectrum of *N*-allylurea/Si(111)-(7 × 7) (curve b) both rest atom and adatom features are completely quenched, indicating that both sites are involved in molecular bonding. As in the (7 × 7) unit cell are present six rest atom−adatom (Re−Ad) dimers and six further adatoms, this finding indicates that molecular adsorption involves both Re−Ad dimers and single adatom sites.

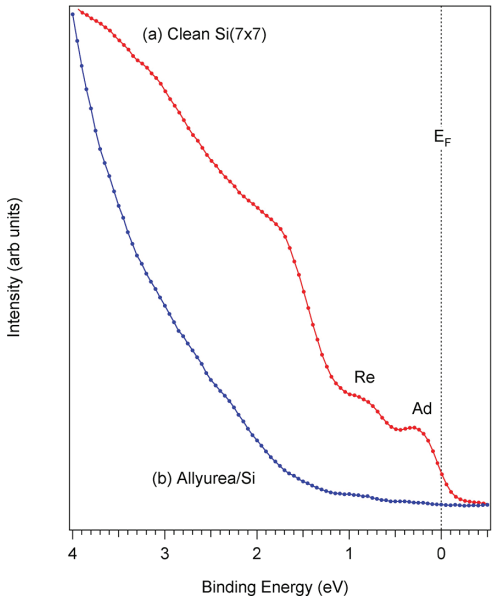

Figure 5. UPS spectra of Si(111)-(7 × 7) clean surface (a) and *N*-allylurea/Si(111)-(7 × 7) (b). The vertical line indicates the position of the Fermi energy.

4. DISCUSSION

Putting together all pieces of information derived from spectroscopic analysis, we are able to propose a comprehensive and quantitative picture of the complex attachment chemistry occurring at the *N*-allylurea/Si(111)-(7 × 7) interface. Indeed, we found strong indication that three different mechanisms of attachment take place at this interface, as sketched in Figure 6: (I) [2 + 2]-like cycloaddition occurring at the rest atom−adatom dimer through cleavage of the vinyl group; (II) Si−N bonding at adatom sites, upon cleavage of NH_2 and rearrangement of the ureic group to form an imidol species (−N=C−OH); this reaction also releases *one* hydrogen atom per molecule; (III) hydrosilylation at adatom sites, through cleavage of the vinyl group and with involvement of the H atoms provided by reaction II.

The relative occurrence F_M (M = I, II, III) of these different mechanisms can be estimated from the results of XPS analysis reported in Table 1. As discussed in section 3.1, roughly one-fourth of the molecules adsorbs through mechanism II, i.e. F_{II} = 1/4, while the remaining fraction of molecules reasonably adsorbs through Si−C bonding, i.e., through both mechanisms I and III, so that $F_I + F_{III} = 3/4$. To quantitatively evaluate the relative occurrence of modes I and III, we now consider how the intensities of the A and B components of the C 1s line shape depend on F_Ms. Contributions to component A come from all carbon atoms directly involved in covalent bonding with the Si surface (i.e., two atoms in mode I, none in mode II, and one in mode III). Therefore, the intensity of component A can be written as $A_A = 2F_I + F_{III}$. Similarly, we can evaluate the contributions to component B by the number of vinyl carbon atoms not interacting with the surface (i.e., none for mode I, two for mode II, and one for mode III), so that $A_B = 2F_{II} + F_{III}$.

Considering now that $F_{II} = 1/4$ and $F_{III} = 3/4 - F_I$, we can estimate the value of F_I and F_{III} from the experimental value of

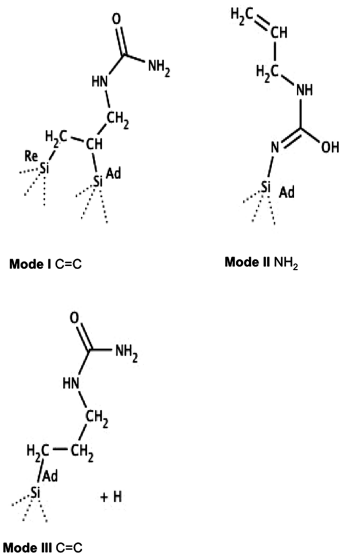

Figure 6. Sketch of the three adsorption modes observed for *N*-allylurea on Si(111)-(7 × 7) (see text for details). Silicon surface atoms are labeled as adatoms (Ad) and rest atom (Re).

the ratio $A_A/A_B = (2F_I + F_{III})/(2F_{II} + F_{III}) = 1.73$ (see Table 1), obtaining $F_I = 0.51$ and $F_{III} = 0.24$. This finding nicely fits with the observation that for hydrosilylation to occur the hydrogen atoms made available by NH_2 cleavage in mechanism II are needed, meaning that F_{III} should be at most equal to F_{II}. The fact that $F_{III} = F_{II}$ suggests that the occurrence of mode III is indeed limited by that of mechanism II.

Keeping in mind that in the (7 × 7) unit cell the most reactive sites are represented by six Re−Ad dimer couples and six adatoms and that cycloaddition typically occurs at rest atom−adatom dimers, we can conclude that half of the molecules adsorbs through [2 + 2]-like cycloaddition at rest atom−adatom dimers, one-fourth adsorbs through Si−N bonding at adatom sites, and the remaining fourth adsorbs through hydrosilylation with Si−C bonding at the remaining adatom sites. In this way, saturation of all dangling bonds at the (7 × 7) surface is obtained, in agreement with UPS data.

5. CONCLUSIONS

Functionalization of silicon with multifunctional molecules possessing different reactive groups is the first important step for further interface modification and growth. Silicon surfaces are extremely reactive, meaning that multiple reaction pathways are possible even for seemingly simple molecules. For this reason, individuation of the reaction pathways leading to the required surface termination is by no means trivial. The Si(111)-(7 × 7) surface, described by the DAS model, is characterized by multiple reaction sites with different reactivity and structural properties. It is therefore expected to display a diversity of reaction mechanisms for different organic molecules and can be considered as a model system to explore more complex situations.

In this work, we studied the UHV adsorption of *N*-allylurea ($CH_2{=}CH{-}CNH{-}CO{-}NH_2$) on the Si(111)-(7 × 7) surface by means of combined HREELS, XPS, and UPS measurements.

This system can be considered as a valuable model to study the adsorption mechanism of multifunctional molecules on Si(111)-(7 × 7) surface. We provide evidence that different adsorption mechanisms take place at this interface: (I) [2 + 2]-like cycloaddition occurring at the rest atom−adatom dimer through cleavage of the vinyl group; (II) Si−N bonding at adatom sites upon cleavage of NH_2 and rearrangement of the ureic group to form an imidol species (−N═C−OH), with the production of a hydrogen atom; (III) hydrosilylation at adatom sites, through cleavage of the vinyl group and involvement of H atoms provided by reaction II.

Competition and mutual influence among different mechanisms are evidenced. Indeed, the [2 + 2] cycloaddition can takes place only at rest atom−adatom dimers and thus cannot completely saturate the surface dangling bonds. On the other hand, the hydrosilylation reaction is not expected to take place at the clean Si(111)-(7 × 7) surface, due to the lack of hydrogen species. We observed that the amine reaction, by making hydrogen atoms available due to the cleavage of the NH bonds, opens the way to the hydrosilylation alternative reaction channel. Interestingly, while on one hand mechanism II is necessary for mechanism III to occur, on the other hand they are both competing for the available surface reactive sites. This mutual influence eventually produces the complete saturation of surface dangling bonds.

■ AUTHOR INFORMATION

Corresponding Author

*E-mail: gaellefrancoise.arnaud@unimore.it.

Notes

The authors declare no competing financial interest.

■ ACKNOWLEDGMENTS

This work was partially supported by MIUR through PRIN 20079KH5H2_002.

■ REFERENCES

(1) Ciampi, S.; Harper, J. B.; Gooding, J. J. *Chem. Soc. Rev.* **2010**, *39*, 2158.
(2) Leftwich, T. R.; Teplyakov, A. V. *Surf. Sci. Rep.* **2008**, *63*, 1071.
(3) Tao, F.; Bernasek, S. L.; Xu, G. Q. *Chem. Rev.* **2009**, *109*, 3991.
(4) Takayanagi, K.; Tanishiro, Y.; Takahashi, M.; Takahashi, S. *J. Vac. Sci. Technol., A* **1985**, *3*, 1502.
(5) Bent, S. F. *Prog. Surf. Sci.* **2003**, *73*, 1.
(6) Buriak, J. M. *Chem. Commun.* **1999**, 1051.
(7) Piancastelli, M. N.; Motta, N.; Sgarlata, A.; Balzarotti, A.; De Crescenzi, M. *Phys. Rev. B* **1993**, *48*, 892.
(8) Rochet, F.; Jolly, F.; Bournel, F.; Dufour, G.; Sirotti, F.; Cantin, J. L. *Phys. Rev B* **1998**, *58*, 11029.
(9) Lu, X.; Wang, X.; Yuan, Q.; Zhang, Q. *J. Am. Chem. Soc.* **2003**, *125*, 7923.
(10) Huang, J. Y.; Tang, H. H.; Shao, Y. X.; Liu, Q. P.; Alshahateet, S. F.; Sun, Y. M.; Xu, G. Q. *J. Phys. Chem. C* **2007**, *111*, 6732.
(11) Tao, F.; Wang, Z. H.; Xu, G. Q. *Surf. Sci.* **2003**, *530*, 203.
(12) Tao, F.; Xu, G. Q. *Acc. Chem. Res.* **2004**, *37*, 882.
(13) Yamada, T.; Shirasaka, K.; Noto, M.; Kato, H. S.; Kawai, M. *J. Phys. Chem. B* **2006**, *110*, 7357.
(14) Terry, J.; Linford, M. R.; Wigren, C.; Cao, R.; Pianetta, P.; Chidsey, C. E. D. *Appl. Phys. Lett.* **1997**, *71*, 1056.
(15) Linford, M. R.; Fenter, P.; Eisenberger, P. M.; Chidsey, C. E. D. *J. Am. Chem. Soc.* **1995**, *117*, 3145.
(16) Huang, J. I.; Ning, Y. S.; Yong, K. S.; Kai, Y. H.; Tang, H. H.; Shao, Y. X.; Alshahteet, S. F.; Sun, Y. M.; Xu, G. Q. *Langmuir* **2007**, *23*, 6218.
(17) Eves, B. J.; Lopinski, G. P. *Langmuir* **2006**, *22*, 3180.

(18) Tang, H. H.; Cai, H. Y.; Ning, Y. S.; Lai, Y. H.; Xu, G. Q. *Surf. Sci.* **2007**, *601*, 3293.
(19) Wang, G. T.; Mui, C.; Musgrave, C. B.; Bent, S. F. *J. Am. Chem. Soc.* **2002**, *124*, 8990.
(20) Higashi, G. S.; Chabal, Y. J.; Trucks, G. W.; Raghavachari, K. *Appl. Phys. Lett.* **1990**, *56*, 656.
(21) He, Y.; Thiry, P. A.; Yu, L. M.; Caudano, R. *Surf. Sci.* **1995**, *331*, 441.
(22) Richardson, N. V. *Curr. Opin. Solid State Mater. Sci.* **1997**, *2*, 517.
(23) Whelan, C. M.; Smyth, M. R.; Barnes, C. J. *Langmuir* **1999**, *15*, 116.
(24) Davis, D. J.; Kyriakou, G.; Lambert, R. M. *J. Phys. Chem. B* **2006**, *110*, 11958.
(25) Löfgren, P.; Krozer, A.; Lausmaa, J.; Kasemo, B. *Surf. Sci.* **1997**, *370*, 277.
(26) Gonella, G.; Terreni, S.; Cvetko, D.; Cossaro, A.; Mattera, L.; Cavalleri, A. O.; Rolandi, R.; Morgante, A.; Floreano, L.; Canepa, M. *J. Phys. Chem. B* **2005**, *109*, 18003.
(27) Haug, A.; Schweizer, S.; Latteyer, F.; Casu, M. B.; Peisert, H.; Ochsenfeld, C.; Chassè, T. *ChemPhysChem* **2008**, *9*, 740.
(28) Seifert, S.; Gavrila, G. N.; Zahn, D. R. T.; Braun, W. *Surf. Sci.* **2007**, *601*, 2291.
(29) Liu, H.; Hamers, R. J. *Surf. Sci.* **1998**, *416*, 354.
(30) Serafin, G.; Friend, C. M. *Surf. Sci.* **1989**, *209*, L163.
(31) Tang, H. H.; Dai, Y. J.; Shao, Y. X.; Ning, Y. S.; Huang, J. Y.; Lai, Y. H.; Peng, B.; Huang, W.; Xu, G. Q. *Surf. Sci.* **2008**, *602*, 2647.
(32) Actually, albeit in principle both amine groups of the molecule could interact with the surface, steric considerations strongly suggest that only the terminal primary amine could be involved in a surface reaction.
(33) Cao, X.; Hamers, R. J. *J. Am. Chem. Soc.* **2001**, *123*, 10988.
(34) Cao, X.; Hamers, R. J. *Surf. Sci.* **2003**, *523*, 241.
(35) Kugler, T.; Thibaut, U.; Abraham, M.; Folkers, G.; Göpel, W. *Surf. Sci.* **1992**, *260*, 64.
(36) Bournel, F.; Carniato, S.; Dufour, G.; Gallet, J. J.; Ilakovac, V.; Rangan, S.; Rochet, F.; Sirotti, F. *Phys. Rev. B* **2006**, *73*, 125345.
(37) Feyer, V.; Plekan, O.; Richter, R.; Coreno, M.; Vall-llosera, G.; Prince, K. C.; Trofimov, A. B.; Zaytseva, I. L.; Moskovskaya, T. E.; Gromov, E. V.; Schirmer, J. *J. Phys. Chem. A* **2009**, *113*, 5736.
(38) http://webbook.nist.gov/chemistry.
(39) Cross, A. D. *An Introduction to Practical Infra-red Spectroscopy*; Butterworths: London, 1964.
(40) Ibach, H.; Mills, D. L. *Electron Energy Loss Spectroscopy and Surface Vibrations*; Academic Press: New York, 1982.
(41) Qiao, M. H.; Tao, F.; Cao, Y.; Xu, G.-Q. *Surf. Sci.* **2003**, *544*, 285.
(42) Yamada, T.; Noto, M.; Shirasaka, K.; Kato, H. S.; Kawai, M. *J. Phys. Chem. B* **2006**, *110*, 6740.
(43) Tao, F.; Yuan, Z. L.; Chen, X. F.; Qiao, M. H.; Wang, Z. H.; Dai, Y. J.; Huang, H. G.; Cao, Y.; Xu, G. Q. *Phys. Rev. B* **2003**, *67*, 245406.

Appendix B

Paper accepted, Journal of Physical Chemistry C.

Nitrocatechol/ZnO Interface: the Role of Dipole in a Dye/Metal-oxide Model System

G. F. Arnaud,[†,‡] V. De Renzi,[*,†,‡] U. del Pennino,[†,‡] R. Biagi,[†,‡] V. Corradini,[‡] A. Calzolari,[‡,¶] A. Ruini,[§,‡] and A. Catellani[‡,‖]

Dipartimento di Scienze Fisiche, Informatiche e Matematiche, Università di Modena e Reggio Emilia, I-41125 Modena, Italy, CNR-NANO, Istituto Nanoscienze, Centro S3, I-41125 Modena, Italy, Department of Physics, University of North Texas, Denton, TX 76203, USA, Dipartimento di Scienze Fisiche, Informatiche e Matematiche, Universitá di Modena e Reggio Emilia, I-41125 Modena, Italy, and CNR-IMEM, Parco Area delle Scienze, 37A, I-43100 Parma, Italy

E-mail: valentina.derenzi@unimore.it;ph++39059-2055274

Abstract

The electronic properties of a prototype system suitable for dye-sensitized solar cell applications are investigated both experimentally and theoretically by means of electron spectroscopies (High-Resolution Electron Energy Loss Spectroscopy , HREELS, Ultraviolet and X-ray Photoemission Spectroscopies, UPS and XPS) and first-principles Density Functional Theory (DFT) -based calculations. The comparison of HREELS and UPS data with the DFT results allows the microscopic description of electronic structure modifications upon interface

[*]To whom correspondence should be addressed

[†]Dipartimento di Scienze Fisiche, Informatiche e Matematiche, Università di Modena e Reggio Emilia, I-41125 Modena, Italy

[‡]CNR-NANO, Istituto Nanoscienze, Centro S3, I-41125 Modena, Italy

[¶]Department of Physics, University of North Texas, Denton, TX 76203, USA

[§]Dipartimento di Scienze Fisiche, Informatiche e Matematiche, Universitá di Modena e Reggio Emilia, I-41125 Modena, Italy

[‖]CNR-IMEM, Parco Area delle Scienze, 37A, I-43100 Parma, Italy

formation, and provides a quantitative evaluation of the ionization energy and electron affinity changes induced by functionalization: these variations can be associated to the electric dipole of the functional species, thus to the formation of an interface dipole layer.

Introduction

Dye Sensitized Solar Cells (DSSCs) have become a consolidated alternative to conventional photovoltaic devices based on silicon technology.[1–3] A percolating mixture of molecular dyes and metal-oxide nanoparticles (e.g. TiO_2, ZnO) constitutes the optically active part of DSSCs: solar light is absorbed by the dye (donor) while the excited electrons are injected into the conduction band of the semiconductor (acceptor) and then collected at the external leads. A p-type hole material, typically an ionic electrolyte, donates electrons back to the dye to complete the cycle. This conceptually simple circuit is built up by several interfaces which should be optimized to enhance cell performances, stability and finally costs. Indeed, the actual performances are wasted due to the occurrence of several microscopic processes (e.g. interface formation, exciton recombination, charge scattering, etc.) that cannot be easily controlled.[4] The efficiency of the solar cell is defined as the ratio between the produced and the incident power. In order to produce electric power, DSSCs must furnish both photocurrent and photovoltage. The maximum value of the produced voltage V_{OC} is the difference between the quasi-Fermi level of the semiconductor under illumination (i.e. when injected photoelectrons are occupying the bottom of the conduction band) and the redox potential of the hole transporter.[5,6] Apparently, V_{OC} seems strictly dictated by the choice of the p- and n-transporting materials, independently from the choice of the dye. The strategies to increase V_{OC} typically rely on the modification of the mesoporous morphology and/or on the improvement of the percolating system compactness, which favors the accumulation of electrons at the interface with the contacts, resulting in a more negative Fermi level of the p-material and thus a larger V_{OC}.[4,7,8] The formation of an interface dipole layer, induced by molecular adsorption, may also shift the position of the semiconductor conduction band and thus the resulting V_{OC}.

This effect has been indeed investigated in particular in the case of solid state heterojunction solar cells.[9–12] In the specific case of DSSCs, few reports have shown a modification of V_{OC}, attributed to the intrinsic dipole moment of the molecular sensitizer[13,14] or of co-adsorbed small molecules.[15] Nonetheless, the exact role of the molecular layer on the variation of the semiconductor electron affinity is not fully addressed. The behavior of the electron affinity upon molecular adsorption on semiconducting substrates is not largely documented, despite molecule-induced variation of the ionization energy was extensively observed on semiconductor functionalized surfaces.[9,16–19] In the case of the ionization energy, the energy modification of the substrate valence band is usually associated to charge transfer between the substrate and the molecule, whose charge reorganization at the interface can be described in terms of surface dipoles, and/or to the presence of molecular dipoles. On the contrary, it is not obvious how molecular adsorption may affect the conduction band (i.e. empty states) of the substrate. In order to decouple these concurring interactions that take place in DSSCs and focus on the effects of dye adsorption on the electronic properties of the substrate, we intentionally disregarded both the fine details of the semiconductor nanoparticle shape and the environment, and we considered a prototypical dye/surface system. By means of electron-spectroscopies (X-ray Photoemission Spectroscopy, XPS, Ultraviolet Photoemission Spectroscopy, UPS, and High-Resolution Energy Loss Spectroscopy, HREELS) and first principles calculations, we studied the effect of the adsorption of a catecholate derivative (1,2-Dihydroxy-4-nitrobenzene, hereafter nitrocatechol) on the electronic properties of an extended ZnO surface. Combining UPS and HREELS measurements allows us to access also the energy position of empty states. Measurements were performed under ultra-high vacuum (UHV) conditions, i.e. in the absence of the electrolyte. While these simplifications do not take into account some characteristic features of the nanostructures (such as edges) and the role of the liquid environment, they provide a more general identification of the dominant electronic effects related to molecular adsorption, not restricted to the unique details of a specific nanosystem. Zinc oxide and nitrocatechol are selected as simple but representative constituents for solar cell applications.[20–22] Most previous works on molecular-induced variation of semiconductor electronic structure considered only TiO_2, which is a non-polar

substrate.[9,11–14,23,24] However, the uniaxial crystal structure of ZnO imparts an internal polarization field to the sample, whose coupling with the dye dipole is not obvious a priori. Furthermore, cathecol-derivatives represent a simple and very popular molecular dye class,[25] whose activity as sensitizer[26–33,35–37] and anchor ligand[38,39] has been largely demonstrated. Finally, nitrocatechol is characterized by a large molecular dipole moment, which makes it a promising candidate to probe the effects of molecular adsorption on V_{OC}. In this work, we provide a thorough characterization of the structural and electronic properties of the functionalized surface and demonstrate the effect of molecular dipole on the energy position of the conduction band of ZnO. We first investigate the microscopic origin of this effect, then we generalize it by using the simple parallel-plate capacitor model.[40] Our results show that a proper tailoring of the dipolar layer at the interface may profitably control the open-circuit voltage of DSSCs.

Methods

Experiments

All measurements were performed in a UHV chamber with a base pressure of 5x10^{-10} mbar. The ZnO $(10\bar{1}0)$ crystal was cleaned by Ar^+ sputtering (1 keV, 10 μA), and annealing (800 ^{o}C) cycles. The deposition of nitrocatechol on the clean ZnO surface was performed in UHV through a molecular beam evaporator[41] and investigated by means of XPS and UPS as a function of coverage. The electronic properties of the system were studied by means of XPS, UPS and HREELS. Band bending was evaluated from the rigid shift of the Zn 3d core level, while work function change was evaluated by the shift of both XPS and UPS secondary edges. UPS and XPS measurements were performed using a He-I discharge-lamp ($h\nu = 21.22$ eV) and an unmonochromatized Al_{K_α} X-ray source ($h\nu$ =1486.7 eV), respectively. Electron energy distribution curves were detected by a hemispherical analyzer (Omicron EA125) with an overall energy resolution of 1.1 eV (0.1 eV for UPS). HREELS measurements were performed in specular conditions ($\theta_i = \theta_o = 70$) with primary energy E_p=20 eV and energy resolution of 20 meV.

Theory

The calculations of adsorption geometries, electronic properties of the functionalized surface, and core level shifts (CLS) were carried out within the Density Functional Theory (DFT) framework, in the planewave pseudopotential implementation, as coded in the Quantum-Espresso package.[42] Since the application of DFT to ZnO is known to produce a severe underestimation of the electronic band gap due to unphysical interaction between the Zn d-orbitals and the O p-bands, we employed the DFT+U scheme to properly compute the electronic structure.[27] The C-1s core level shifts are calculated in the pseudopotential formalism by using the final state theory,[43,44] the specific pseudopotential reproduces the core-excited electron configuration C*(1s1 2s2 2p2). Calculations were performed in supercells with 3×2 ZnO($10\bar{1}0$) lateral periodicity and six ZnO bilayers, with one nitrocatechol molecule symmetrically adsorbed on each surface. Slab replicas were separated by 12 Å of vacuum, and each structure was fully relaxed, until forces on all atoms become lower than 0.03 eV/Å. The structure optimization of the ZnO($10\bar{1}0$) surface reveals the formation of ordered rows of buckled Zn-O dimers along the polar [0001] direction.[45] The initial configuration of the hybrid system was prepared by setting the molecule at $\sim$ 3.2 Å from the surface, with the phenyl ring perpendicular to the surface dimers. During relaxation, the molecule chemisorption occurs spontaneously by creation of two Zn-O bonds with the Zn atoms belonging to two consecutive Zn-O dimers, and formation of two hydrogen bonds between the molecule and the substrate.[27] The surface does not exhibit structural distortion, except for the buckling removal occurring for the dimers involved in the chemisorption. The final adsorption geometry is sketched in Fig.1.

Results

4-Nitrocatechol adsorption

The molecular adsorption process has been experimentally monitored and characterized by XPS core level measurements. In Fig.2 and Fig.3 the O 1s, N 1s and C 1s core level peaks are reported.

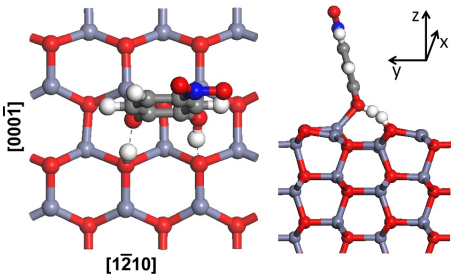

Figure 1: Top (right panel) and side (left panel) view of the nitrocatechol molecule chemisorbed on the ZnO(10$\bar{1}$0) substrate. The molecule is anchored to the surface through two Zn-O chemical and two hydrogen bonds.

Analysis of these peaks has been performed by fitting their lineshapes with Voigt multiplets with fixed Lorentzian width. The O1s lineshape of the clean surface displays two components at 531 eV and 532.3 eV binding energy, which correspond to bulk oxygen and to oxygen atoms of adsorbed hydroxylic groups, respectively. The latter attribution is also confirmed by HREELS measurements (not shown), which show a feature at 456 meV energy loss (3675 cm^{-1}), typical of the stretching mode of partially dissociated water adsorbed on the surface[46] . The O1s spectrum of nitrocatechol/ZnO(10$\bar{1}$0) appears more skewed on the high energy side and can be fitted by two components: The main peak, corresponding to substrate oxygen, lies at 530.6 eV, while the second component at 531.9 eV is attributed to the NO_2 and OH terminations of the nitrocatechol molecule. The N1s core-level shows a single component at 405.2 eV binding energy, attributed to NO_2 species. The relative intensity of N1s, C1s and the molecular component of O1s core levels are in agreements with molecular stoichiometry, revealing that molecules adsorb intact on the surface. The intensity of the N1s and C1s core level saturates upon increasing molecular dose. A rough estimate of the molecular coverage at saturation, based on quantitative XPS analysis, gives a molecular density of 0.18 molecules per ZnO unit cell. We can therefore conclude that saturation corresponds to the formation of a single monolayer with no further adlayer growth. The adlayer density corresponds roughly to one nitrocatechol molecule every six ZnO unit cells. The same molecular density is assumed in the theoretical model. The C1s core-level spectrum is shown in Fig.3. The broadness of the main peak clearly indicates the presence of different components,

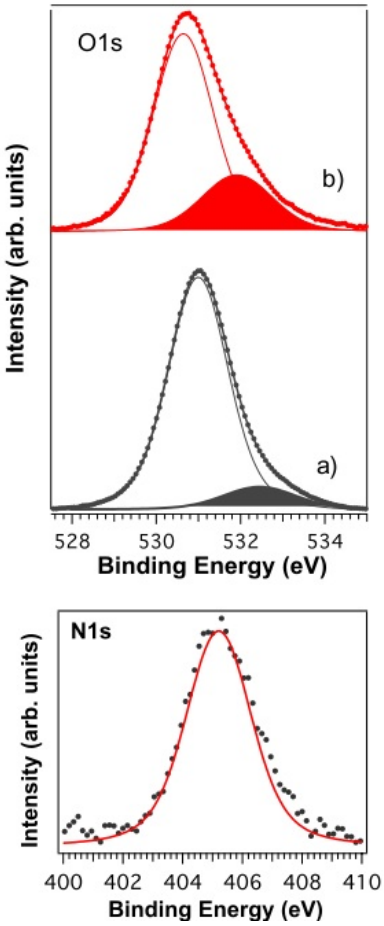

Figure 2: Top panel: O1s core level peak for the clean ZnO(10$\bar{1}$0) (a) and the saturation coverage nitrocatechol/ZnO(10$\bar{1}$0) (b) surfaces. The clean surface spectrum is fitted with two Voigt components, located at 531 eV and 532.3 eV respectively, and associated to bulk oxygen and adsorbed -OH groups. In the nitrocatechol/ZnO(10$\bar{1}$0) spectrum the molecular component appears at 531.9 eV. Bottom panel: N 1s core level peak of the saturation coverage nitrocatechol/ZnO(10$\bar{1}$0) surface: a single component is observed at 405.2 eV.

related to molecular carbon atoms in different chemical states. The theoretical predictions of the C1s core-level shift for the adsorbed molecule allowed us to draw a quantitative analysis of the C1s lineshape. In Fig.3, the theoretical results are reported as vertical lines superimposed to the experimental spectrum: the three aromatic carbons are almost degenerate in energy, and therefore

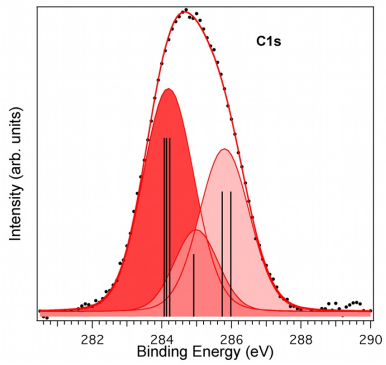

Figure 3: C1s core level peak of the saturation coverage nitrocatechol/ZnO($10\bar{1}0$) surface. The three Voigt components (shaded curves) are located at 284.2 eV, 285 eV and 285.8 eV and attributed to aromatic carbons, C-NO_2 and C-OH, respectively. The calculated values of C1s core level shifts are indicated as vertical lines. Comparison to experimental data is done by aligning the energy of the aromatic carbon components.

build up a single component at low binding energy; the core level C-NO_2 contribution is shifted by +0.83 eV to higher binding energy, while those of the two C-OH atoms are shifted by +1.75 eV with respect to the aromatic carbon core levels. On the basis of these theoretical results, we fit the experimental lineshape with three components. The main component is located at 284.2 eV, while the other two are at 285 eV and 285.8 eV, respectively, corresponding to core level shifts of 0.8 and 1.6 eV. The areas of the three components also follow the theoretical prediction, being in a 3:1:2.2 ratio. The excellent agreement between experiment and theory confirms that the molecules adsorb without disruption. As a result of DFT structural optimization, we find that catechol is chemisorbed through two Zn-O bonds involving two consecutive surface dimers. The adsorbed molecule is slightly distorted with respect to its gas phase geometry: a rotation of the hydroxyl catechol terminations occurs, leading to the formation of two parallel hydrogen bonds with the surface. These findings are in substantial agreement with the results reported in literature for cathecol on anatase and rutile surfaces, for which bonding through the OH group in both monodentate and bidentate configurations have been found.[33]

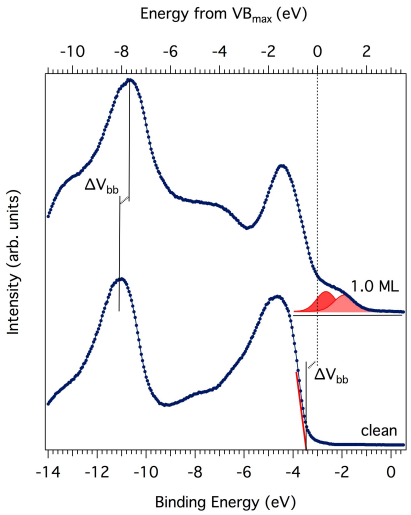

Figure 4: UPS valence band spectra of the clean ZnO(10$\bar{1}$0) (a) and of the saturation coverage nitrocatechol/ZnO(10$\bar{1}$0) (b) surfaces. For the clean surface, the red straight line extrapolates the valence band leading edge at -3.4 eV. For the nitrocatechol/ZnO(10$\bar{1}$0) surface, the spectrum results rigidly shifted by $\Delta V_{bb} = 0.4$ eV, setting VB_{max} at -3.0 eV. The gap feature in the nitrocatechol/ZnO(10$\bar{1}$0) spectrum is fitted with two Gaussian components, located at -1.9 and -2.6 eV binding energy, i.e 1.1 eV and 0.4 eV above VB_{max}, respectively.

Interface electronic properties

The experimental valence band spectra of the clean ZnO surface and of the functionalized interface are reported in Fig.4. Both spectra are dominated by the Zn 3d peak, located around -11 eV binding energy, and by a feature located at roughly - 4 eV, mainly derived from oxygen states. For the clean surface, extrapolation of the low-energy leading edge of the spectrum to zero intensity sets the energy position of the valence band maximum (VB_{max}) 3.4$\pm$0.1 eV below the Fermi energy, indicating that the Fermi level is degenerate with the conduction band minimum (CB_{min}). This means that, as in the bulk the Fermi level lies 0.3 eV below CB_{min} [1], on the clean surface the bands are slightly downward bended ($V_{bb} = 0.3$ eV), in agreement with previous reports.[47] Upon nitrocatechol adsorption, we observe a rigid shift of the whole spectrum towards lower

[1]This determination is based on a separate Hall effect measurement, performed on the same sample before functionalization, which gives an intrinsic n-doping of $\simeq 2.5 \times 10^{14}$ cm^{-3}.

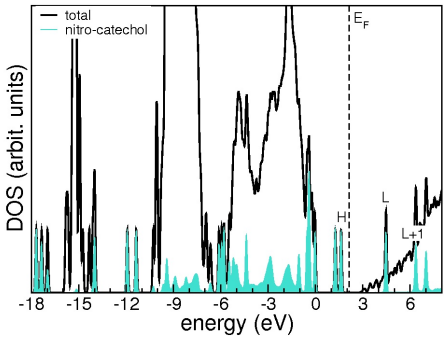

Figure 5: Total density of states (black line) and its projected contribution on nitrocatechol (cyan line) for the molecule/ZnO interface system. The zero of the energy scale corresponds to the valence band top of the ZnO substrate. The peaks corresponding to the molecular frontier orbitals are also indicated.

binding energies, corresponding to an upward shift of the bands. The amount of band bending variation is evaluated tracking the energy position of the Zn 3d peak, and corresponds to $\Delta V_{bb} = -0.4 \pm 0.1$ eV at saturation coverage. We also checked, varying the photon source intensity, that the surface photovoltage effect is negligible in these measurements. Adsorption of the chromophore determines therefore an overall upward band bending $V_{bb} = -0.1$ eV, leading to the formation of a small depletion layer at the ZnO surface. Furthermore, a distinct feature appears in the energy gap region of the UPS spectra. We analyze this feature on the basis of the theoretical results. The calculated DOS of the functionalized surface (Fig.5) shows two molecule-derived states lying in the pristine gap of ZnO, at $\simeq 1.3$ eV and 1.6 eV above VB_{max}; their corresponding wavefunctions indicates that they are associated to almost unperturbed HOMO and HOMO-1 molecular orbitals mainly localized in the molecular ring. The states associated with bond formation to the substrate are instead deeper in energy, and are mostly degenerate with the ZnO valence band. Following the theoretical predictions, we attribute the experimentally observed gap-feature to the superposition of the HOMO and HOMO-1 molecular states. As shown in Fig.4, we fit the spectral shoulder with two Gaussian components located at 1.1 eV (HOMO) and 0.4 eV (HOMO-1) above the ZnO valence band top (see top-axis in Fig.4), in agreement with theoretical predictions. The slight energy discrepancy between the experimental and theoretical states can be traced back to small

differences in the adsorption geometry details between the ideal and the real surfaces. Indeed, the details of adsorption geometry could strongly influence the system electronic properties. For instance, in the case of catechol adsorption on anatase, the energy position of the HOMO state has been found to vary with the molecular adsorption sites (i.e. surface defects vs flat terraces). Furthermore a possible influence of molecular dimer formation on the HOMO position has been also proposed.[34] The residual presence of H_2O molecules and -OH groups in the experimental system may also affect its electronic properties.[45] Nitrocatechol forms a staggered type-II interface with non-polar ZnO surfaces, with unperturbed molecular states in the substrate pristine band gap, as occurs for other molecules of the same class.[27] This is one necessary condition for DSSCs operation. Energy determination of the empty states has been obtained by combining UPS results with HREELS measurements taken in the electronic transition energy loss region (0-7 eV). In Fig. 6 the energy loss spectra of the clean ZnO($10\bar{1}0$) and nitrocatechol/ZnO($10\bar{1}0$) surfaces are reported, suitably matched with the corresponding UPS valence band spectra (see figure caption for details). The HREELS clean surface curve clearly displays an onset at 3.4 eV, which corresponds to the electron excitation across the ZnO band gap. Upon adsorption, the HREEL spectrum is strongly modified: (i) the electron transition onset reduces to 2.3 eV, and (ii) two broad and pronounced features appear at 3.8 eV and 5.8 eV. The red shift of the onset corresponds to a HOMO$\rightarrow$ CB_{min} electronic transition, and reflects the narrowing of the interface band gap due to the presence of the molecular states inside the ZnO gap (type-II interface). The feature appearing at 3.8 eV is attributed to the HOMO $\rightarrow$ LUMO transition, while that at 5.8 eV corresponds to HOMO $\rightarrow$ (LUMO+1) transition. The assignments are in agreement with optical absorption measurements on nitrocatechol in aqueous solution, that reported two main absorption peaks at 3.59 eV and 5.21 eV, attributed to HOMO$\rightarrow$ LUMO and HOMO$\rightarrow$LUMO+1 transitions, respectively.[48] The experimental results set the LUMO and LUMO+1 levels 1.5 eV and 3.5 eV above the CB_{min} , respectively. The simulated DOS reproduces the same spectral features (Fig. 5) dominated by two prominent peaks, corresponding to the unperturbed LUMO ($\simeq$ 1.4 eV above CB_{min}) and LUMO+1 ($\simeq$ 3.4 eV above CB_{min}) molecular states degenerate with the ZnO conduction band.

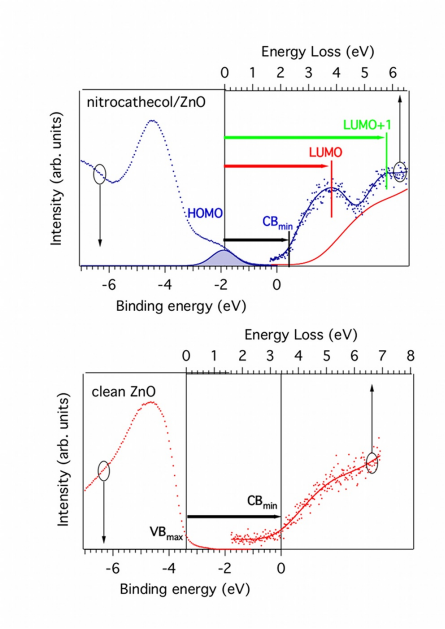

Figure 6: UPS valence band (left axis) and HREELS (right axis) spectra of the clean ZnO(10$\bar{1}$0) (bottom panel) and nitrocatechol/ZnO (10$\bar{1}$0) (top panel) surfaces. Spline curves of HREELS data are also shown as guide for the eye. Bottom panel: The onset of electronic transitions is at 3.4 eV. The zero of the energy loss scale is aligned to the UPS VB_{max}. Top panel: The onset of the electronic transitions is at 2.3 eV and corresponds to the HOMO$\rightarrow$ CB_{min} distance. The HOMO $\rightarrow$ LUMO and HOMO $\rightarrow$ LUMO+1 transitions are at 3.8 eV and 5.8 eV, respectively. The zero of the energy loss scale is aligned to the UPS HOMO (shaded curve). The spline of the HREELS clean surface data are also shown for comparison (red line).

Ionization energy and electron affinity variations

As described in the introduction, the energy positions of the semiconductor bands and of the molecular states relative to the vacuum level are fundamental parameters of the dye/semiconductor interface, which influence DSSCs performances. The modification of the interface ionization energy (IE) can be evaluated from photoemission data, taking into account both work function (ΔW_F) and band bending variations ΔV_{bb} induced by molecular adsorption, according to the following equation: $\Delta IE = \Delta W_F + \Delta V_{bb}$.[49] In Fig. 7 these three quantities are reported as a function of nitrocatechol coverage: the change in band bending saturates at -0.4 eV, while the work function

variation is 1.7 eV (see Supplementary Information). This corresponds to a quite impressive 1.3 eV variation of the ionization energy, which leads to a strong downward shift of the whole valence band relative to the vacuum level. The origin of this shift can be investigated in details by means of DFT calculations, in terms of interface dipole moments and macroscopic average of the Hartree and external potential energies of the functionalized surface. As described in Ref.,[50] the macroscopic average of the electrostatic potential energy, ΔV_{macro}, has been calculated by integrating over the plane parallel to the surface and, then, by a running average along the $(10\bar{1}0)$ direction with a period equal to a bilayer distance. Indeed, the molecular dipole is linked to the ionization energy of the system, that is derived with reference to the vacuum level. This construction is depicted in Fig. 8, where the macroscopic electrostatic potential energy of the clean surface and of the functionalized system are represented, as a function of the z position in the slab: the difference in vacuum levels is a measure of the interface dipole change induced by functionalization.[40] In this frame, we obtain a theoretical prediction for the ionization energy variation of 1.6 eV, which reproduces quite well the experimentally observed value. We observed that small modifications in the adsorption geometry and/or the presence of -OH groups can slightly alter the interface dipole moment, thus the calculated ΔV_{macro}. This can lead to an even better agreement between experimental and theoretical results, in the presence of a more complex scenario such as the real functionalized system.

Discussion

From the results presented above, we may draw the following considerations:

- Nitrocatechol adsorbs on non-polar ZnO surfaces without strong chemical modifications (except protonation): this is accompanied by the presence of almost unperturbed molecular states in the pristine substrate band gap, as revealed from the calculated density of states. Indeed, since the molecular edge states are not involved in bond formation (the bonding states lay deeper in energy, and are degenerate with the substrate valence band) they are not

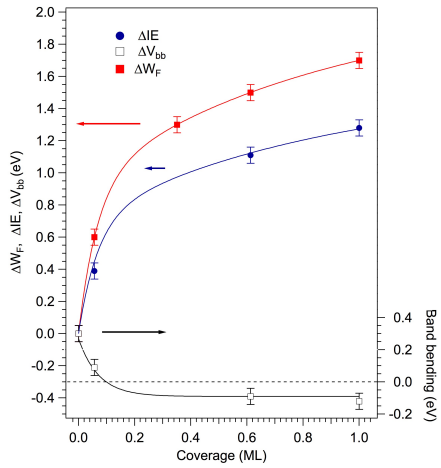

Figure 7: Variation of work function, band bending and ionization energy as a function of nitrocatechol coverage. The right axis shows also the variation of band bending relative to the flat band condition (horizontal dashed line) , as determined by the bulk Fermi level position.

modified by interface formation.

- Surface functionalization preserves the clean ZnO band gap value, i.e. the distance between CB_{min} and VB_{max} is not affected by adsorption. This is an outcome of the combined UPS and HREELS data: summing the values of the HOMO-VB_{max} (1.1 eV) and CB_{min}-HOMO (2.3 eV) distances, we get CB_{min}-VB_{max}= 3.4 eV, i.e. the clean surface value. We therefore conclude that no significant density of states around CB_{min} is induced by molecular adsorption. Calculated DFT gaps for both bare and functionalized ZnO surface confirm this statement. This finding proves that the semiconductor valence and conduction bands experience the same energy shift upon adsorption, i.e. $\Delta IE = \Delta EA$. This is not an obvious result, and it comes from the combination of two effects: (i) the specific molecular orbital distribution after adsorption and (ii) the intrinsic sp-character of ZnO valence and conduction bands[2].

- The variation in the ionization energy induced by the interface dipole layer can be expressed

[2]Such result is not obtained for TiO_2, where the top valence bands have sp character while the bottom conduction band states are d-like.

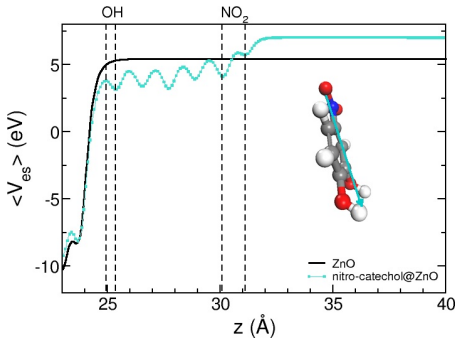

Figure 8: Macroscopic average of the electrostatic potential energy for the clean (black line) and nitrocatechol-functionalized (cyan line) ZnO surface. The inset shows the molecule geometry in the chemisorbed configuration: the corresponding electric dipole is also indicated as an arrow.

within the simple parallel-plate capacitor model,[40] as:

$$\Delta IE = \frac{e\mu_{\perp}\theta}{\varepsilon_0}, \tag{1}$$

where $\mu_{\perp}$ is the component of the molecular dipole moment perpendicular to the surface, θ is the molecular density (here corresponding to the (3x2) structure) and ε_0 the vacuum dielectric constant. The simple capacitor model is able to reproduce almost perfectly the full theoretical result for ΔV_{macro} (1.6 eV) only if the z-component of the molecular dipole in the distorted configuration ($\mu_z = -4.57D$) is considered, z being the direction perpendicular to the substrate. This simple analysis shows that in principle the ionization energy variation can be fully accounted for by just considering the molecular dipole moment in the adsorbed geometry and that adsorption-induced molecular distortion can have considerable influence in the determination of the vacuum level shift. On the other hand the molecular distortion that takes place during the adsorption process is itself an effect of the interaction with the substrate, which directly depends also on the electrostatic properties of the system. (See for instance Ref.[28] for the effects of adsorption of catechol molecules on different hexagonal substrates). Eq. 1 implies a direct relationship between the orientation of the molecular dipole (inwards/outwards the surface) and the upward/downward shift of

the ionization energy. This, along with the observed rigidity of the bandgap, provides also a connection between the orientation of the molecular dipole and the modification of the conduction band, and consequently of the open-circuit voltage of DSSCs. We in particular note that in the significant case of cathecolate molecules, where adsorption occurs through -OH linkers and involve hydrogen-bond formation, molecular distortion can be associated to the degree of protonation of the adsorbed molecule. The understanding that we obtain from our experimental and theoretical observations leads to a scenario where the molecules are adsorbed without dissociation (except protonation) on the ZnO substrate, although experiencing a strong bond stretching. Furthermore, molecular distortion is associated to molecular dipole variation, which determines the ionization energy of the functionalized system. We note here that, as shown in Fig.7, the dependence of the ionization energy on coverage is not linear: it steeply increases at low coverage, while its value tends to saturate for higher coverage. This behavior is quite typical of adsorbates on metal and semiconductor surfaces[51,52] and is usually attributed to a coverage-dependent decrease of the adsorbate dipole moment due to depolarization.[40] A possible role of variations in the adsorption geometry for different coverage can also be envisaged.

- The results obtained for other non-polar metal-oxides (e.g. TiO_2)[9,15] on the linkage between molecular dipoles and V_{OC}, or rather substrate Electron Affinity, can be extended to polar compound semiconductors, such as ZnO. This is a non trivial result, since it has been shown[53–55] that dipole fields are present even at non-polar surfaces in these compounds, which in principles may couple with the dipole of the impinging molecules, modifying for instance its resulting geometry in the adsorption configuration.

Conclusions

In the present work, we provided a comprehensive picture of the electronic properties and energy level alignment of the nitrocatechol/ZnO interface, combining the results of different electronic

spectroscopies with those of DFT calculations. This helped us to elucidate the different roles played by band bending, molecular states and molecular dipole moment. We showed that dye adsorption induces a very strong variation in both the ionization energy and the electron affinity of the interface. i.e. both valence and conduction bands undergo a rigid shift upon molecular adsorption. These variations are relevant as they could determine, in a complete DSSC cell, a significant change in V_{OC}. The theoretical model clearly demonstrates that they can be traced back to the formation of an interface dipole layer, mainly related to the intrinsic dipole moment of the molecule. We emphasize that inferring the modification of the level alignment from the simple knowledge of the pristine intrinsic molecular dipole is by no means trivial, while a full microscopic characterization of the interface is needed to reliably determine the vacuum level setting.

Supporting Information Available

XPS measurement of the work function change as a function of nitrocatechol coverage. This information is available free of charge via the Internet at http://pubs.acs.org.

References

(1) Graetzel, M.; Janssen, R. A. J.; Mitzi, D. B.; Sargent, E. H. Materials interface engineering for solution-processed photovoltaics. *Nature* **2012**, *488*, 304-312.

(2) Mershin, A.; Matsumoto, K.; Kaiser, L.; Yu, D.; Vaughn, M.; Nazeeruddin, Md. K.; Bruce, B. D.; Graetzel, M.; Zhang, S. Self-assembled photosystem-I biophotovoltaics on nanostructured TiO_2 and ZnO. *Sci. Rep.* **2012**, *2*, 234-241.

(3) Calogero, G.; Yum, J.-H.; Sinopoli, A.; Di Marco, G.; Gratzel, M.; Nazeeruddin, M. K. Anthocyanins and betalains as light-harvesting pigments for dye-sensitized solar cells. *Solar Energy* **2012**, *86*, 1563-1575.

(4) O'Regan, B. C.; Durrant, J. R. Kinetic and energetic paradigms for dye-sensitized solar cells: Moving from the ideal to the real. *Acc Chem. Res.* **2009**, *42*, 1799-1808.

(5) Hagfeldt, A.; Boschloo, G.; Sun,L.; Kloo, L.; Pettersson, H. Dye-sensitized solar cells. *Chem. Rev.* **2010**, *110*, 6595-6663.

(6) Peter, L. M. Dye-sensitized nanocrystalline solar cells. *Phys. Chem. Chem. Phys.* **2007**, *9*, 2630-2642.

(7) Liu, J.; Shi, Y.; Yang, Y. Solvation-induced morphology effects on the performance of polymer-based photovoltaic devices. *Adv. Func. Mater* **2001**, *11*, 420-425.

(8) Gadisa, A.; Svensson, M.; Andersson, M. R.; Inganas, O. Correlation between oxidation potential and open-circuit voltage of composite solar cells based on blends of polythiophenes/fullerene derivative. *Appl. Phys. Lett.* **2004**, *84*, 1609-1611.

(9) Krueger, J.; Bach, U.; Graetzel, M. Modification of TiO_2 Heterojunctions with Benzoic Acid Derivatives in Hybrid Molecular Solid-State Devices. *Adv. Mater.* **2000**, *12*, 447-451.

(10) Tada, A.; Geng, Y.; Wei, Q.; Hashimoto, K.; Tajima, K.; Tailoring organic heterojunction interfaces in bilayer polymer photovoltaic devices. *Nat Mat.* **2011**, *10*, 450-455.

(11) Goh, C.; Scully, S. R.; McGehee, M. D. Effects of molecular interface modification in hybrid organic-inorganic photovoltaic cells. *J. Appl. Phys.* **2007**, *101*, 114503-114512.

(12) Cappel, U. B.; Plogmaker, S.; Johansson, E. M. J.; Hagfeldt, A. Energy alignment and surface dipoles of rylene dyes adsorbed to TiO_2 nanoparticles. *Phys. Chem. Chem. Phys.* **2011**, *13*, 14767-14774.

(13) De Angelis, F.; Fantacci, S.; Selloni, A.; Graetzel, M.; Nazeeruddin, M. K. Influence of the sensitizer adsorption mode on the open-circuit potential of dye-sensitized solar cells. *Nano Lett.* **2007**, *7*, 3189-3195.

(14) Chen, P.; Yum, J. H.; De Angelis,F.; Mosconi, E.; Fantacci, S.; Moon, S-Jin.; Baker, R. H.; Ko, J.; Nazeeruddin, Md. K.; Graetzel, M. High Open-Circuit Voltage Solid-State Dye-Sensitized Solar Cells with Organic Dye. *Nano Lett.* **2009**, *9*, 2487-2492.

(15) Ruhle, S.; Greenshtein, M.; Chen, S.-G.; Merson, A.; Pizem, H.; Sukenik, C. S.; Cahen, D.; Zaban, A. Molecular Adjustment of the Electronic Properties of Nanoporous Electrodes in Dye-Sensitized Solar Cells. *J. Phys. Chem. B* **2005**, *109*, 18907-18913.

(16) Schlesinger, R.; Xu, Y.; Hofmann, O. T.; Winkler, S.; Frisch, J.; Niederhausen, J.; Vollmer, A.; Blumstengel, S.; Henneberger, F.; Rinke, P.; et al., Controlling the work function of ZnO and the energy-level alignment at the interface to organic semiconductors with a molecular electron acceptor. *Phys. Rev B* **2013**, *87*, 155311-155316.

(17) Yang, S.; Prendergast, D.; Neaton, J. B. Tuning Semiconductor Band Edge Energies for Solar Photocatalysis via Surface Ligand Passivation. *Nanolett.* **2012**, *12*, 383-388.

(18) Wood, C.; Li, H.; Winget, P.; Bredas, J-L. Binding Modes of Fluorinated Benzylphosphonic Acids on the Polar ZnO Surface and Impact on Work Function. *J. Phys. Chem C*, **2012**, *116*, 19125-19133.

(19) Cucinotta, C. S.; Ruini, A.; Catellani, A.; Caldas, M. J. Tailoring the electronic properties of silicon with cysteine: A first-principles study. *Phys. Rev. B* **2005**, *72*, 245310-245316.

(20) H. Morkoc and U. Ozgur, *Zinc Oxide: Fundamentals, Materials and Device Technology*, Wiley-VCH Verlag GmbH and Co. KGaA, Weinheim, **2009**.

(21) Marczak, R.; Werner, F.; Gnichwitz, J.-F.; Hirsch, A.; Guldi, D. M.; Peukert, W.; Communication via Electron and Energy Transfer between Zinc Oxide Nanoparticles and Organic Adsorbates *J. Phys. Chem. C* **2009** , *113*, 4669-4678.

(22) Gnichwitz, J.-F.; Marczak, R.; Werner, F.; Lang, N.; Jux, N.; Guidi, D. M.; Peukert, W.; Hirsch, A.; Efficient Synthetic Access to Cationic Dendrons and Their Application for ZnO

Nanoparticles Surface Functionalization: New Building Blocks for Dye-Sensitized Solar Cells *J. Am. Chem. Soc.* **2010**, *132* , 17910-17920.

(23) Lyon, J. E.; Rayan, M. K.; Beerbom, M. M.; Schlaf, R. Electronic structure of the indium tin oxide/nanocrystalline anatase (TiO_2)/ruthenium-dye interfaces in dye-sensitized solar cells *J. Appl. Phys.* **2008**, *104*, 073714-073723

(24) Cao, L.; Wang, Y.; Zhong, J.; Han, Y.; Zhang, W.; Yu, X.; Faqiang Xu, F.; Qi, D.-C.; Wee, A. T. S. Electronic Structure, Chemical Interactions and Molecular Orientations of 3,4,9,10-Perylene-tetracarboxylic-dianhydride on TiO_2(110). *J. Phys. Chem. C*, *2011*, *115*, 24880-24887.

(25) Sedó, J.; Saiz-Poseu, J.' Busqué, F.; and Ruiz-Molina, D.; Catechol-Based Biomimetic Functional Materials *Adv Mater.* **2013**, *25*, 653-701.

(26) Moser, J.; Punchihewa, S.; Infelta, P. P.; Gratzel, M. Surface complexation of colloidal semiconductors strongly enhances interfacial electron-transfer rates. *Langmuir* **1991**, *7*, 3012-3018.

(27) Calzolari, A.; Ruini, A.; Catellani,A. Anchor Group versus Conjugation: Toward the Gap-State Engineering of Functionalized ZnO($10\bar{1}0$) Surface for Optoelectronic Applications. *J. Am. Chem. Soc.* **2011**, *133*, 5893-5899.

(28) Calzolari, A.; Ruini, A.; Catellani, A. Surface Effects on Catechol/Semiconductor Interfaces. *J. Phys. Chem. C* **2012**, *116*, 17158-17163.

(29) Rego, L. G.; Batista, V. S. Quantum dynamics simulations of interfacial electron transfer in sensitized TiO_2 semiconductors. *J. Am. Chem. Soc.* **2003**, *125*, 7989-7997.

(30) Duncan, W.; Prezhdo, O. V. Electronic structure and spectra of catechol and alizarin in the gas phase and attached to titanium. *J. Phys.Chem B* **2005**, *109*, 365-373.

(31) Rangan, S.; Theisen, J.-P.; Bersch, E.; Bartynski, R. A. Energy level alignment of catechol molecular orbitals on ZnO $(11\bar{2}0)$ and TiO_2 (110) surfaces *App. Surf. Sci.* **2010**, *256*, 4829-4833.

(32) Li, S.-C.; Chu, L.-N.; Gong, X.-Q.; Diebold, U. Hydrogen bonding controls the dynamics of catechol adsorbed on a TiO2 (110) surface. *Science* **2010**, *328*, 882-884.

(33) Li, S.-C.; Wang, J.-G.; Jacobson, P.; Gong, X.-Q.; Selloni, A.; Diebold, U. Correlation between Bonding Geometry and Band Gap States at Organic-Inorganic Interfaces: Catechol on Rutile TiO_2(110). *J. Am. Chem. Soc.* **2009**, *131*, 980-984.

(34) Li, S.-C.; Losovyj, Y.; Diebold, U. Adsorption-Site-Dependent Electronic Structure of Catechol on the Anatase TiO_2 (101) Surface. *Langmuir* **2011** *27*, 8600-8604.

(35) Syres, K. L.; Thomas, A. G.; Flavell, W. R.; Spencer, B. F.; Bondino, F.; Malvestuto, M.; Preobrajenski, A.; Gratzel, M. Adsorbate-Induced Modification of Surface Electronic Structure: Pyrocatechol Adsorption on the Anatase TiO_2 (101) and Rutile TiO2 (110) Surfaces. *J. Phys. Chem. C* **2012**, *116*, 23515-23525.

(36) Rangan, S.; Katalinic, S.; Thorpe, R.; Bartynski, R. A.; Rochford, J.; Galoppini, E. Energy Level Alignment of a Zinc (II) Tetraphenylporphyrin Dye Adsorbed onto TiO_2 (110) and ZnO$(11\bar{2}0)$ Surfaces. *J. Phys. Chem. C* **2010**, *114*, 1139-1147.

(37) Jankovic, I. A.; Saponjic, Z. V.; Comor, M. I.; Nedeljkovic, J.M. Surface Modification of Colloidal TiO_2 Nanoparticles with Bidentate Benzene Derivatives. *J. Phys. Chem. C* **2009**, *113*, 12645-12652.

(38) Rice, C. R.; D. Ward, M. D.; Nazeeruddin, M. K.; Graetzel, M. Catechol as an efficient anchoring group for attachment of ruthenium âĂŞpolypyridine photosensitisers to solar cells based on nanocrystalline TiO_2 films. *New J. Chem.*, **2000**, *24*, 651-652.

(39) Ye, Q.; Zhou, F.; Liu, W. Bioinspired catecholic chemistry for surface modification. *Chem. Soc. Rev.*, **2000**, *40*, 4244-4258.

(40) Lueth, H. *Surface and Interfaces of Solid Materials*, Springer Verlag Berlin, **1995**.

(41) De Renzi, V.; Arnaud, G.F.; del Pennino, U. Competing Pathways in N-Allylurea Adsorption on Si (111) (7×7).*J. Phys. Chem. C* **2012**, *116*, 5673-5680.

(42) Giannozzi, P.; Baroni, S.; Bonini, N.; Calandra, M.; Car, R.; Cavazzoni, C.; Ceresoli, D.; Chiarotti, G. L.; Cococcioni, M.; Dabo, I.; et al. QUANTUM ESPRESSO: a modular and open-source software project for quantum simulations of materials. *J. Phys.: Condens. Matter* **2009**, *21*, 395502-395521. See also www.quantum-espresso.org.

(43) Pasquarello, A.; Hybertsen, M. S.; Car, R. Theory of Si 2p core-level shifts at the Si(001)-SiO_2 interface *Phys. Rev. B* **1996**, *53*, 10942-10950.

(44) Catellani, A.; Galli, G.; Gygi, F. First-principles calculations of SiC (001) surface core level shifts. *Appl. Phys. Lett.* **1998**, *72*, 1902-1904.

(45) A. Calzolari, A.; Catellani, A. Water Adsorption on Nonpolar ZnO($10\bar{1}0$) Surface: A Microscopic Understanding. *J. Phys. Chem. C* **2009**, *113*, 2896-2902.

(46) Wang, Y.; Muhler, M.; Woell, C. Spectroscopic evidence for the partial dissociation of H2O on ZnO($10\bar{1}0$). *Phys. Chem. Chem. Phys.* **2006**, *8*, 1521-1524.

(47) Ozawa, K.; Mase, K. Comparison of the surface electronic structures of H-adsorbed ZnO surfaces: An angle-resolved photoelectron spectroscopy study. *Phys. Rev. B* **2011**, *83*, 125406-125414.

(48) Cornard, J.-P.; Rasmiwetti , Merlin, J.-C. Molecular structure and spectroscopic properties of 4-nitrocatechol at different pH: UV-visible, Raman, DFT and TD-DFT calculations. *Chem. Phys.*, **2005**, *309*, 239-249.

Acknowledgments

I dedicate this thesis to my husband, Enrico (and Fitz), who helped me to overcame all the difficulties that occurred during this journey.

I thank my parents for being always so proud of me. I thank my family-in-law for being with me.

I thank Valentina for being very patient with me.

Finally, I thank Prof. Umberto del Pennino and the whole group Sesamo 2 for having taught, explained, discussed and heard.